universität wien

MASTERARBEIT / MASTER'S THESIS

Titel der Masterarbeit / Title of the Master's Thesis

Investigation of Interaction Sites Between Vaccinia Virus Immunomodulator A46 and Human MyD88^{TIR}

verfasst von / submitted by

Meryl Haas, BSc

angestrebter akademischer Grad / in partial fulfilment of the requirements for the degree of

Master of Science (MSc)

Wien, 2020 / Vienna 2020

Studienkennzahl lt. Studienblatt / degree programme code as it appears on the student record sheet:	UA 066 834
Studienrichtung lt. Studienblatt / degree programme as it appears on the student record sheet:	Masterstudium Molekulare Biologie UG2002
Betreut von / Supervisor:	ao. Univ.-Prof. Dr. Timothy Skern

Acknowledgments

First of all, I thank Tim Skern. During my studies, his teaching in structural biology and virology has inspired me to conduct research in this field. I am, thus, grateful for the opportunity to join his lab, practice my biochemical skills, and deepen my knowledge. In particular, I want to thank him for his patience and encouragement.

Many thanks to Daniel Azar for training and supervising me during the lab work and helping me whenever I got stuck at an experiment. I enjoyed our fruitful debates when discussing new experimental data and putting information together to see the bigger picture. I also want to thank the other lab members Karin Olek, Amelie Schoenenwald, and Justyna Konecka for the helpful tips and tricks around the daily lab routine and Sina Hanke and Koleta Michalek, whom I had the pleasure to supervise.

All of them, I thank for the warm welcome to the lab, the wonderful times we spent together and for making this research work a memorable time of my life.

From the facilities I thank Nici Drexler for training and helping me during my negative-stain EM image acquisition at the Vienna BioCenter Facility and the team from the Mass Spectrometry Facility at the Max Perutz Labs for performing proteomic analysis of my cross-linked samples using the VBCF instrument pool. For valuable scientific advice I want to thank Gijs Versteeg.

Last but not least, I want to thank my family for supporting me to pursue my dreams, my partner for helping me in hard times, and my friends in Austria and Canada for making my years of studying special.

Abstract

Vaccinia virus belongs to the family *Poxviridae* and was the agent used in a world-wide immunization program to successfully eradicate smallpox, which is caused by the more devastating variola virus, a close relative. Poxviruses are large, complex DNA viruses, their genome encodes about 200 proteins, and their replication occurs exclusively in the host's cytoplasm. Eukaryotes have developed various strategies to detect invading pathogens. Cells of the innate immune system express germ-line encoded pattern recognition receptor (PRR) that sense conserved stimuli, known as pathogen-associated molecular patterns (PAMPs). Upon activation, an intracellular signaling cascade activates transcription factors that lead to the expression of interferons, cytokines, and chemokines. The family of the membrane-bound Toll-like receptors (TLRs) are the best studied receptors. They utilize four canonical adaptors and recruit them via their TIR (Toll/Interleukin-1 receptor)-domain to initiate the signaling cascade. Vaccinia virus has evolved numerous immunomodulators that inhibit TLR signaling at different points in this cascade. In particular, viral A46 binds the TIR-domains of all four canonical TLR adaptors to inhibit signal transduction early on. Investigating the interaction sites between the C-terminal domain (CTD) of A46 and the TIR-domain of the human TLR adaptor myeloid differentiation primary response protein 88 (MyD88) is the main focus of this work.

Based on the structure of the CTD of A46, four surface-exposed amino acids within the last helix $\alpha 7$ were chosen and mutated in two double-mutants to alanines to abolish their interaction properties. The mutants were recombinantly expressed and successfully purified. Using the observations on $MyD88^{TIR}$ assembly formation and the destruction thereof by A46 wild-type, a change in destruction caused by the mutants was observed by negative-stain EM. One mutant showed complete destruction of the assemblies comparable to the wild-type protein while the other mutant allowed

some assembly formation, rendering K206 and/or R209 possible residues involved in the interaction site to MyD88^{TIR}. To confirm the involvement of either of these two residues, protein cross-linking coupled to mass spectrometry (XL-MS) experiments were conducted. Two different cross-linking systems were employed and both confirmed K206 of A46 to be a critical residue at the interaction sites to MyD88^{TIR}. In addition, other cross-linked residues revealed that A46 interacted with MyD88^{TIR} in more than one specific way and possibly targeted more than one molecule at the same time. Furthermore, A46 cross-linked to all assembly interfaces of MyD88^{TIR}. These findings explain on a structural level how viral A46 efficiently inhibits MyD88 assembly and thus, allows vaccinia virus to successfully evade the immune system.

Zusammenfassung

Das Vaccinia Virus gehört der Familie der *Poxviridae* an und wurde in einer weltweiten Impfkampagne zur Ausrottung der Pocken verwendet, welche von dem nahen Verwandten Variola Virus verursacht werden. Die Pockenviren sind große, komplexe DNA Viren, deren Genom kodiert etwa 200 Proteine und sie vermehren sich ausschließlich im Zytoplasma des Wirts. Eukaryoten entwickelten mehrere Strategien um eindringende Krankheitserreger zu entdecken. Zellen des angeborenen Immunsystems exprimieren Rezeptoren, die evolutionär konservierte Reize erkennen, sogenannte pathogen-assoziierte molekulare Muster. Nach der Aktivierung eines Rezeptors, wird eine intrazelluläre Signalkaskade ausgelöst, die die Aktivierung von Transkriptionsfaktoren zur Expression von Interferone, Zytokine und Chemokine veranlasst. Die Familie der Toll-ähnlichen Rezeptoren (engl: TLR) ist das best-erforschte Mitglied und verwendet zur Initiierung der Kaskade vier kanonische Adapter, die alle eine Toll/Interleukin-1 Rezeptor (TIR)-Domäne beinhalten. Das Vaccinia Virus entwickelte zahlreiche Immunmodulatoren, die an verschiedenen Stellen in der TLR-Kaskade die Signalweiterleitung unterbinden. Im Speziellen bindet das virale A46 Protein an die TIR-Domänen aller vier kanonischen Adapter. Die Untersuchung der Bindungsstellen zwischen dem viralem A46 Protein und der humanen $MyD88^{TIR}$ Adapter-Domäne ist die Zielsetzung dieser Forschungsarbeit.

Basierend auf der Struktur der C-terminalen Domäne von A46 wurden vier exponierte Aminosäuren in der letzten Helix $\alpha 7$ ausgewählt und in zwei Doppelmutanten zu Alaninen mutiert. Nach rekombinanter Expression und erfolgreicher Aufreinigung wurde die veränderte Interaktionsfähigkeit getestet. Hierfür nutzte ich die Beobachtung im Elektronenmikroskop mittels Negativfärbung, wodurch geordnete $MyD88^{TIR}$ Polymere sichtbar gemacht werden können sowie deren Zerstörung durch wildtyp A46. Ein Mutant zeigte kein verändertes Bild im Vergleich zum Wildtyp

des A46 Proteins, während der zweite Mutant Formierung von Polymeren in gewissem Maße zuließ. Dadurch ergaben sich zwei potentielle Stellen (K206 und R209) als ersten Anhaltspunkt, welche durch die permanenten Vernetzung naheliegender Aminosäuren mit anschließender Analyse mittels Massenspektrometrie genauer erforscht wurden. Zwei Vernetzungssystem wurden verwendet und beide bestätigten, dass K206 an der Interaktion zu $MyD88^{TIR}$ beteiligt war. Zudem enthüllten weitere verlinkte Aminosäuren, dass A46 in mehr als nur einer Art und Weise mit MyD88 interagierte und womöglich sogar mehrere Adaptermoleküle gleichzeitig binden konnte. Außerdem besetzte A46 alle Berührungsflächen des MyD88 Polymers. Diese Ergebnisse erkären auf einer strukturbasierten Ebene, wie virales A46 effizient die Signalweiterleitung von MyD88 unterbindet und dem Virus dadurch erlaubt dem Immunsystem zu entgehen.

Contents

1

Introduction

Vaccinia virus (VACV) is the agent used to successfully eradicate smallpox in the 20th century and has since become a model system to study virus-host interactions. Cells of the innate immune system express pattern recognition receptors (PRRs) that detect conserved pathogen-associated molecular patterns (PAMPs), which activate the receptor and its intracellular signaling cascades lead to an immediate first response and the stimulation of the long-lasting adaptive immunity. The best-studied members are the Toll-like receptors (TLRs). Viruses have evolved different strategies to evade the host's immune system, one of them is to target these signaling cascades. The research in this work focuses on the interaction sites between the viral immunomodulator A46 and the human TLR-adaptor myeloid differentiation primary response protein 88 (MyD88).

1.1 Vaccinia Virus

Smallpox, caused by variola virus (VARV), was one of the most devastating diseases in history with its earliest record more than 3500 years ago (Henderson 2011). In the late 18th century, Edward Jenner systematically tested the hypothesis that milkmaids that had previously been infected with cowpox were protected from the life-threatening smallpox. By inoculating a young boy with a cowpox sample obtained from the lesions of a milkmaid and then challenging the boy with smallpox, Jenner successfully immunized the boy and had thereby developed the first vaccination (Henderson 2011;

Smith and McFadden 2002). Later, the viral agent of this vaccination was discovered and thus named vaccinia virus (VACV), whose origin was long assumed to be cowpox. However, recent analysis of the horsepox genome and early vaccinia vaccines revealed VACV to be more closely related to horsepox than cowpox (Esparza et al. 2017; Jacobs et al. 2009). In the 19th century, cowpox as well as horsepox were used to immunize against smallpox, which may have led to various virus mixtures allowing genetic recombination events and most likely the origin of the laboratory virus VACV (Esparza et al. 2017). All of the above mentioned poxviruses belong to the family *Poxviridae* of the genus *Orthopoxviridae*. Due to conserved structural proteins within this genus, horsepox, cowpox, and VACV provide cross-immunity to smallpox (Jacobs et al. 2009). In 1980, after a worldwide immunization program where live VACV was employed as a vaccine, the World Health Organization (WHO) declared smallpox the first successfully eradicated disease by vaccination (Henderson 2011; World Health Organization 2016).

1.1.1 Importance for Research

Officially, all laboratories have destroyed their live VARV stocks or have transferred them to one of the two institutions that still reposit reproductive VARV - one in the United States and one in Russia (Mahy 2003). However, the threat of intentional release makes it necessary to classify VARV as a potential bioterrorism weapon. Especially since Dr. Ken Alibek claimed in 1999 that smallpox had been developed in the Bioweapons Program of the USSR from 1980 to 1990 and in light of the terrorist attack on September 11th, 2001, the debate on biological warfare has surfaced (Mahy 2003; Smith and McFadden 2002). Due to the high transmissibility and mortality rate of VARV, especially younger generations would be susceptible to a smallpox outbreak because vaccination efforts have been stopped after it was declared eradicated (Mahy 2003). Therefore, the WHO and selected national institutions have replenished their

stockpile of vaccinia vaccinations (Lane and Poland 2011). However, especially for the 1st generation of vaccines, postvaccinal impairments have been reported, in the worst cases leading to encephalitis and death (Jacobs et al. 2009; Smith and McFadden 2002). A better understanding of VACV is, therefore, essential to develop safer vaccines.

A highly attenuated strain, called modified vaccinia Ankara (MVA), derived in the late 1960s maintained its immunogenicity but was incapable of productively replicating in most mammalian cells due to its lack of large portions of the VACV genome and numerous point-mutations that prevent maturation of the virion (Jacobs et al. 2009; Volz and Sutter 2017). MVA is now licensed as a 3rd generation vaccine against smallpox (Volz and Sutter 2017). More interestingly, MVA allows insertion and high level expression of large foreign genes, which makes it a promising vector for recombinant vaccine development against infectious diseases (Jacobs et al. 2009). Recent research on recombinant MVA vaccines against human immunodeficiency virus (HIV)-1, Mycobacterium tuberculosis, and Plasmodium falciparium (malaria) has advanced to the clinical test phase (Volz and Sutter 2017). In light of the current global pandemic (COVID-19) caused by the severe acute respiratory syndrome coronavirus 2 (SARS-CoV-2) and the urgent need for a vaccination, research on MVA-derived vaccines has begun (Chiuppesi et al. 2020).

Additionally, VACV offers a great opportunity to study virus-host interactions because it expresses a plethora of antagonists to the innate immune system by inhibiting the activity of interferons (IFNs), cytokines, chemokines, and signaling cascades (Smith et al. 2013). The attenuated strain MVA lacks most of these genes and thus, by reinserting a particular VACV gene, its specific function can be studied in cells (Volz and Sutter 2017). Once the target of a particular viral protein is found, further structural studies can be conducted to investigate the interaction mechanisms in detail. By learning from the virus how it specifically inhibits certain parts of the

immune system, we could mimic its strategy and develop novel therapeutic methods. The research conducted for this thesis focused on the structural investigation of one such viral protein, called A46, and how it specifically inhibits one protein involved in the signaling cascade.

1.1.2 Structure of Vaccinia Virus

The complex structure of poxviruses is unique among viruses and does not follow an icosahedral or helical symmetry (Condit et al. 2006). VACV exists in two infectious forms: intracellular mature virions (MVs) are released by lysis of the infected cell, while extracellular enveloped virions (EVs) acquire two membrane layers during intracellular maturation and disseminate by exocytosis resulting in one additional membrane compared to MVs (Moss 2016; Schmidt et al. 2012). The large barrel to brick-shaped MV particle has a size of approximately 360 x 270 x 250 nm (Cyrklaff et al. 2005) and is, thus, visible by light microscopy. The outer layer of the MV particle consists of a complex lipid membrane, which surrounds a biconcave, walled core flanked by two proteinaceous lateral bodies (Condit et al. 2006). The lateral bodies, which are released into the cytoplasm upon infection, are believed to contain viral enzymes essential to inhibit an early immune response in the host cell (Schmidt et al. 2013). The core is walled with two layers: the outer, striated wall called "palisade layer" and the inner "smooth layer". In the core, viral nucleoproteins associate with the supercoiled genome (Condit et al. 2006).

The linear, double-stranded (ds) DNA molecule of poxviruses is between 130 and 230 kb in length and encodes about 200 proteins (Mohamed and McFadden 2009; Moss 2013). The central region of the genome is conserved in sequence across species holding essential genes for transcription, DNA replication, and structural proteins, while variable genes located towards the termini code for non-essential functions and define host range, virulence, and immunomodulators and end in inverted ter-

minal repeats (ITR) (Smith and McFadden 2002). The two ends of the ds DNA molecule are linked together to form a continuous polynucleotide chain ending in non-complementary hairpins (Moss 2013; Smith and McFadden 2002).

The genome of the VACV Copenhagen strain was the first complete sequence to be published and thus, the initial genetic nomenclature was based on it. Genes were denoted with letters and numbers corresponding to their position relative to the left of individual *Hind*III fragments. An additional letter (L or R) referred to the direction of the open reading frame (ORF), which was often omitted in the names of the gene products. However, if this same system was applied to a different strain, orthologous genes would have been numbered differently causing confusion. Therefore, current nomenclature simply numbers the genes from left to right along with the virus strain but gene products are often still referred to with the orthologous names of the Copenhagen strain (Condit et al. 2006). In this regard, the protein of interest in this thesis is called A46 with the gene name VACWR172, WR standing for Western Reserve strain (The UniProt Consortium 2019, ID: P26672).

1.1.3 Life Cycle

The principal steps in the reproductive life cycle of poxviruses starts with the entry, followed by gene expression and DNA replication leading to the assembly and maturation of progeny particles, and ends with dissemination (Figure 1.1). This process can take as little as 4 h under suitable conditions, with a maximum yield of new particles obtained after 24 h (Moss 1990).

Entry

The entry of viral particles is defined as the step in which the core enclosing the genome is released into the cytoplasm (Moss 2016). Enveloped viruses enter via fusion, either at the plasma membrane or after endocytic uptake of the viral particle at the endosomal or lysosomal membrane (Schmidt et al. 2012). MV particles, one form

of infectious virion of VACV, were reported to enter at the plasma membrane at a neutral pH and via the endocytic route by macropinocytosis or fluid-phase endocytosis at an acidic pH (Moss 2016). EVs, the other infectious form, have one additional membrane, which restricts them from direct fusion; instead the EV membrane ruptures in a nonfusogenic reaction upon contact with glycosaminoglycans (GAGs), thereby releasing an MV-like particle that can then fuse with the membrane (Law et al. 2006; Schmidt et al. 2011).

In the MV membrane, five proteins have been identified to bind to cellular surface proteins: D8 binds to chondroitin, A27 and H3 to heparan, A26 to laminin, and L1 to a yet unknown protein. A conserved 11-protein complex spanning the MV membrane, called the entry fusion complex (EFC), mediates post attachment steps essential for fusion. Two of these eleven proteins in the EFC were shown to be targets of neutralizing antibodies (Moss 2016).

Upon successful fusion and release into the host's cytoplasm, the lateral bodies dissociate from the core and the phosphatase VH1 (also refereed to as H1) rapidly inactivates cellular STAT1 to prevent an IFNγ-mediated antiviral response. The once biconcave core undergoes structural changes and becomes oval, while an increase in its size suggests active transcription of early genes within the viral core (Schmidt et al. 2013). In addition, the core is transported on microtubules deeper into the cytoplasm (Carter et al. 2003).

A process called superinfection exclusion prevents reinfection of the same cell where two mechanisms are known for VACV. Early during infection, viral A33 and A36 are expressed on the host's membrane to repulse EVs, while the second mechanism is triggered by late gene products where a complex of two viral proteins, A56 and K2, is expressed on the cell membrane that interacts with the EFC and blocks fusion (Moss 2016).

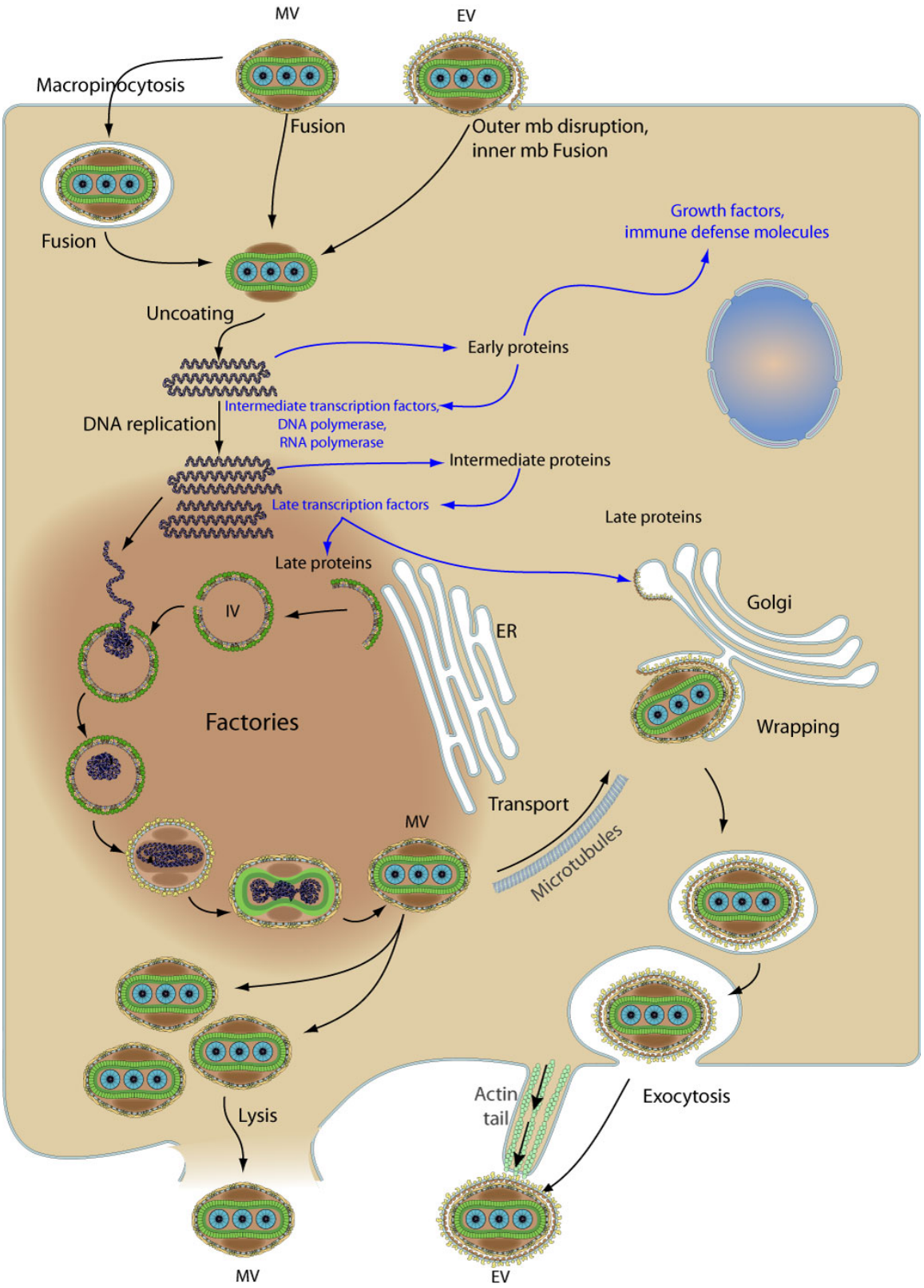

Figure 1.1: **A schematic and simplified overview of the life cycle of *Poxviridae*.** Figure: ViralZone by Swiss Institute of Bioinformatics (2020).

Replication

The poxviral replication is unique among viruses in that it occurs exclusively in the cytoplasm and is studied extensively for VACV. Gene transcription and DNA replication follow a temporal orchestrated cascade: late gene products are packaged into the core along with the genome to initiate early gene transcription, which results in the expression of enzymes and factors required for DNA replication and intermediate gene expression, which in turn switches on late gene transcription (Broyles 2003; Condit et al. 2006; Moss 2013). In addition, VACV expresses the proteins D9 and D10, which degrade viral as well as host mRNAs alike. Thereby, they cause a turnover of viral mRNA resulting in an additional switch from early to intermediate to late gene expression while at the same time they inhibit host gene expression and thus activation of an immune response (Smith et al. 2013).

Early genes are transcribed and processed within the core immediatly after fusion with the host cell (Schmidt et al. 2013). The viral early transcription factor (ETF) recruits viral RNA polymerase with H4 to early gene promoters and hydrolyses ATP to initiate transcription. To produce mature viral mRNAs that resemble cellular mRNAs, a capping enzyme, poly(A) polymerase, and 2'-O-methyltransferase are packaged into the core along with the RNA polymerase. Within minutes after cell entry, viral transcripts are released through pores into the host's cytoplasm and hijack the cellular translation machinery for protein synthesis (Broyles 2003; Stern-Ginossar et al. 2019). Gene products of this phase include proteins required for viral DNA replication and intermediate gene transcription, viral immunomodulators to evade an immune response, and growh factors, like the vaccinia growth factor VGF that is responsible for the characteristic dermal hyperplasia (skin lesions) associated with infections (Albarnaz et al. 2018; Condit et al. 2006; Smith et al. 2013). About half of the genes are believed to be early stage genes, with the immunomodulator A46 being one of them (Broyles 2003; Stack et al. 2005).

Upon release of the DNA from the core, seven enzymes are required for DNA replication, which are synthesized from early gene transcripts: viral DNA polymerase, processivity factor A20, uracial-DNA glycosylase, helicase-primase, protein kinase, single-stranded DNA binding protein, and DNA ligase. DNA replication starts within 2 h after infection in so called "viral factories" (Moss 2013), which are domains in the cytoplasm surrounded by E.R.-derived lipids and progress to places of new virion assembly later in infection (Liu et al. 2014).

De novo synthesized DNA serves as a template for intermediate and late gene transcription, which also requires newly synthesized RNA polymerase from early gene expression. Interestingly, H4 is only required for early gene transcription within the core but not for intermediate or late gene expression. Most of the proteins necessary for the assembly of new virions are produced in these two phases, including structural proteins, assembly factors and enzymes that are packaged into the core to transcribe and process viral mRNA upon cell entry (Condit et al. 2006).

Assembly, Maturation & Release

Within viral factories, crescent-shaped membranes start to assemble, indicative of new virion formation. The developing crescent is filled with about 80 different viral proteins constituting the viroplasm. Shortly before closure of the resulting three-dimensional sphere, genomic DNA is packaged into the nascent particle, termed immature virion (IV). Further maturation, including proteolysis, redox-reactions and reconstruction, leads to the infectious MV encompassing two lateral bodies and a transcriptionally activated core (Liu et al. 2014; Moss 2016). MVs are exclusively found inside the host cell, only liberated upon cell lysis (Moss 2016).

A subset of MVs are transported by microtubules to a site where they are wrapped with a double cellular membrane enriched with viral proteins, either derived from early endosomes or the trans-Golgi network (Smith and Law 2004). The wrapped particles are transported to the periphery of the cell on microtubules, where they

fuse with the plasma membrane and exit by exocytosis (Roberts and Smith 2008). Thereby, EVs, the second form of infectious particles, are released while at the same time viral proteins, in particular A36, are retained in the plasma membrane due to the fusion process. In some cases, depending on the cell type and viral strain, A36 stays associated with the released EV particle and induces intracellular actin-polymerization resulting in actin-tails (Roberts and Smith 2008; Smith and Law 2004). Cell-associated, retained EVs are driven into neighboring cells by these actin-tails while released virions mediate long-range dissemination (Smith et al. 2002).

To note, MVs and EVs exhibit different surface protein compositions; it is, thus, not surprising that they show different antigenic properties, which is important to monitor for safer vaccine development (Pütz et al. 2006). EVs are more resistant to neutralizing antibodies and the complement system than MVs, making them ideal to promote cell-to-cell infection, while MVs particles are readily neutralized by antibodies and destroyed by the complement system. However, due to the MV's physical robustness they are important for human-to-human transmission (Moss 2016; Smith and Law 2004).

1.2 Detecting Invading Pathogens

Cells of the innate immune system act as the first line of defense against invading pathogens. They express germline-encoded pattern recognition receptors (PRRs) that recognize pathogens via conserved stimuli, known as pathogen-associated molecular patterns (PAMPs), and activate the innate immune response to elicit an immediate defense as well as the long-lasting adaptive immunity (Abbas et al. 2010). The family of the membrane-bound Toll-like receptors (TLRs) are the most prominent and best-studied receptors and will be introduced in more detail (Gay et al. 2014; Kawai and Akira 2010; Luo et al. 2019; O'Neill and Bowie 2007).

1.2.1 TLR Signaling

Toll-like receptors (TLRs) are transmembrane proteins, which consist of three distinct domains: (i) an extracellular, horseshoe-shaped N-terminal domain with 19-25 leucine-rich repeats to recognize PAMPs, (ii) a transmembrane domain with a single α-helix, and (iii) an intracellular C-terminal TIR (Toll/Interleukin-1 receptor)-domain for relaying the signal downstream (Narayanan and Park 2015; Ve et al. 2015). Upon ligand binding, the receptors are believed to dimerize or oligomerize and thereby undergo a conformational change that allows their cytosolic TIR-domains to act as a scaffold for a signaling complex to bind (O'Neill and Bowie 2007; Saitoh et al. 2004), lately referred to as the TLR signalosome (Nanson et al. 2020). Through utilizing different adaptors, a signaling cascade results in the activation of transcription factors that orchestrate an immune response tailored to the stimulus (Figure 1.2) (Luo et al. 2019; Pandey et al. 2014). Expression of pro-inflammatory cytokines amplify the immune response and shape the adaptive immunity while chemokines attract leukocytes to the site of infection. In addition, type I IFNs are expressed and secreted, which bind to type I IFN receptors of the same or of adjacent cells to initiate the JAK/STAT (Janus kinase / signal transducer and activator of transcription) signaling cascade that leads to the expression of IFN-stimulated genes to confer an antiviral state (Smith et al. 2013).

In humans, there are 10 known functional TLRs whereas in mice 13 are known but only 12 are functional (TLR10 is a non-functional pseudogene). TLRs 1–9 are conserved in both species and can thus be studied in gene-targeted mouse models (Kawai and Akira 2010). In general, each receptor recognizes distinctive PAMPs. On the cell surface, TLR2 (as a homodimer or heterodimer with either TLR1 or TLR6) binds bacterial diacylated or triacylated lipopeptides as well as viral glycoproteins, TLR4 recognizes gram-negative bacterial lipopolysaccharide (LPS) bound to MD2 (myeloid differentiation factor 2) and viral glycoproteins, and TLR5 is the receptor

for bacterial flagellin. Within endosomal compartments, receptors recognize foreign nucleic acids: TLR3 senses viral dsDNA, TLR7 and TLR8 bind viral single-stranded (ss) DNA, while TLR9 is the receptor for bacterial and viral unmethylated CpG-containing DNA motifs. TLR4 is the only receptor that first signals from the plasma membrane and then, upon endocytosis, activates a second signaling pathway from the endosomal membrane (O'Neill and Bowie 2007; Pandey et al. 2014).

TLR Adaptors

Currently, there are four known canonical adaptors, namely MyD88 (myeloid differentiation primary response protein 88), MAL (MyD88-adaptor like, also known as TIRAP), TRAM (TRIF-related adaptor molecule, also known as TICAM-2), and TRIF (TIR-domain-containing adaptor protein inducing IFNβ, also known as TICAM-1), and three regulatory ones (Luo et al. 2019). SARM1 (sterile α- and armidillo-motifs-containing protein 1) inhibits TRIF signaling from endosomal membranes while BCAP (B-cell adaptor for phosphoinositide 3-kinase) negatively regulates TLR signaling by linking it to PI3K (Phosphoinositide 3-kinase), which phosphorylates phosphoinositides at the inositol ring. These modified lipids play an important role in the immune system including signaling cell survival and proliferation. SCIMP (SLP adapter and CSK-interacting membrane protein) positively regulates TLR signaling predominately in macrophages where it acts as a membrane-bound scaffold for multiple TLRs at the plasma membrane as well as at the endosomal membrane. All adaptors, except SCIMP, contain a TIR-domain and engage in homotypic TIR-TIR interactions, either with the receptor and/or with another adaptor (Luo et al. 2019).

Essentially, signal transduction occurs via two pathways, depending on the recruitment of MyD88 or TRIF, thereby distinguishing them into the MyD88-dependent or the TRIF-dependent pathways, respectively. All receptors except TLR3 utilize MyD88 with TLR2 and TLR4 recruiting MAL as a bridging adaptor first. Indeed,

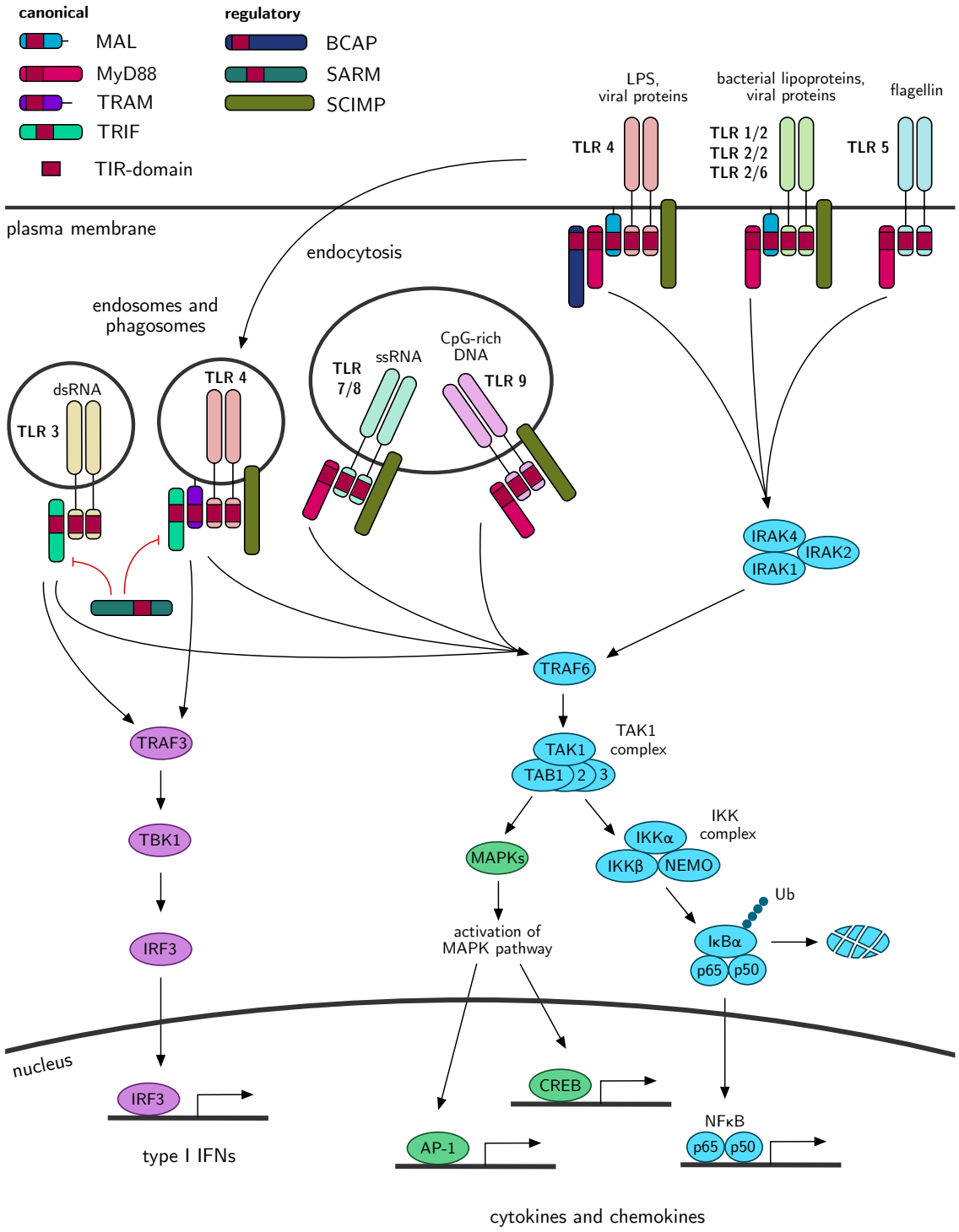

Figure 1.2: **Simplified overview of TLR signaling pathways.** Upon PAMP recognition, the receptors dimerize and trigger an intracellular signaling cascade leading to the expression of pro-inflammatory cytokines and chemokines, and depending on the receptor also type I IFNs production. All abbreviations are listed in the last chapter 7 "Abbreviations", figure generated with Inkscape (2020) based on Balka and Nardo (2018) and Luo et al. (2019).

TLR4 is the most complex receptor as it involves all four canonical adaptors. First, at the plasma membrane TLR4 recruits MAL, which is already in close proximity being tethered to the plasma membrane through its lipid binding motif, and MyD88 to unleash a strong cytokine response by activating the transcription factor NFκB (nuclear factor κB). Then, after endocytosis of TLR4, TRAM as the bridging adaptor being anchored to the endosomal membrane by means of a myristoyl moiety recruits TRIF to initiate type I IFN production and a delayed NFκB response (Balka and Nardo 2018; Bonham et al. 2014; Gay et al. 2014; O'Neill and Bowie 2007).

MyD88-dependent signaling

MyD88 binds via its C-terminal TIR-domain to either the receptor or is activated through MAL, while the N-terminal death domain (DD) recruits the serine/threonine kinase IRAK4 (Interleukin-1 receptor-associated kinase 4) via DD-DD interaction. Upon autophosphorylation, IRAK4 activates IRAK1 and IRAK2 and together with MyD88, they constitute a signaling platform termed the myddosome that induces the activation of the E3 ubiquitin ligase TRAF6 (tumor necrosis factor receptor-associated factor 6). TRAF6 recruits the TAK1 (TGF-β-activated kinase 1) complex, which consists of TAK1 and the three TAK1 binding proteins (TABs) 1-3. Here, the signal is split into two branches, the NFκB activation and the MAPK (mitogen-activated protein kinase) pathway (Arthur and Ley 2013; Balka and Nardo 2018; Chen 2005; O'Neill and Bowie 2007).

NFκB is a dimeric transcription factor retained in the cytosol through binding of IκBα (NFκB inhibitor α) by masking the nuclear translocation signal. TAK1 activates the IκB kinase (IKK) complex, which phosphorylates IκBα, thus targeting it for polyubiquination and subsequent degradation by the proteasome. The IKK complex consists of the two catalytic subunits α and β, and the regulatory subunit NEMO (NFκB essential modulator, also called the subunit γ of IKK). This process releases NFκB with its two subunits p65 and p50 and allows translocation into the

nucleus where it initiates the transcription of pro-inflammatory cytokines (Chen 2005; Ghosh and Dass 2016).

In the MAPK pathway, a cascade of kinases results in the activation and translocation of the transcription factors AP-1 (activator protein-1) and CREB (cAMP response element-binding protein) to induce chemokine and cytokine production (Balka and Nardo 2018).

TRIF-dependent signaling

In the TRIF-dependent pathway, the signal is also transmitted to TRAF6 leading to pro-inflammatory cytokine expression but it also associated with TRAF3 and TBK1 (TANK-binding kinase 1, also known as serine/threonine-protein kinase) to activate the transcription factor IRF3 (interferon regulatory factor 3), which initiates type I IFN expression (Gay et al. 2014).

1.2.2 TIR-domains

TIR-domains comprise 125–200 residues and adopt a flavodoxin-like fold. This topology consists of five β-strands forming a central, parallel β-sheet that is surrounded by five α-helices. The secondary structures alternate in sequence and are labeled from

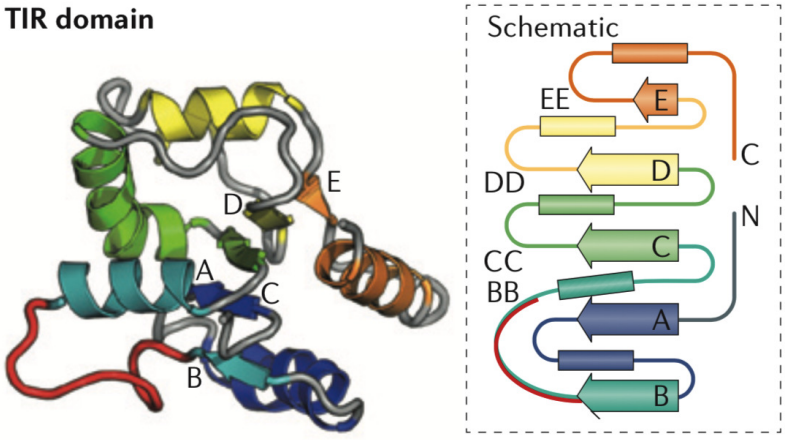

Figure 1.3: **General structure and schematic topology of TIR-domains.** The conserved BB loop motif is marked in red. Figure: Gay et al. (2014).

A to E. Thus, their connecting loops can be identified according to this nomenclature (Figure 1.3). In this respect, the BB loop connects the βB-strand to the αB-helix (Narayanan and Park 2015; Ve et al. 2015).

In general, TIR-domains share limited sequence identity, only the so-called boxes 1–3 are conserved. Structural comparison shows a conserved β-sheet core while the loops and helical regions differ significantly, only the BB loop is conserved (corresponding to box 2). This surface-exposed loop with its conserved proline was shown to be critical for homotypic TIR-domain interactions (Gay et al. 2014; Narayanan and Park 2015; Ve et al. 2015).

TIR-domain assemblies

Recent evidence emphasizes that a higher-order assembly is necessary in the TLR signalosome to amplify and relay the signal downstream, a process coined signaling by co-operative assembly formation (SCAF) (Nimma et al. 2017). Supporting this phenomenon, Ve et al. (2017) reported TIR-domain assembly formation in MyD88-dependent TLR4 signaling. At high concentrations MAL^{TIR} reversibly assembles into filaments *in vitro* and its 12-fold, symmetrical structure was resolved by cryo-EM (PDB ID: 5uzb). In short, each of the 12 protofilaments consists of two MAL^{TIR} strands, which interact via their BB and EE surfaces at the intra-strand and their BC and CD surfaces at the inter-strand interface. When combining MAL^{TIR} and $TLR4^{TIR}$ *in vitro*, filaments of a different phenotype form at lower concentrations than required for the previously mentioned MAL^{TIR} assemblies. Last, $MyD88^{TIR}$ does not assemble on its own or in combination with $TLR4^{TIR}$ *in vitro* but only when combined with low concentrations of MAL^{TIR}. The electrostatic surface potentials of $MyD88^{TIR}$, MAL^{TIR}, and $TLR4^{TIR}$ are distinct in that MAL^{TIR} is largely positively charged whereas the other two predominantly negative. This might explain why MAL is required for TLR4 signaling to bridge to MyD88 (Dunne et al. 2003).

Negative-stain EM micrographs of MyD88 revealed rod-shaped, heterogeneous

MyD88^{TIR}-assemblies varying in size (Ve et al. 2017). Based on a non-symmetrized projection map from cryo-EM micrographs and the known interaction sites from the MAL^{TIR} filament, a model for MyD88^{TIR} assemblies with the respective amino acids participating at the interfaces was proposed (Figure 1.4b and 1.5). Recently, the MyD88^{TIR} assembly structure was resolved by micro-ED, at large confirming the proposed model and its interaction site (by personal communication with Bostjan Kobe).

1.2.3 MyD88

One of the investigated proteins in this thesis is the TIR-domain containing adaptor MyD88 and thus a detail introduction on the current pathophysiological, biochemical and structural information is given.

Human MyD88 consists of 296 amino acids, which structurally fold into two domains (The UniProt Consortium 2019, ID: Q99836). The N-terminal death domain

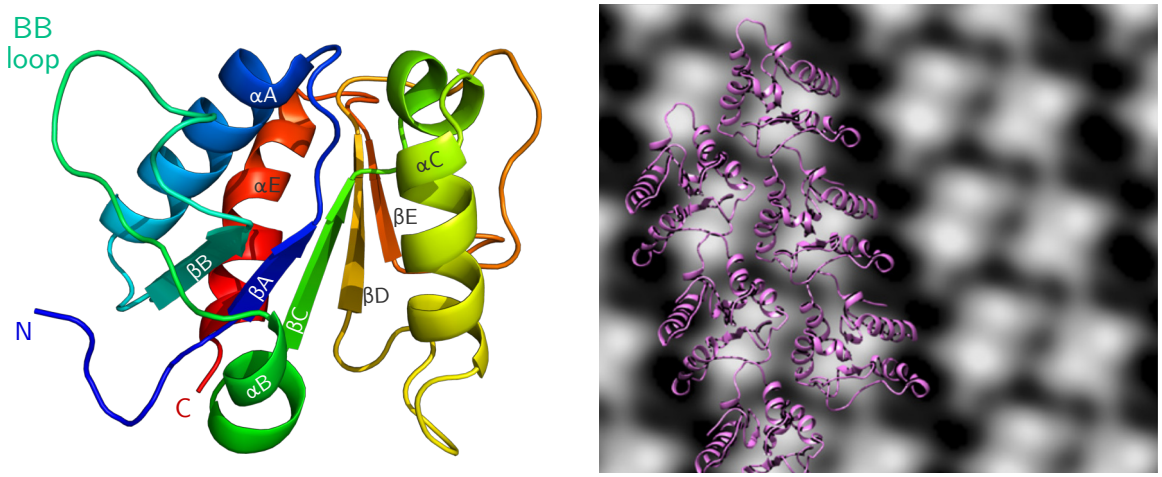

(a) solution NMR structure

(b) non-symmetrized projection map with MyD88^{TIR} assembly model

Figure 1.4: **MyD88^{TIR} structure.** **(a)** Monomeric NMR structure in solution. Figure generated with PyMOL (2020) using the PDB entry 2z5v (Berman 2000; Ohnishi et al. 2009). **(b)** A non-symmetrized projection map from cryo-EM micrographs of MyD88^{TIR} assemblies with a structural model overlaid. Figure: Ve et al. (2017).

(residues 54–109) binds the DD of IRAK4 to initiate the myddosome formation in order to transduce the signal downstream (Ve et al. 2012). C-terminally, the TIR-domain (residues 159–296) engages in homotypic TIR-TIR interactions and the structure revealed a central, parallel β-sheet holding the 5 β-strands but found only 4 surrounding α-helices, lacking αD (Figure 1.4a) (PDB ID: 2z5v, Ohnishi et al. 2009).

Recent research emphases on the importance of post-translational modifications (PTMs) for successful signal transduction: palmitoylation of cysteine 113 (in the linker region between the two domains) is required for IRAK4 recruitment (Y.-C. Kim et al. 2019) while phosphorylation of the serines 242 and 244 regulates the association of the TLR signalosome (Figure 1.5) (Xie et al. 2013).

Mutations in MyD88 can lead to severe life-threatening diseases. MyD88 deficient patients are susceptible to life-threatening bacterial infection; three mutations are currently known to be associated with this disease, namely deletion of E52, L93P, and R196C (Picard et al. 2010). Two rare mutations in the DD (S34Y and R98C) showed a significant decrease in NFκB activation that may contribute to MyD88 deficiency (George et al. 2011). The gain-of-function mutation L252P (previously stated as L265P) constitutively activates MyD88 signaling, which is often found in hematological malignancies, like diffuse large B-cell lymphoma or Waldenström's macroglobulinemia (Ngo et al. 2011; Treon et al. 2012). Other mutations found in oncogenically active MyD88 include M219T and S230N with equally strong effects on NFκB activation as L252P, and modest effects in S209R and T281P mutants compared to the wild-type protein (Ngo et al. 2011).

By using random germ-line mutagenesis, Jiang et al. (2006) created the Pococurante (Poc) phenotype in mice, which had lost all MyD88-dependent signaling, and identified I179N in the TIR-domain as the responsible mutation. Further mutagenesis analysis identified five residues (R196, D197, R217, K282, and R288) to be essential for NFκB activation *in cells* of which R196 and R288 were attributed to bind to

MAL^{TIR} *in vitro* (Ohnishi et al. 2009). Another study stated five residues essential for MyD88^{TIR} homodimerization (D162, E183, D195, K282, and R288); two of these are important for *in cell* signaling (E183 and R288) in addition to S244, which is one of the phosphorylation sites (Loiarro et al. 2013). Last, Vyncke et al. (2016) proposed four binding sites (BS) on the TIR-domain of MyD88, where BS I and III interact with MyD88^{TIR} as well as MAL^{TIR} and were thus shown to be important for NFκB activation and BS II and IV interact only with MAL^{TIR}. Of these, only the former site was shown to be important for NFκB activation (Figure 1.5).

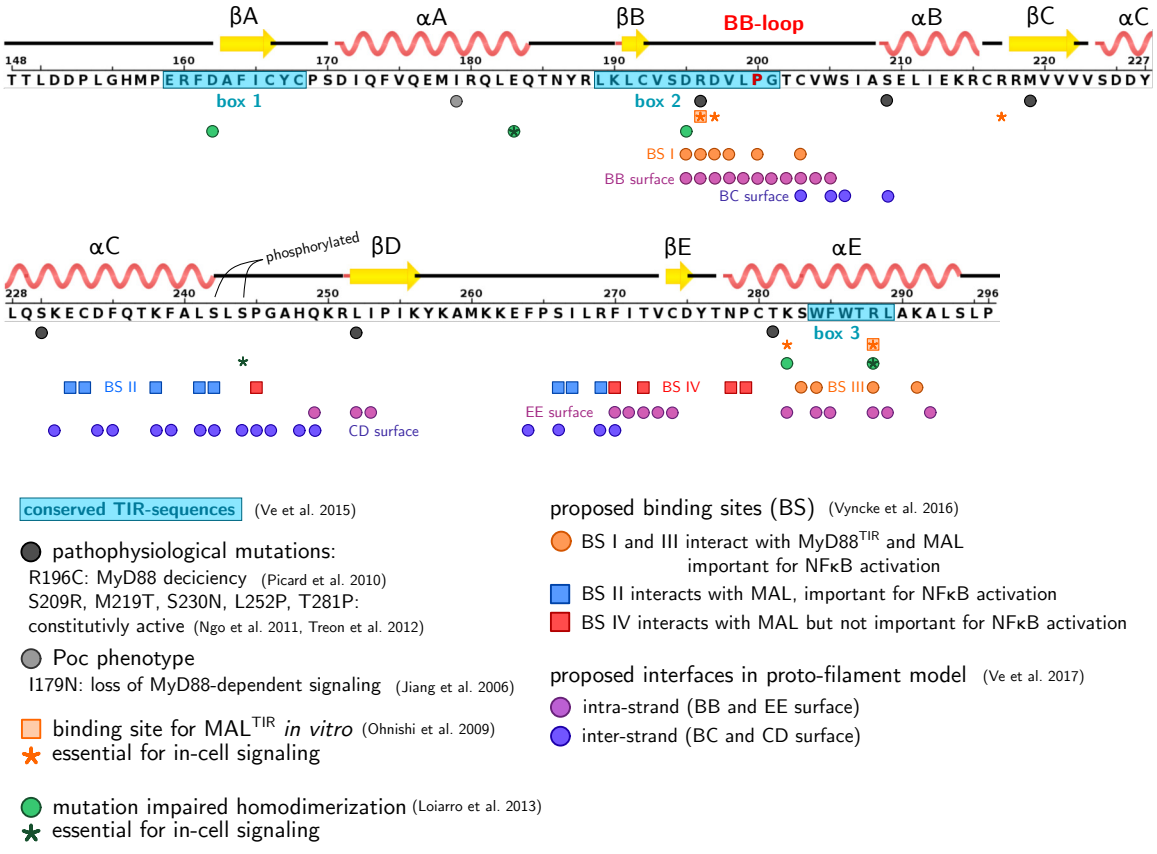

Figure 1.5: **MyD88^{TIR} sequence.** The relevant information is summarized in the sequence with the schematic representation of the secondary structures. Sequence obtained from PDB entry 2z5v (Berman 2000; Ohnishi et al. 2009) and figure generated with Inkscape (2020).

1.3 Immune Evasion Strategies of Vaccinia Virus

VACV has evolved many strategies to evade the host's immune system. The list is long and only a few, in particular those interfering with TLR signaling, will be introduced to grasp the magnitude of viral immunomodulatory proteins. Previously, VH1 has already been mentioned, which is packaged into the lateral bodies and released upon cell entry to rapidly inhibit JAK/STAT signaling and thus evade the activation of an antiviral state in the cell (Schmidt et al. 2013).

Inhibiting NFκB and IRF3 activation is a central aspect. Thus, VACV expresses a plethora of immunomodulators that target TLR signaling cascades. A46 binds the TIR-domains of all four canonical adaptors as well as those of TLR2, 3, and 4 while A49 and K7 act further downstream targeting IRAK2 and TRAF6. B14 binds IKKβ and thereby prevents the activation of the IKK complex by TAK1. A49 additionally stabilizes phosphorylated IκBα and thus prevents its degradation. M2 inhibits nuclear translocation of p56, one of the subunits of NFκB. Finally, C4, K1, and N1 have also been shown to inhibit NFκB activation but their mechanisms remain unknown. C6, K7, and N2 inhibit proteins leading to IRF3 activation (Bowie and Unterholzner 2008; Mohamed and McFadden 2009; Smith et al. 2013). Taken together, almost every step in the TLR signaling cascade is targeted by a viral immunomodulator, albeit the exact mechanisms of some are not yet known.

Another strategy of VACV is to inhibit the activity of IFNs. B18, for example, sequesters type I IFNs by sequestering them while B8 acts as a soluble decoy receptor for IFNγ. VACV has evolved similar strategy to combat cytokines and chemokines. Some cytokines require proteolytic cleavage to mature. B13 inhibits this cleavage and thus prevents maturation of cytokines. In addition, decoy receptors and proteins that bind to secreted cytokines and chemokines have been reported. For example, B15 and C12 bind cytokines while A41, B7, and B23 sequester chemokines (Smith et al. 2013). Finally, D9 and D10, as previously mentioned, degrade mRNAs thereby

preventing translation of host proteins including those expressed upon PAMP recognition essential to combat invading pathogens (Smith et al. 2013).

1.3.1 Viral Immunomodulator A46

A46 inhibits NFκB as well as IRF3 activation (Bowie et al. 2000; Stack et al. 2005). When the gene for A46 is deleted, the virus becomes attenuated (Bowie and Unterholzner 2008). In particular, A46 full-length ($A46^{FL}$) was shown to bind the TIR-domains of all four canonical TLR adaptors as well as the TIR-domains of TLR2, 3, and 4 *in vitro* (Stack and Bowie 2012; Stack et al. 2005). The BB loop of the TIR-domain contains a conserved proline across all adaptors except for MAL where it is found in the AB loop as it lacks the αB-helix (Gay et al. 2014). A46 targets the BB loop but only when the conserved proline is present (Stack and Bowie 2012).

The 240 amino acid long protein folds into two distinct domains joined via a flexible

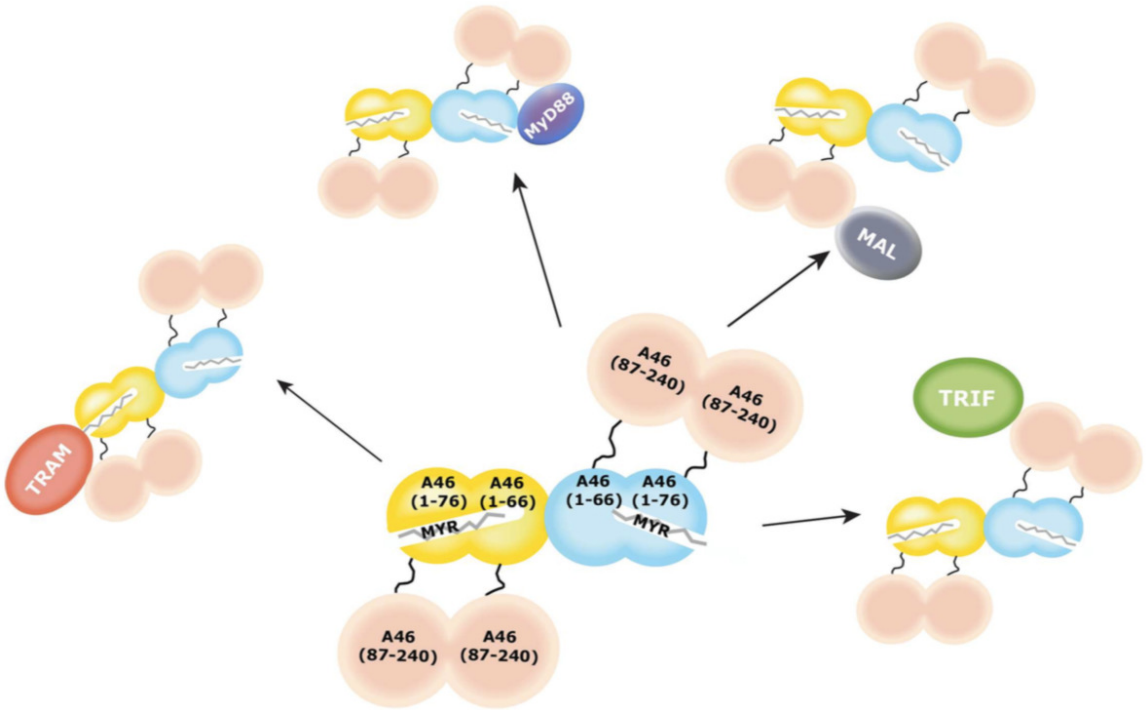

Figure 1.6: The proposed model summarizes the known interactions between the two domains of A46 and the four canonical TIR-domain containing adaptors MyD88, MAL, TRAM, and TRIF. Figure: Fedosyuk et al. (2016).

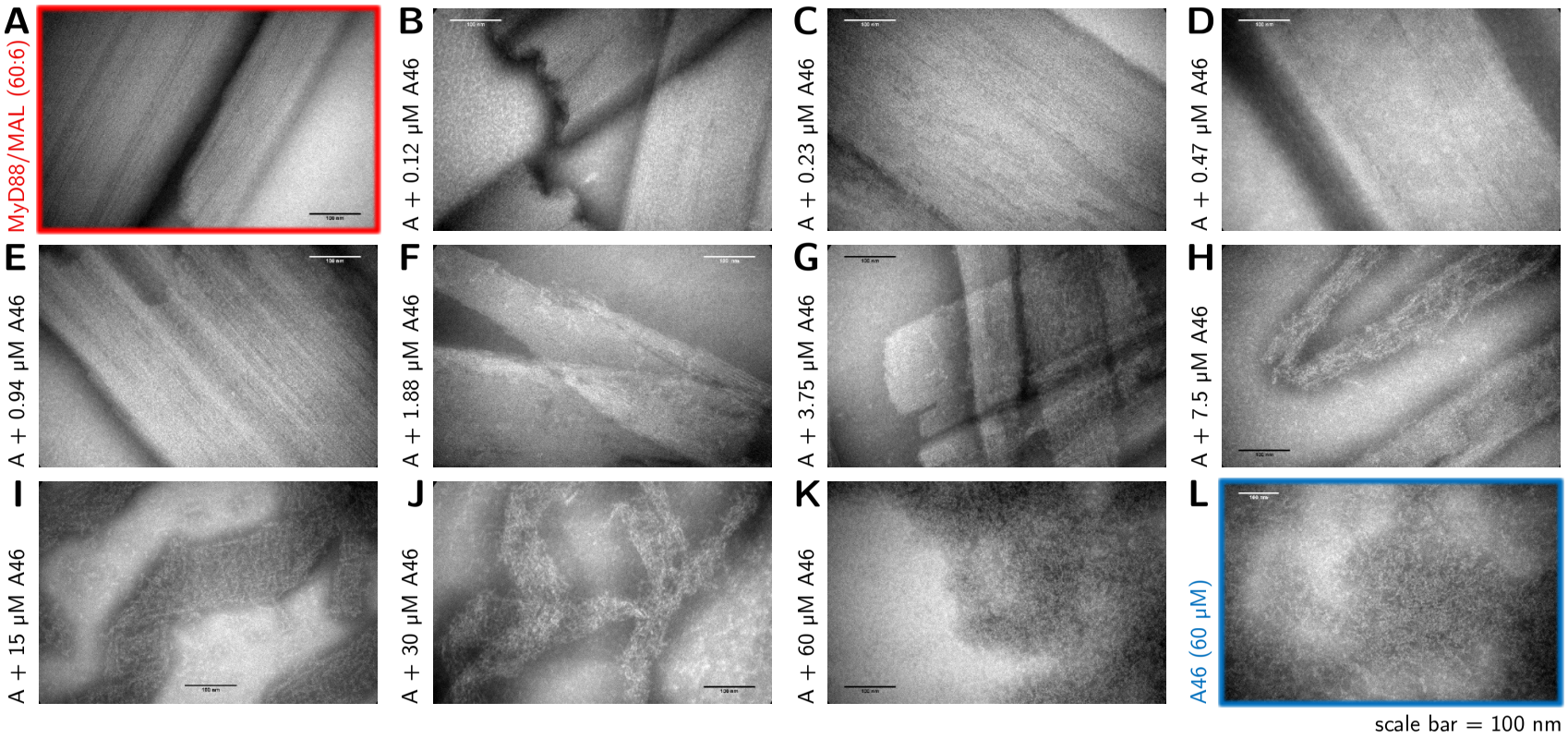

Figure 1.7: Negative-stain EM reveals the dose-dependent effects of $A46^{FL}$ on MAL^{TIR}-induced $MyD88^{TIR}$ assembly disruption. A and L depict the controls while B–K show the dose-dependent effects of $A46^{FL}$ on the assemblies. In A–K 60 µM $MyD88^{TIR}$ and 6 µM MAL^{TIR} were incubated with the stated concentration of $A46^{FL}$ at 30 °C for 16 h. Figure: Azar et al. (2020).

linker and forms a tetramer in solution. The N-terminal domain (NTD) of A46 was shown to bind MyD88^{TIR} but not MAL^{TIR} or TRAM^{TIR} while the C-terminal domain (CTD) binds MAL^{TIR}, MyD88^{TIR}, and TRAM^{TIR} *in vitro* (Fedosyuk et al. 2016; Fedosyuk et al. 2014; Y. Kim et al. 2014; Oda et al. 2011). Based on these known interactions, Fedosyuk et al. (2016) proposed a model of interacting partners and sites (Figure 1.6). Although TRAM has not yet been shown to interact with the NTD *in vitro*, the authors propose that TRAM might bind via its post-translational myristoylation into the hydrophobic tunnel.

The recent findings on visualizing TIR-domain assemblies by negative-stain EM (Ve et al. 2017) provides an easy and fast method to visualize the destructive effects of viral A46 on MAL^{TIR} as well as MyD88^{TIR} assemblies *in vitro* (Azar et al. 2020). Figure 1.7A (red boxed) depicts the unaffected MyD88^{TIR} control while B-K show the dose-dependent effects of A46^{FL} on MyD88^{TIR} assembly formation. The A46^{FL} control (blue boxed) is shown in L.

N-terminal domain

Like the full-length protein, a construct containing the residues 1–83 of A46 (NTD) forms a tetramer in solution (Fedosyuk et al. 2016). The crystal structure (PDB ID: 5ezu, Fedosyuk et al. 2016) revealed two molecules in the asymmetrical unit. One molecule (subunit A) consists of seven β-sheets while the other (subunit B) only has six β-sheets. Thus, in subunit B, the last β-sheet is not assembled and contributes to a longer, unorganized linker to the CTD. The two molecules fold into a β-sandwich (Figure 1.8a) forming a hydrophobic tunnel that harbors a myristic acid molecule and stretches subunit A and protrudes into subunit B (Figure 1.8a and 1.8b). A tetramer is formed over two asymmetrical crystal units with the two B subunits binding in a 90° angle with respect to each other (Figure 1.8c).

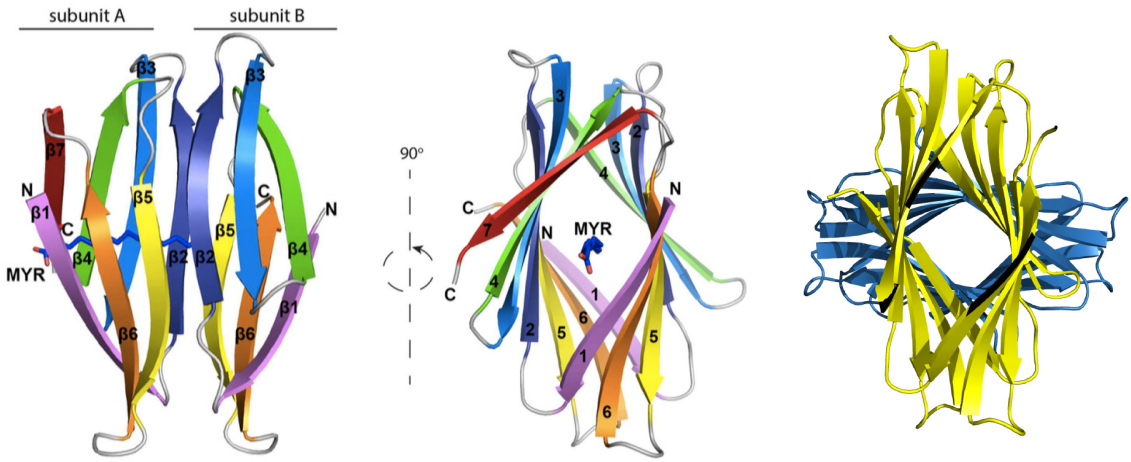

(a) dimer (b) dimer 90° turned (c) tetramer

Figure 1.8: **Crystal structure of the N-terminal domain (1-83) of A46.** **(a)** Subunit A and B form a dimer holding a molecule of myristic acid. **(b)** Dimer rotated by 90° showing the hydrophobic tunnel. **(c)** ABBA tetrameric arrangement with the two B subunits binding in a 90° angle. The two dimeric subunits are colored in yellow and blue. Figures: Fedosyuk et al. (2016).

C-terminal domain

A construct including amino acids 87–229, corresponding to the CTD, forms a dimer in solution (Fedosyuk et al. 2014). The two X-ray structures reveal seven α-helices

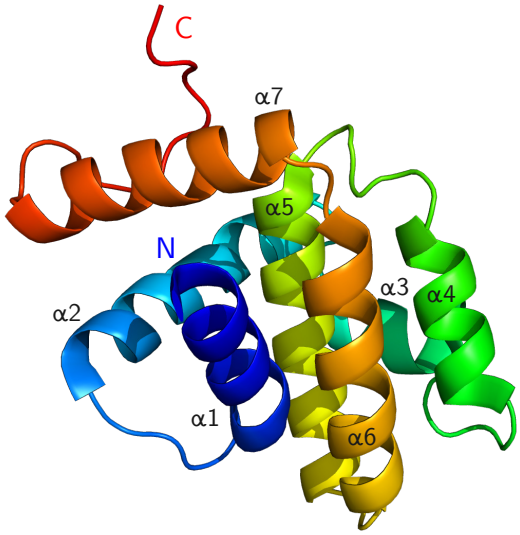

Figure 1.9: **Crystal structure of the monomeric C-terminal domain (87-229) of A46.** The sequence is colored in a rainbow spectrum. Figure produced with PyMOL (2020) using the PDB entry 4lqk (Berman 2000; Fedosyuk et al. 2016) and labeled with Inkscape (2020).

forming a Bcl-2-like fold (Figure 1.9) where helices α4 and α6 build the dimer interface (PDB ID: 4lqk and 4mos, Fedosyuk et al. 2014; Y. Kim et al. 2014, respectively).

A synthesized 11 amino acid long peptide termed viral inhibitory peptide of TLR4 (VIPER) derived from the α1-helix of the CTD of A46 (residues 88 to 98) effectively inhibits TLR4 signaling in primary human cells (Lysakova-Devine et al. 2010). Specifically, VIPER was shown to inhibit the two bridging adaptors, MAL and TRAM, but not TRIF or MyD88 *in vitro*. However, Oda et al. (2011) could not verify that the VIPER peptide binds MAL *in vitro*. Mutations corresponding to L93A (Lysakova-Devine et al. 2010) and E97A (Y. Kim et al. 2014) identified these residues as the two most critical ones for inhibiting TLR4 responses *in cells*.

Previous bioinformatical predictions of interaction sites between A46 and MyD88^{TIR} yielded multiple results (Figure 1.10) (Fedosyuk 2014). The consensus protein-protein interaction site prediction (cons-PPISP) algorithm calculated a surface patch spanning from helix α2 to the loop between α4 and α5, also covering parts of the dimer interface. The FTSite binding pocket prediction revealed three pockets for possible interaction sites, where pocket 1 overlaps with the dimer interface. Pocket 2 spans he-

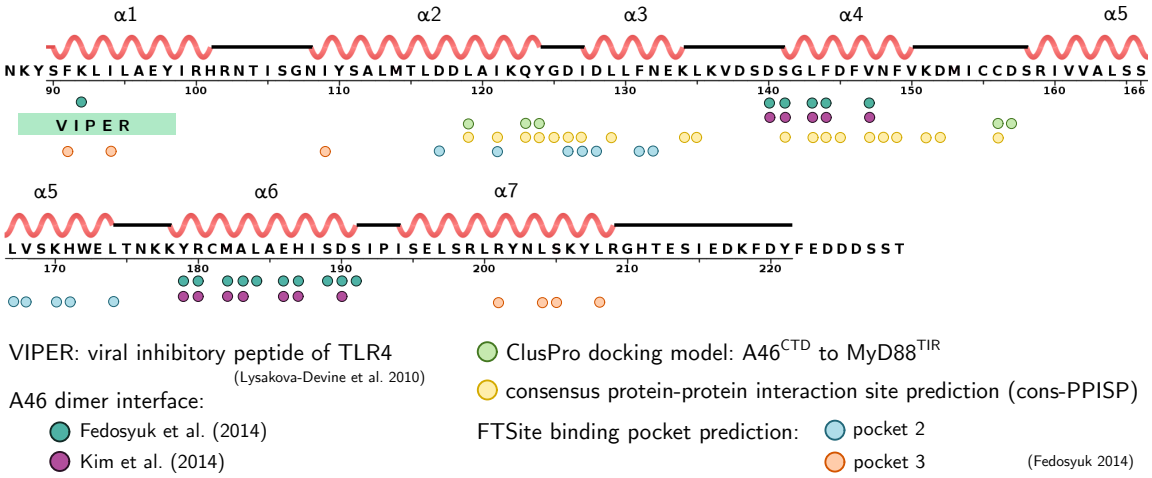

Figure 1.10: **Sequence of A46^{CTD}.** Summary of the known information and predictions are visualized in the sequence, which was obtained from PDB entry 4lqk (Berman 2000; Fedosyuk et al. 2014). Figure generated with Inkscape (2020).

lices α2 and α3 as well as the loop inbetween them, and helix α5 while pocket 3 covers parts of the VIPER sequence including one residue in helix α2 combined with parts of α7. The best obtained docking model suggested an interface involving helix α2 and the α4-α5 loop. However, these predictions still need further investigation.

2

Scientific Question

Vaccinia virus encodes numerous immunomodulator, which allow the virus to evade the host's immune system (Smith et al. 2013). Viral A46 specifically targets TLR4 signaling by interacting with the TIR-domains of all four canonical TLR adaptors (Stack et al. 2005). In particular the conserved proline in the BB-loop of the TIR-motif plays a crucial role in the interaction to A46 (Stack and Bowie 2012). However, only little is known about the interaction sites on A46. Previously, only the VIPER peptide, corresponding to a sequence in helix α1, was reported to interact with the two bridging adaptors, MAL and TRAM, but did not interact with MyD88 or TRIF (Lysakova-Devine et al. 2010). In this work, I focus on the interaction between viral A46 and human MyD88$^{\mathrm{TIR}}$.

Emphasizing on A46, I first chose one helix for mutagenesis analysis. Helix α1, holding the VIPER sequence, was discarded for the reason stated above. Helices α4 and α6 engaged in the dimer interface while helix α5 folded into the center (Fedosyuk et al. 2014; Y. Kim et al. 2014) and were thus not chosen. From the remaining three helices, I chose to investigate helix α7 because it is the most exposed helix and was bioinformatically predicted to participate in a binding pocket (Fedosyuk 2014). Within helix α7, four surface-exposed residues were selected and mutated to alanines to abolish their interaction properties. Alanine has a high propensity for helix formation and should thus not alter this secondary conformation (Pace and Scholtz 1998). The chosen four mutations were divided into two double-mutants:

Mutant 1 held R199A and Y202A while Mutant 2 consisted of K206A and R209A (Figure 2.1). To test a change of interaction, I made use of the previous observations where MyD88^{TIR} assemblies and the destruction thereof by A46 wild-type can be investigated by negative-stain EM (Azar et al. 2020; Ve et al. 2017).

I finally employed protein cross-linking coupled to mass spectrometry (XL-MS). This method permanently links residues in close proximity and can thus reveal interaction sites between proteins. For this experiment I cross-linked wild-type A46^{FL} to MyD88^{TIR} using two different cross-linking systems.

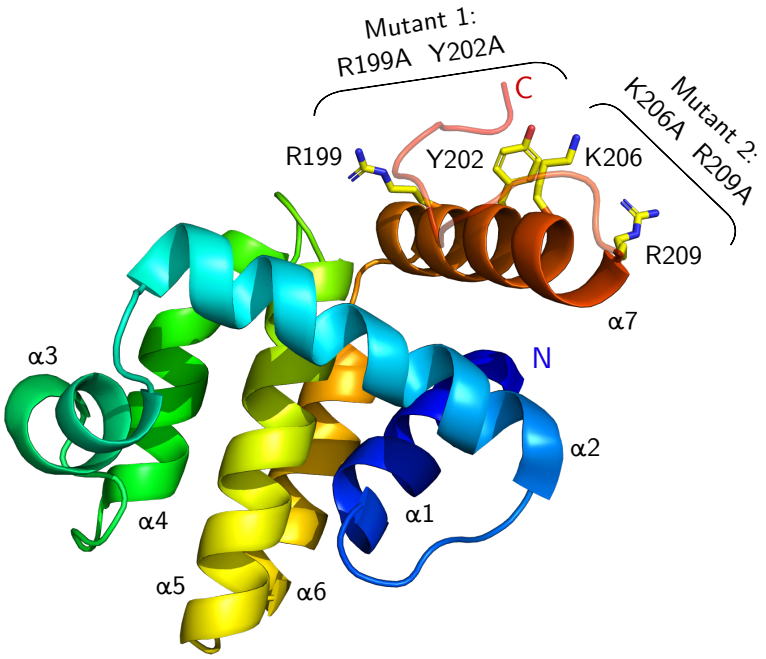

Figure 2.1: **Mutants generated in this work.** Four surface-exposed amino acids in the CTD of A46 were chosen to be mutated to alanines to generate two double-mutants to investigate changed interaction properties. Visualization generated with PyMOL (2020) using PDB entry 4lqk (Berman 2000; Fedosyuk et al. 2014), figure generated with Inkscape (2020).

3

Materials & Methods

3.1 Protein Production and Purification

3.1.1 Plasmid pSF21

The plasmid pSF21 expressed the recombinant protein construct of the full length (1–240) A46 gene sequence of the VACV Western Reserve Strain. N-terminally, an MBP sequence, a flexible asparagine/serine linker, a His_{10}-tag, the TEV protease cleavage recognition site (ENLYFQ/G) as well as three amino acids (SQQ) were added (Figure 3.1). A kanamycin resistance gene allows for selection (Fedosyuk et al. 2014).

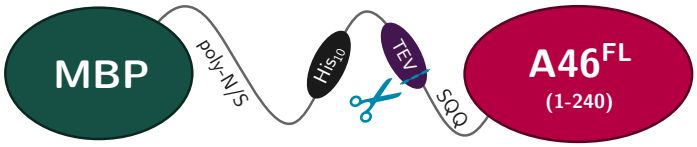

Figure 3.1: Recombinant protein expressed by the pSF21 vector.
Figure generated with Inkscape (2020).

Table 3.1: Theoretical properties of pSF21 and its constructs according to the Swiss Institute of Bioinformatics (2019).

plasmid	resistance	protein constructs	MW [kDa]	pI
pSF21	Kan	uncleaved	~ 74.6	5.52
		cleaved $A46^{FL}$	~ 28.0	4.99
		cleaved MBP-His_{10}-tag	~ 46.6	5.93

The desired mutations were introduced into pSF21 via site-directed mutagenesis by PCR according to the protocol of the Q5® Site-Directed Mutagenesis Kit (New England BioLabs® Inc. 2019), using Q5® High-Fidelity DNA Polymerase. The used primers for each mutant are listed in Table 3.2. According to above mentioned protocol, the KLD reaction was performed on the PCR products.

Table 3.2: Overview of oligonucleotides used for mutating vector pSF21.

Mutant	Mutations	Sequence (5' to 3')
Mutant 1	R199A Y202A	F: GCTATCTGCACTACGAGCCAATCTATGTAAGTATCTACG R: TCAGATATTGGAATACTATCAGATATATGTTCGGCTAATGCC
Mutant 2	K206A R209A	F: CTATGTGCGTATCTAGCCGGACACACTG R: ATTGTATCGTAGTCTAGATAGCTCAGATATTGGAATACTATCAG

Competent *E. coli* TOP10 cells were transformed and plated on kanamycin selective agar plates over night at 37 °C (or over the weekend at room temperature if applicable). Selected colonies were grown in 5 mL LB^{Kan} at 37 °C over night, shaking at 180 rpm. DNA was isolated via mini-preps according to the manufacturer's protocol (Promega 2010), their concentration measured on a Nanodrop, and sent to Microsynth AG for Sanger sequencing (primers T7 and T7term).

3.1.2 pET-MyD88^{TIR} & pET-MAL^{TIR}

The plasmids encoding the recombinant human $MyD88^{TIR}$ (pET-$MyD88^{TIR}$) and human MAL^{TIR} (pET-MAL^{TIR}) proteins were a kind gift of Bostjan Kobe (Ve et al. 2017). The vector pET-$MyD88^{TIR}$ expressed the residues 155–296 of human MyD88, followed by two residues (LE) and a His_6-tag (Figure 3.2).

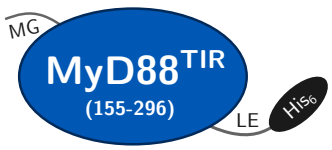

Figure 3.2: Recombinant protein expressed by the pET-$MyD88^{TIR}$ plasmid (Ve et al. 2017). Figure generated with Inkscape (2020).

The plasmid pET-MAL^{TIR} expressed the MAL^{TIR}-construct, which encompasses an N-terminal His$_6$-tag, a linker of 8 amino acids followed by the TEV protease cleavage recognition site (ENLYFQ/G), a 2 amino acid long linker to a myc-tag (EQKLISEEDL) followed by the residues 79–221 of human MAL (Figure 3.3) .

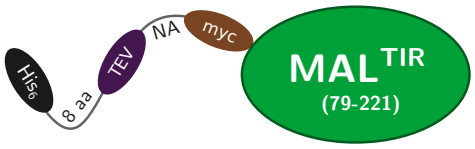

Figure 3.3: Recombinant protein expressed by the pET-MAL^{TIR} plasmid (Ve et al. 2017). Figure generated with Inkscape (2020).

Table 3.3: Properties of the plasmids and their recombinant MyD88^{TIR} and MAL^{TIR} constructs according to the Swiss Institute of Bioinformatics (2019).

plasmids	resistance	protein of interest	MW [kDa]	theor. pI
pET-MyD88^{TIR}	Kan	human MyD88 (155–296)	~ 17.9	8.80
pET-MAL^{TIR}	Amp	human MAL (79–221)	~ 19.7	5.25

3.1.3 Expression and Purification

Induction of expression for all three plasmids occurred via the T7 promotor by IPTG whereas antibiotic selection was assured by the presence of a kanamycin resistance gene for pSF21 and pET-MyD88^{TIR} or an ampicilin resistance gene on pET-MAL^{TIR}. The purification protocol for A46^{FL} was established by Fedosyuk et al. (2014) whereas Ve et al. (2017) established the protocol for the two TIR-adaptors.

E. coli BL21(DE3) competent cells were transformed and grown in LB^{Kan} or LB^{Amp} until mid-log phase (A_{600}=0.6). After induction of expression with 0.25 mM IPTG, cells were grown at 15–23 °C for 16 h, shaking at 180 rpm. Cells were harvested and per 2 L expression volume resuspended in 25 mL A46 Resuspension Buffer or MyD88/MAL Resuspension Buffer. BME and DNaseI were added freshly directly

before lysis with a cell homogenizer (EmulsiFlex-C3). For each constrcut, the soluble phase was separated from the insoluble phase by centrifugation for 60 min at the maximum speed allowed by the rotor type. Via FPLC on an ÄKTA Pure, the filtered supernatant (filter: 0.45 µm) was loaded onto a Ni-NTA His-tag affinity chromatography column (HisTrap FF 5 mL, GE Healthcare), pre-equilibrated with A46 Binding Buffer or MyD88/MAL Binding Buffer. The His-tagged proteins were eluted with 100% A46 Elution Buffer or MyD88/MAL Elution Buffer. The constructs on pSF21 (A46 wild-type and the two mutants) were cleaved by TEV protease and dialysed (7000 MWCO) against A46 Dialysis Buffer over night. HisTrap was performed twice to separate the MBP-His_{10}-tag from the protein of interest. For $MyD88^{TIR}$ and MAL^{TIR} the His-tags were not cleaved off, rendering this purification step unnecessary. The samples were concentrated using 10 000 MWCO concentration units before further purifying the samples via SEC in A46 SEC Buffer or MyD88/MAL SEC Buffer. For $A46^{FL}$ wild-type and the two mutants a HiLoad® Superdex® 200 pg column was used whereas the TIR-adaptors required a HiLoad® Superdex® 75 pg column (both GE Healthcare), either 16/600 or 26/600 in size depending on the concentrated sample volume. The fractions with few impurities (according to the SDS-polyacrylamide gel) were pooled, concentrated, buffer-exchanged to MyD88/MAL SEC Buffer without DTT, and flash-frozen for further *in vitro* analysis.

3.1.4 SDS-PAGE

Samples were denaturated using 5× loading dye at 95 °C for at least 5 min. Samples and Precision Plus Protein™ Standards (Bio-Rad) as a ladder were resolved by SDS-PAGE. Gels were stained with Coomasie Blue (0.4% Coomasie, 40% ethanol) and destained with tap water for visualization.

3.2 Negative-stain EM

15 µL of samples were incubated at 30 °C for 16 h. The samples were gently resuspended before applying 7 µL onto a glow-discharged carbon-coated Formvar grid for 60 s. The grids were washed with PTA stain before being incubated with that stain for 60 s, then blotted and allowed to air dry. The samples were imaged on an FEI Morgagni 268D transmission electron microscope operating at 80 kV with a 11-megapixel CCD Morada camera from Olympus-SIS and scale bars added to the images using ImageJ (Schneider et al. 2012).

3.3 Protein XL Coupled with MS (XL-MS)

3.3.1 BS^3

The homobifunctional cross-linker (XL), bis(sulfosuccinimidyl) suberate (BS^3) (Figure 3.4), covalently links primary amino groups, that is N-termini and side-chains of lysines, thereby introducing a spacer of 11.4 Å (Thermo Fisher Scientific Inc. 2018a). Some cross-reactivity to the hydroxyl groups of serine, tyrosine and threonine were reported in the literature (Sinz 2018). The constructs of A46$^{\mathrm{FL}}$ and MyD88$^{\mathrm{TIR}}$ have 14 and 11 lysines, respectively, while the MAL$^{\mathrm{TIR}}$ construct only contains 4 with 3 of them in the gene sequence and one in the myc-tag (see Table 3.4).

The proteins (in Assembly Buffer) were mixed on ice to the desired final concen-

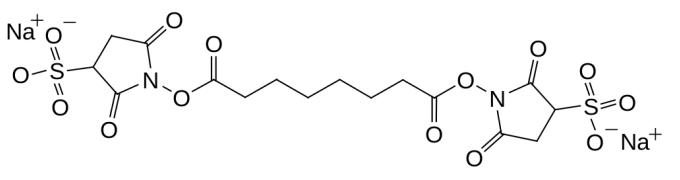

Figure 3.4: Chemical structure of bis(sulfosuccinimidyl) suberate (BS^3).
Figure: Thermo Fisher Scientific Inc. (2018a).

Table 3.4: Summary of the lysine contents of the recombinant protein constructs.

construct	Lys
$A46^{FL}$	14
$MyD88^{TIR}$	11
MAL^{TIR}	4

trations and the required amount of BS^3 was added. The samples were incubated at room temperature for the required time according to the experimental outline until the reaction was quenched with Tris (Thermo Fisher Scientific Inc. 2018a).

3.3.2 EDC and sulfo-NHS

1-ethyl-3-(3-dimethylaminopropyl)carbodiimide hydrochloride (EDC) binds carboxyl groups forming an unstable ester and can then either react with a primary amine to form a stable amide bond, which is our desired cross-linking reaction, or regenerate the original substrate. By adding N-hydroxysulfosuccinimide (sulfo-NHS) the stable amide bond is favored via an intermediate state (Figure 3.5). Thus, this combina-

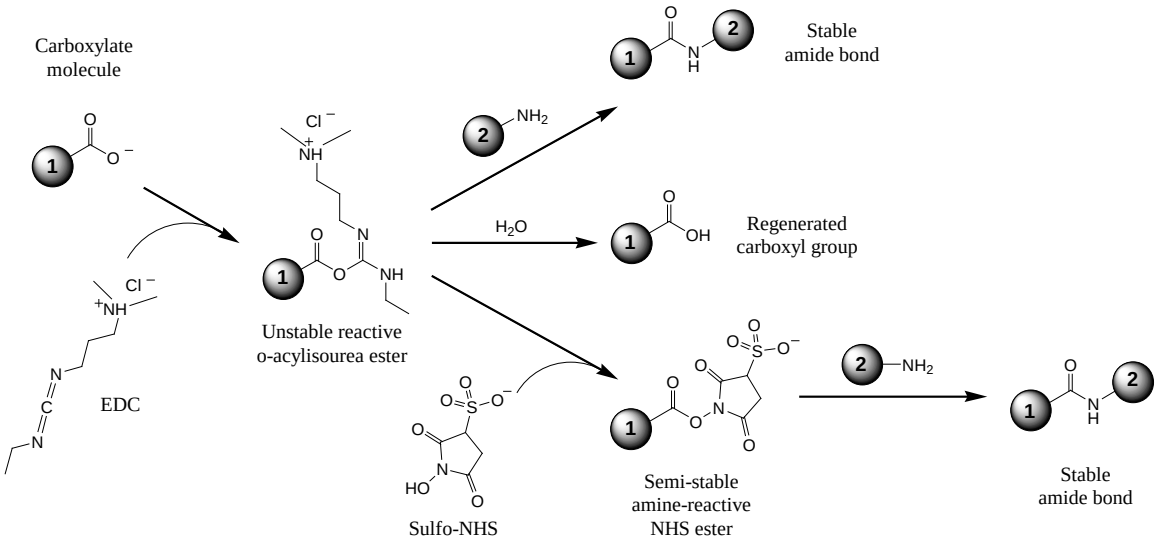

Figure 3.5: Reaction of the cross-linker system 1-ethyl-3-(3-dimethylaminopropyl)carbodiimide hydrochloride (EDC) in combination with N-hydroxysulfosuccinimide (sulfo-NHS). Figure: Thermo Fisher Scientific Inc. (2018b).

tion of reagents links carboxyl groups of the sides chains of aspartic and glutamic acids to primary amines of lysines and N-termini introducing a zero length cross-link (Thermo Fisher Scientific Inc. 2018b). Table 3.5 summarizes the amino acid composition relevant for this cross-linker system.

Table 3.5: Summary of the relevant amino acid composition of the recombinant protein constructs used with EDC & sulfo-NHS.

construct	Lys	Glu	Asp
$A46^{FL}$	14	14	23
$MyD88^{TIR}$	11	8	8
MAL^{TIR}	4	12	10

This reaction can be done in a one-step or in a two-step protocol (Max Perutz Labs Mass Spectrometry Service Facility 2018; Thermo Fisher Scientific Inc. 2017; Thermo Fisher Scientific Inc. 2018b).

One-step reaction The proteins were buffer exchanged to One-Step XL Buffer using Zeba™ Spin Desalting Columns (Thermo Fisher Scientific). According to the experimental outline, the required amounts of cross-linkers were added and the samples incubated. The reaction was quenched with BME and Tris.

Two-step reaction A46 as the first cross-link partner was buffer exchanged to Two-Step XL Buffer using Zeba™ Spin Desalting Columns (Thermo Fisher Scientific). The desired amount of EDC and sulfo-NHS were added and incubated for 15 min, when EDC was quenched with BME. The above mentioned desalting columns were used to buffer exchange the sample to Assembly Buffer for the second reaction. $MyD88^{TIR}$ or MAL^{TIR} (already in that buffer) was added as the second cross-link partner and incubated for the desired time until sulfo-NHS was quenched with Tris.

3.3.3 MS Analyses

Samples for MS were resolved by SDS-PAGE (see above) and destained using 40% ethanol and 10% acetic acid. Trypsin digest, LC-MS/MS, and proteomic analyses were conducted by Mass Spectrometry Facility at the Max Perutz Labs using the VBCF instrument pool; all data was filtered for 1% false discovery rate (FDR) at the peptide spectrum match (PSM) level and a maximum e-value of 0.001 (Azar et al. 2020).

3.4 Structural Analyses and Figure Generation

The visualized protein structures were drawn with PyMOL (2020) using the crystal structure of $A46^{CTD}$ (PDB ID: 4lqk, Fedosyuk et al. 2014), the cryo-EM structure of MAL^{TIR} (PDB ID: 5uzb, Ve et al. 2017), and the NMR structure of $MyD88^{TIR}$ (PDB ID: 2z5v, Ohnishi et al. 2009) (Berman 2000). Figures in this work were generated with GIMP (2020) and Inkscape (2020).

3.5 Buffers

Assembly Buffer	10 mM HEPES-NaOH; 150 mM NaCl; pH 7.4
A46 Resuspension Buffer	20 mM Tris-HCl pH 8.5; 100 mM NaCl; 25 mM imidazol; 5% glycerol (v/v); 15 mM BME
A46 Binding Buffer	20 mM Tris-HCl pH 8.5; 100 mM NaCl; 25 mM imidazol; 5% glycerol (v/v)
A46 Elution Buffer	20 mM Tris-HCl pH 8.5; 100 mM NaCl; 250 mM imidazol; 5% glycerol (v/v)
A46 Dialysis Buffer	20 mM Tris-HCl pH 8.5; 100 mM NaCl; 25 mM imidazol; 5% glycerol (v/v); 15 mM BME
A46 SEC Buffer	20 mM Tris-HCl pH 8.5; 5 mM DTT
MyD88/MAL Resuspension Buffer	50 mM HEPES-NaOH; 500 mM NaCl; 1 mM DTT; pH 7.4
MyD88/MAL Binding Buffer	50 mM HEPES-NaOH; 500 mM NaCl; 25 mM imidazol; pH 7.4
MyD88/MAL Elution Buffer	50 mM HEPES-NaOH; 500 mM NaCl; 250 mM imidazol; pH 7.4
MyD88/MAL SEC Buffer	10 mM HEPES-NaOH; 150 mM NaCl; 1 mM DTT; pH 7.4
One-Step XL Buffer	10 mM MES-NaOH; 150 mM NaCl; pH 6.6
Two-Step XL Buffer	10 mM MES-NaOH; 150 mM NaCl; pH 6.0

4

Results

The mutants as outlined in Figure 2.1 were successfully cloned and expressed as described in Materials & Methods. The typical purification procedure for the protein constructs on pSF21 is here shown by means of Mutant 2 (A46 K206A R209A).

4.1 Purification

4.1.1 pSF21

After bacterial expression, the lysate (T = total lysate) was centrifuged to separate the soluble phase (S) from the insoluble parts (I). After applying the soluble phase onto a HisTrap FF 5mL column (FT = flow through) and a washing step (W), the sample was eluted (E) with 100% A46 Elution Buffer (see chromatogram and gel in Figure 4.1). The elution was dialysed against A46 Dialysis Buffer over night while simultaneously cleaving off the tag using the TEV protease. In Figure 4.1, the HisTrap and the samples of the individual steps resolved by SDS-PAGE are shown, where the elution sample E clearly depicts the purified uncleaved construct at a mass of about 75 kDa and the cleaved sample confirms almost complete cleavage.

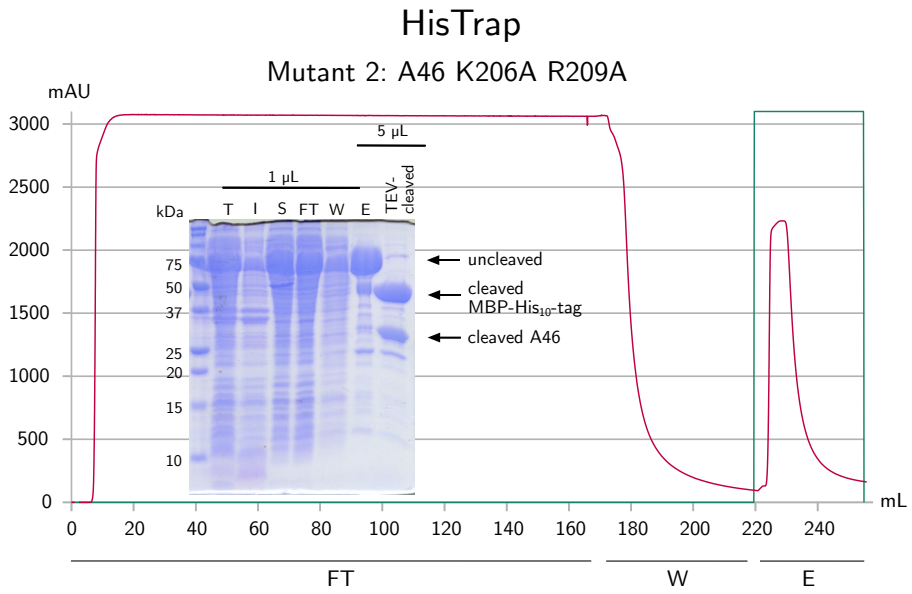

Figure 4.1: After expression of Mutant 2 (A46 K206A R209A) in *E. coli* BL21, the cells were harvested, resuspended and lysed (T = total lysate). The lysate was centrifuged to separate the insoluble phase (I) from the soluble (S), which was applied onto a HisTrap FF 5mL column calibrated with A46 Binding Buffer (FT = flow through). After a step of washing (W), the protein of interest was eluted (E) with 100% A46 Elution Buffer and dialysed over night against A46 Dialysis Buffer while being cleaved by TEV protease. The corresponding HisTrap chromatogram and the samples resolved by SDS-PAGE are shown.
Figure generated using LibreOffice (2020), GIMP (2020), and Inkscape (2020).

To separate the cleaved MBP-His_{10}-tag from the protein of interest, two purification steps using the same HisTrap column were necessary (applying FT and W in the second step). Figure 4.2 shows the two chromatograms as well as the corresponding samples resolved by SDS-PAGE. FT and W of the second step were combined and concentrated in preparation for SEC. As seen on the gel, the SEC load sample still contained some uncleaved protein and MBP-His_{10}-tag.

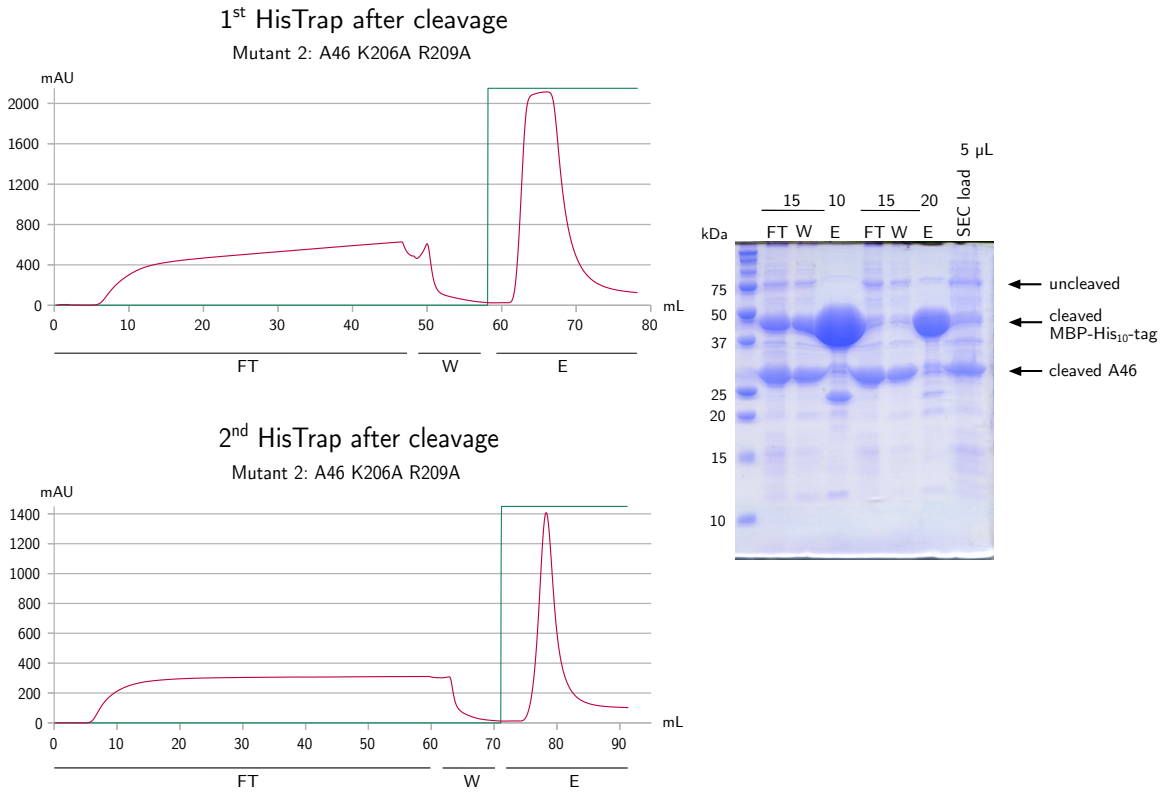

Figure 4.2: After TEV cleavage two HisTrap steps were required to separate the MBP-His_{10}-tag from the protein of interest. The two chromatograms and the corresponding samples resolved by SDS-PAGE show the progress in purification. First, the TEV-cleaved sample was applied onto a HisTrap FF 5mL column equilibrated with A46 Binding Buffer (FT = flow through) and washed (W). The cleaved MBP-His_{10}-tag was eluted with 100% A46 Elution Buffer. FT and W were combined and applied onto the same column after equilibration for the second HisTrap, which followed the same procedure as the first. FT and W were combined and concentrated for the following SEC step (SEC load).
Figure generated using LibreOffice (2020), GIMP (2020), and Inkscape (2020).

The size-exclusion chromatogram and individual SEC fractions (yellow and red) resolved by SDS-PAGE to check for purity (Figure 4.3). The first peak (fraction B10) revealed only impurities. In contrast, peaks 2 and 3 (fractions D7–H1) contained the desired protein. However, peak 2 also eluted the rest of the uncleaved product, which should be avoided. The desired, cleaved product was predominantly eluted in peak 3 and according to the gel, fractions F7–G7 contained the fewest impurities. In combination with the chromatogram, fractions F6–G9 (red) were used.

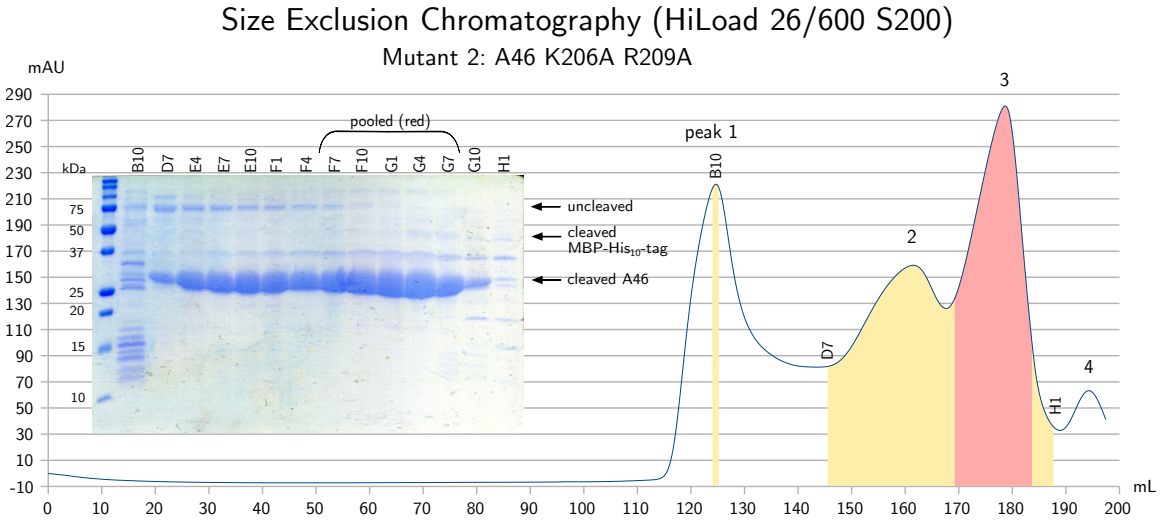

Figure 4.3: Size-exclusion chromatogram and fractions resolved by SDS-PAGE. The yellow and red fractions were resolved on the gel. Fractions F6–G9 show high amounts of cleaved protein with the fewest impurities (red fractions) and were thus used. Figure generated using LibreOffice (2020), GIMP (2020), and Inkscape (2020).

4.1.2 Purified proteins

Figure 4.4 shows all purified proteins used in this thesis for the *in vitro* assays. The expression and purification of the MAL^{TIR} construct resolved two bands. The higher band resembled the expected construct at 19.7 kDa. MS analysis revealed that the construct in the lower band was a truncated version and missed the first 27 amino acids. Parts of the myc-tag were missing but the human MAL^{TIR} sequence were intact. Wild-type $A46^{FL}$ and the two mutants have few impurities of the cleaved MBP-His_{10}-tag (46 kDa) and the uncleaved construct (75 kDa). The two mutants also have another small impurity just below the 37 kDa marker.

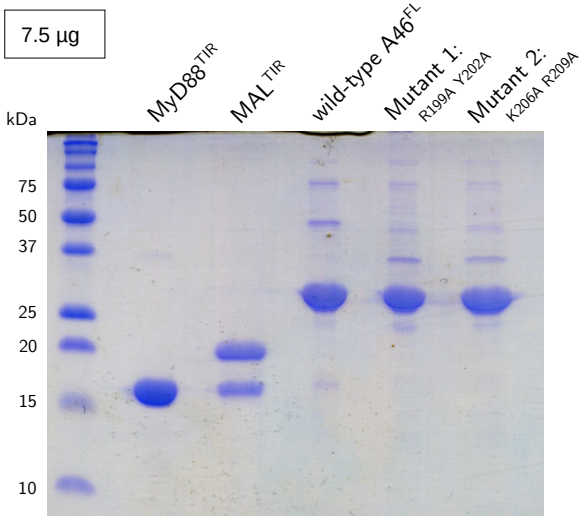

Figure 4.4: 7.5 µg samples of the five proteins used in this work for the *in vitro* assays. Figure generated using GIMP (2020) and Inkscape (2020).

4.2 Negative-stain EM

$MyD88^{TIR}$ at high concentrations forms MAL^{TIR}-induced assemblies that can be visualized by negative-stain EM (Ve et al. 2017). This data was successfully reproduced for $MyD88^{TIR}$ in Figure 4.5 at low and high magnifications. On the left, the rod-shaped 3D crystals at low magnification can be seen while on the right, the end of an assembly with straight, ordered filaments is clearly visible at high magnification.

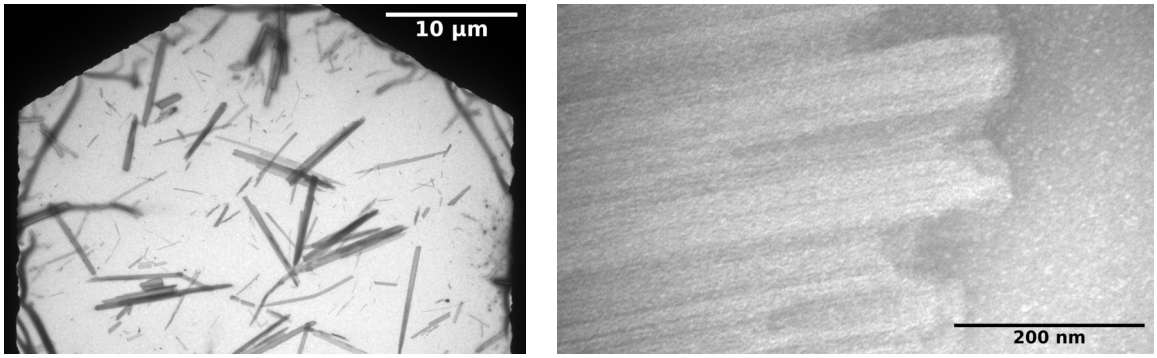

Figure 4.5: MyD88^{TIR} at high concentrations forms 3D MAL^{TIR}-induced crystals that were visualized by negative-stain EM.

Keeping in mind the dose-dependent effects of A46 in disrupting MyD88^{TIR} filament formation (Figure 1.7), the two mutants were tested at the three highest concentrations (15 µM, 30 µM, and 60 µM) as well as a twofold dose of 120 µM in negative-stain EM (Figure 4.6, Azar et al. 2020). At the top, the three concentrations of wild-type A46^{FL} are shown for comparison. Mutant 1 (R199A Y202A) shows no assembly formation at equimolar concentration and thus resembles wild-type phenotype. The filament formation was gradually regained at the two lower concentrations (15 µM and 30 µM). In contrast, mutant 2 (K206A R209A) does show filament formation at an equimolar concentration. However, the filaments do not appear completely healthy when compared to the MyD88^{TIR} control that is straight and ordered. Instead, the filaments are somewhat damaged, comparable to the filaments observed at lower concentrations of A46^{FL} wild-type. In addition, at double the concentration (120 µM) of mutant 2, filament formation was still observed but with a similar phenotype as the equimolar concentration.

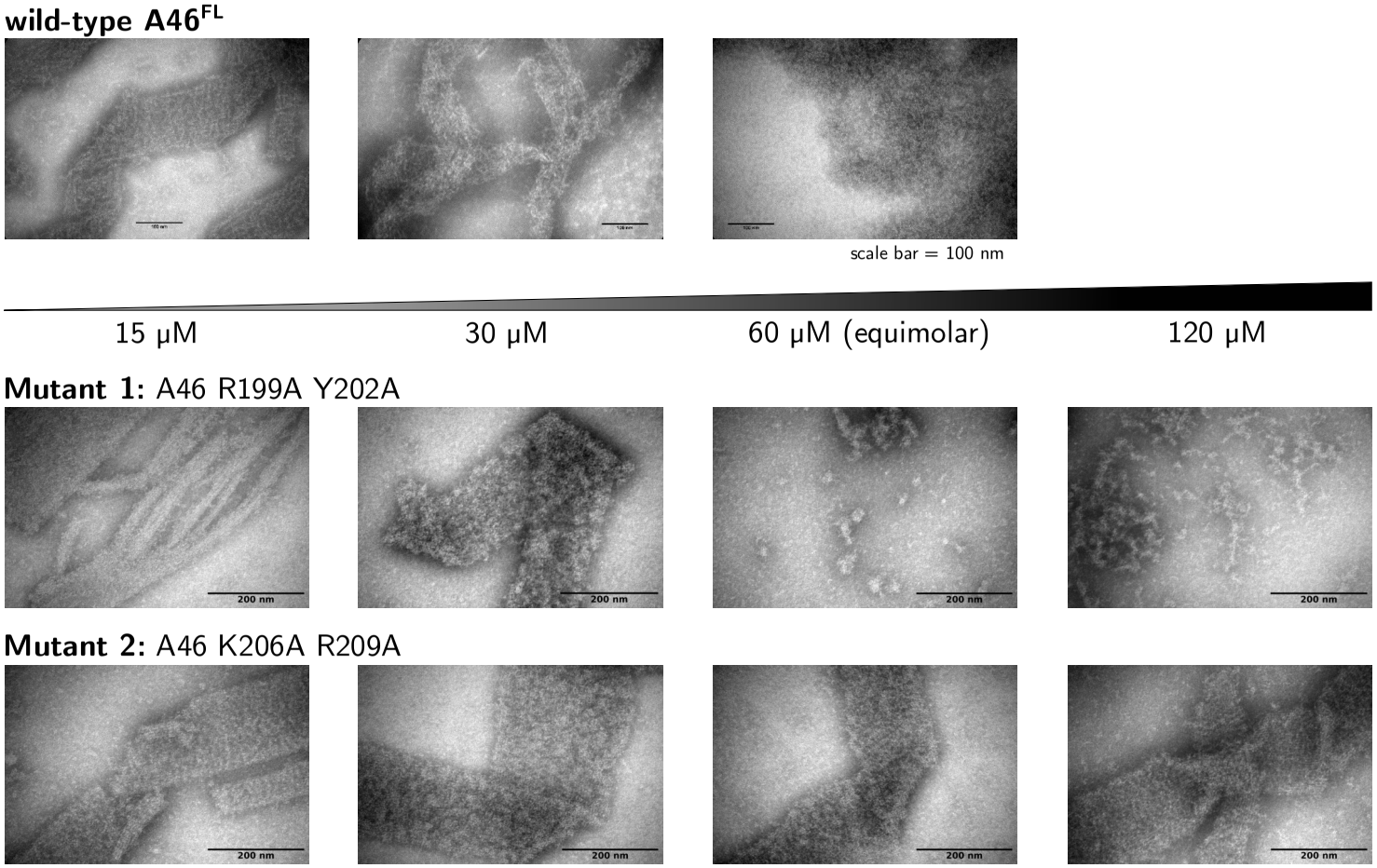

Figure 4.6: **Comparison of wild-type A46^{FL} to Mutant 1 and Mutant 2 in their effects on MAL^{TIR}-induced assembly formation of MyD88^{TIR} visualized by negative-stain EM.** Mutant 1 shows a similar phenotype as the wild-type in that it destroys the assemblies at equimolar concentrations. Mutant 2 shows incomplete assembly destruction at equimolar or twofold concentrations and thus differs from the wild-type phenotype. Figure: adapted from Azar et al. (2020).

4.3 Protein Cross-linking Coupled to MS

For protein cross-linking (XL) two chemical systems were employed: BS^3 and EDC with sulfo-NHS.

4.3.1 BS^3

For controls, each protein construct was used alone, using a 6 µM protein concentration and a 35-fold molar excess of BS^3 (see Figure 4.7). For a non-cross-linked sample of wild-type $A46^{FL}$, please refer to Figure 4.4, noting the impurities just below 50 kDa (arrow 1 in Figure 4.7) and around 75 kDa. Immediately after adding the cross-linker (0 min), three new bands appeared on the gel for the $A46^{FL}$ sample, two running close together just above 50 kDa (arrow 2) and one strong band barely entering the gel (arrow 3). On the gel of the $MyD88^{TIR}$ sample, a faint band around 37 kDa can be seen (arrow 4). MAL^{TIR} did not show any new band formation.

Bearing these controls in mind, we cross-linked $A46^{FL}$ to $MyD88^{TIR}$ (Azar et al. 2020) or MAL^{TIR}, respectively, as seen in Figure 4.8. Apart from the known bands (arrows 1-3), no new bands formed. However, there is one band that appeared in both cross-linking experiments that needs further consideration: arrow 1, which corresponds to the known impurity of $A46^{FL}$ just below 50 kDa. Consequently, this band appeared in both cross-linked samples. The particularity about this mass is that a cross-linked sample of one monomer of each constituent would result in about the same mass. $A46^{FL}$ with 28 kDa cross-linked to $MyD88^{TIR}$ with about 18 kDa results in a 46 kDa product while $A46^{FL}$ cross-linked to about 20 kDa of MAL^{TIR} would yield a 48 kDa product. The band did, however, not increase in intensity in either of the samples and thus not used for MS-analysis.

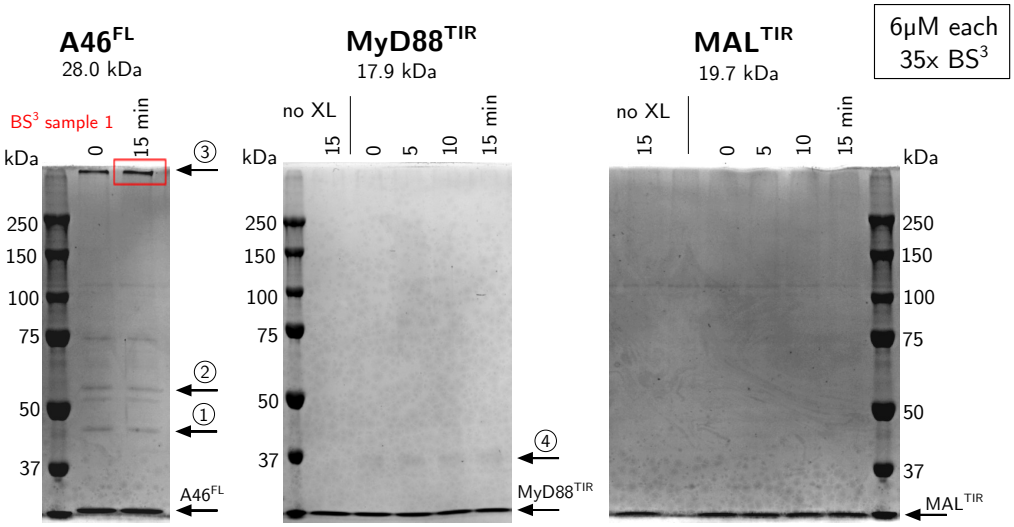

Figure 4.7: The individual proteins at 6 µM concentration cross-linked with a 35-fold molar excess of BS^3. $A46^{FL}$ without cross-linker can be seen in Figure 4.4. Arrow 1 indicates the known impurity of $A46^{FL}$ just below 50 kDa, arrow 2 indicates the two new bands appearing in both cross-linked samples of $A46^{FL}$, and arrow 3 indicates a dominant band at the top of the gel. When cross-linking $MyD88^{TIR}$ to itself, only a faint band appears (arrow 4). Cross-linking MAL^{TIR} does not show any new band formations. The red boxed condition was used to prepare samples for mass spectrometry analysis.
Figure generated using GIMP (2020) and Inkscape (2020).

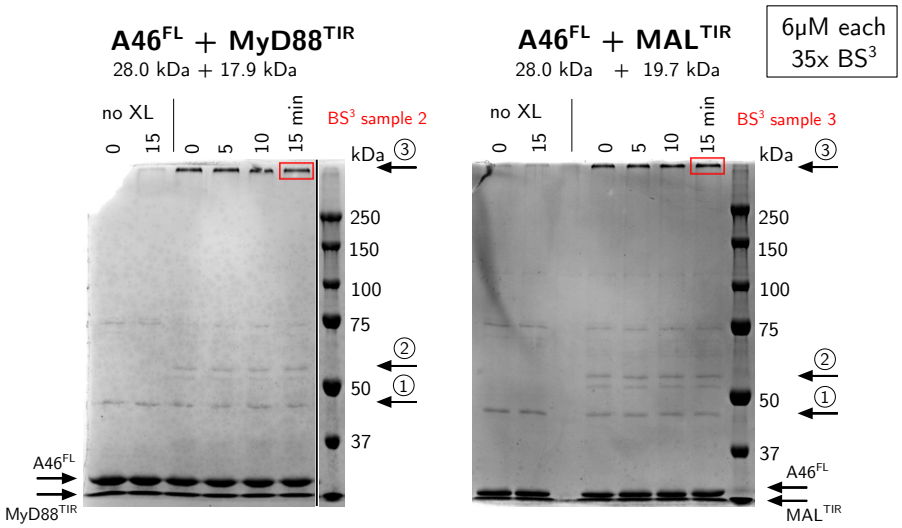

Figure 4.8: Cross-linking $A46^{FL}$ to $MyD88^{TIR}$ (Azar et al. 2020) or MAL^{TIR}; all proteins at 6 µM concentration with a 35-fold molar excess of BS^3. The known impurity and the known cross-linked bands are indicated as in Figure 4.7 with arrows 1, 2 and 3. The red boxed conditions were used to prepare samples for mass spectrometry analysis.
Figure generated using GIMP (2020) and Inkscape (2020).

In addition, both samples of 0 min XL already showed a strong band of oligomerized protein at the top. However, decreasing the concentration to a 5-fold molar excess of BS^3, as shown in Figure 4.9, did not yield any new band formations. Arrows 1, 2, and 3 point at the known bands from the previous figures. In both 90 min samples, the desired band at arrow 1 slightly increased representing the desired cross-link product while the band for the cross-linked A46 dimer (arrow 2) appeared as well. At the same time, the 90 min samples showed strong bands at the top of the gels (arrow 3).

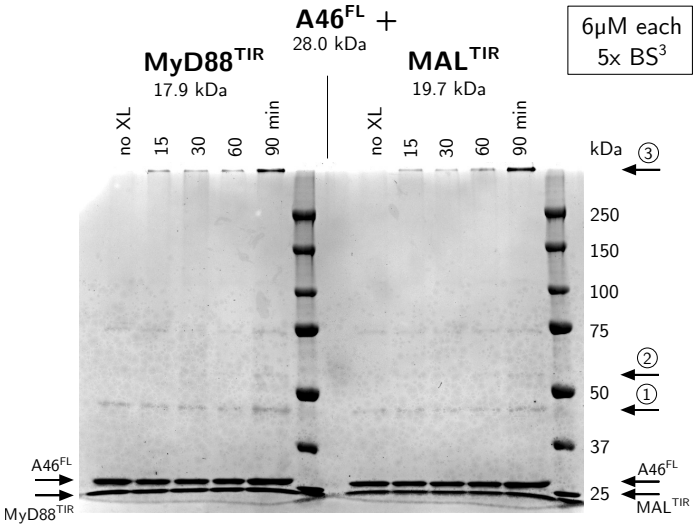

Figure 4.9: Cross-linking $A46^{FL}$ with $MyD88^{TIR}$ or MAL^{TIR}, respectively, using a 5-fold molar excess of BS^3. Arrow 1 indicates the known impurity of $A46^{FL}$ and the position where the desired cross-linked product of heterodimers would run. Figure generated using GIMP (2020) and Inkscape (2020).

In conclusion, we used the red boxed conditions of 35-fold BS^3 in Figures 4.7 and 4.8 to prepare samples for MS to see whether either of the adaptors $MyD88^{TIR}$ or MAL^{TIR} cross-linked to wild-type $A46^{FL}$ in the top band.

4.3.2 MS analysis of BS^3 cross-links

The obtained cross-links are summarized in Table 4.1, where the cross-linked sites of the constructs are translated into the actual residues. The N-terminal methionine of $MyD88^{TIR}$ had been cleaved off during expression (Wingfield 2017) and thus, residue

2 of MyD88^{TIR} corresponds to the N-terminus of the construct. Figure 4.10 depicts the XL-map of sample 2 (MyD88^{TIR} and A46^{FL}) (Azar et al. 2020; Combe et al. 2015).

Table 4.1: MS results summarized for the three samples cross-linked with BS^3. The cross-link sites of the protein constructs are translated into the residues corresponding to the protein sequence. PSM: peptide spectrum match where the intensity of red correlations to the count.

BS^3 cross-links									PSMs		
									sample 1	2	3
cross-link type	protein 1	cross-link site 1	residue	protein 2	cross-link site 2	residue	best e-value	best score	A46^{FL}	MyD88^{TIR} & A46^{FL}	MAL^{TIR} & A46^{FL}
cross-link	A46^{FL}	1	N-term	A46^{FL}	181	K177	1.376E-09	2.218E-03	0	0	1
cross-link	A46^{FL}	162	S158	A46^{FL}	210	K206	4.364E-04	5.123E-02	1	0	0
loop-link	A46^{FL}	181	K177		182	K178	9.938E-20	2.551E-16	11	6	7
loop-link	A46^{FL}	179	T175		182	K178	3.048E-05	2.186E-09	0	1	0
loop-link	A46^{FL}	182	K178		183	Y179	9.538E-08	1.045E-03	2	0	2
loop-link	A46^{FL}	210	K206		211	Y207	1.548E-06	9.910E-03	1	0	0
cross-link	MyD88^{TIR}	2	N-term	MyD88^{TIR}	2	N-term	4.152E-05	4.557E-02	0	1	0
cross-link	MyD88^{TIR}	2	N-term	MyD88^{TIR}	38	K190	1.613E-12	1.463E-12	0	31	0
cross-link	MyD88^{TIR}	2	N-term	MyD88^{TIR}	98	K250	3.065E-16	8.395E-06	0	4	0
cross-link	MyD88^{TIR}	2	N-term	MyD88^{TIR}	104	K256	1.723E-06	1.288E-06	0	13	0
cross-link	MyD88^{TIR}	2	N-term	MyD88^{TIR}	110	K262	2.193E-07	5.670E-10	0	4	0
cross-link	MyD88^{TIR}	98	K250	MyD88^{TIR}	104	K256	9.021E-04	3.133E-02	0	1	0
cross-link	MyD88^{TIR}	104	K256	MyD88^{TIR}	109	K261	3.110E-17	2.176E-04	0	9	0
cross-link	MyD88^{TIR}	104	K256	MyD88^{TIR}	110	K262	6.908E-07	4.844E-10	0	2	0
loop-link	MyD88^{TIR}	38	K190		42	S194	6.949E-04	2.125E-07	0	1	0
loop-link	MyD88^{TIR}	92	S244		98	K250	5.506E-10	6.754E-14	0	13	0
loop-link	MyD88^{TIR}	104	K256		105	Y257	4.772E-05	3.371E-08	0	2	0
loop-link	MyD88^{TIR}	109	K261		110	K262	2.745E-36	2.222E-15	0	16	0
loop-link	MyD88^{TIR}	139	K291		142	S294	8.073E-23	1.161E-16	0	14	0
cross-link	A46^{FL}	210	K206	MyD88^{TIR}	2	N-term	8.558E-08	7.260E-05	0	7	0
cross-link	A46^{FL}	210	K206	MyD88^{TIR}	104	K256	2.710E-05	5.166E-02	0	1	0

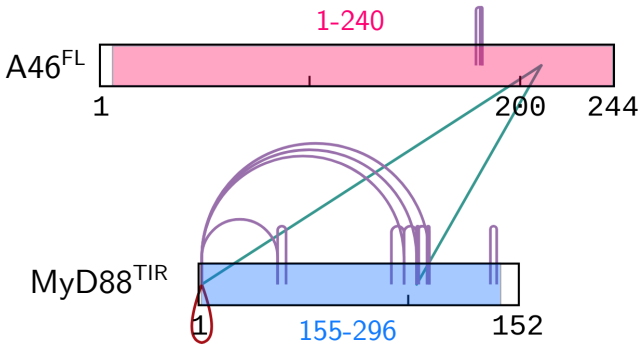

Figure 4.10: Cross-link map of A46^{FL} and MyD88^{TIR}(sample 2), using BS^3 as a cross-linker (Azar et al. 2020). The gene sequence of each protein within its construct is depicted in color. The XL-map was generated via Combe et al. (2015) and labeled with Inkscape (2020).

Six links were found within or between $A46^{FL}$ constructs; four of them being intramolecular links, while one of the other two links involved the N-terminus of the construct linked to K177 and the second connects S158 to K206 of $A46^{FL}$.

Cross-linking $A46^{FL}$ to $MyD88^{TIR}$ revealed an appreciable number of cross-links between or within $MyD88^{TIR}$ constructs; five of these involved the N-terminus, another five were loop-links, while three linked within or between $MyD88^{TIR}$ constructs, which are of more interest. Most notably, K256 was involved in all of these three connections, being linked to K250, K261, and K262. Two cross-links were recorded between $A46^{FL}$ and $MyD88^{TIR}$, one involving the N-terminus of the latter, while the second joined the above mentioned K256 of MyD88 to K206 of A46.

No cross-links between $A46^{FL}$ and MAL^{TIR} or between MAL^{TIR} constructs were found.

4.3.3 EDC and sulfo-NHS

The above results show that BS^3 did not yield any cross-linked products that could be resolved by SDS-PAGE. Thus, we employed a different cross-linker system: EDC in combination with sulfo-NHS links carboxylates to primary amines (Thermo Fisher Scientific Inc. 2018b).

In a first cross-linker titration, the one-step procedure with 30 min XL incubation was tested on the individual constructs at 6 µM protein concentration each (Figure 4.11). The samples of $A46^{FL}$ show a dominant band at the top (arrow 3, numbered as in section 4.3.1) while lacking the bands just above 50 kDa. The samples with $MyD88^{TIR}$ or MAL^{TIR} did not show any complex formation whatsoever.

Figure 4.12 depicts cross-linking $A46^{FL}$ to the two adaptor proteins under the same titration conditions. Note in both titrations the gradual decrease of the $A46^{FL}$ monomer bands at 28 kDa with a parallel build-up of cross-linked protein at the top of the gel with increasing XL concentrations (arrow 3). This is in contrast to the previ-

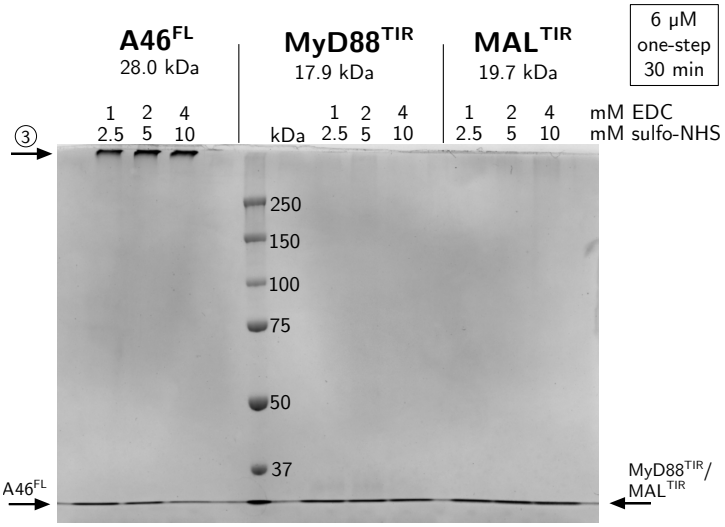

Figure 4.11: EDC and sulfo-NHS cross-linker titration in a one-step experiment with the individual proteins $A46^{FL}$, $MyD88^{TIR}$, and MAL^{TIR} at 6 µM concentration each, after 30 min of cross-linking. Arrow 3 indicates a dominant band in the $A46^{FL}$ samples not resolved, at the top of the gel. When cross-linking $MyD88^{TIR}$ or MAL^{TIR} to themselves no cross-linked band can be visualized. Figure generated using GIMP (2020) and Inkscape (2020).

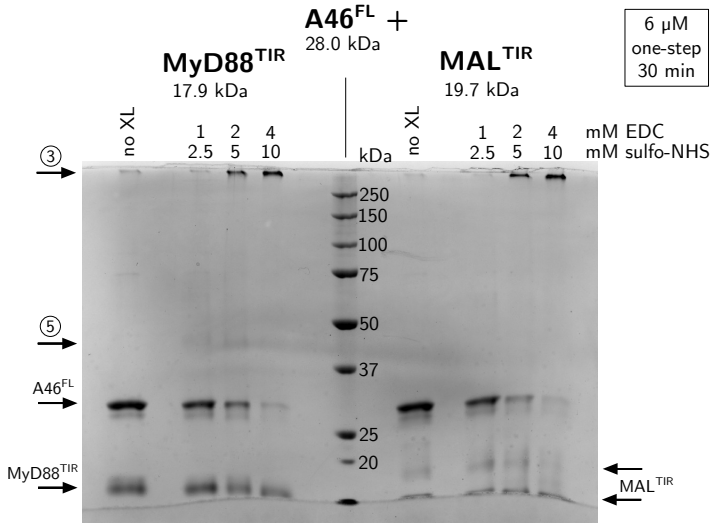

Figure 4.12: Cross-linking $A46^{FL}$ to the two adaptors, $MyD88^{TIR}$ or MAL^{TIR}, at 6 µM concentration each in a one-step cross-linker titration using EDC and sulfo-NHS. With increasing cross-linker concentration the cross-linked proteins at the top of the gel build up (arrow 3) while, in parallel, the $A46^{FL}$ monomer decreases. Arrow 5 points at the desired cross-linked product, only appearing faintly. Figure generated using GIMP (2020) and Inkscape (2020).

ous figure 4.11 where the top band appeared stronger at all three XL-concentrations. However, more remarkably are the samples with $MyD88^{TIR}$ where at the two lowest concentrations a new faint band appeared (arrow 5), while the build-up of cross-linked protein at the top of the gel becomes less. The desired cross-linked product of a heterodimer would run at about 46 kDa, which corresponds to the band at arrow 5; yet, the band is still faint and further optimization was needed.

For the two-step protocol, a larger volume and thus more protein was needed due to the buffer exchange step. This also diluted the sample resulting in an unknown end-concentration. Although this is the recommended protocol (Thermo Fisher Scientific Inc. 2017), this approach did not yield any usable data (not shown). In a second trial, we used 60 µM of protein to counteract the dilution factor. A faint smear of the desired mass below 50 kDa formed (data not shown). Therefore, we used the higher protein concentrations in a one-step cross-linking reaction. Again, we observed a faint band at the desired mass but this time it was sharper than in the two-step procedure (data not shown).

In a final attempt, we incubated the proteins under assembly conditions (60 µM $MyD88^{TIR}$ with 6 µM MAL^{TIR} and 60 µM $A46^{FL}$ for 16 h at 30 °C) before adding the cross-linkers. In one experiment, BS^3 was applied; however, no new band formation was observed (data not shown). In parallel, a one-step experiment with 5 mM EDC and 12.5 mM sulfo-NHS was conducted (Figure 4.13). The build-up of cross-linked $A46^{FL}$ at the top of the gel is known from the previous experiments. Yet, here this build-up occurred gradually over time, while at the same time the desired cross-linked product between a monomer of $A46^{FL}$ and a monomer $MyD88^{TIR}$ (arrow 5) became more distinct and stronger than observed before at lower protein concentrations (Figure 4.12). It is noteworthy that these bands become fainter with longer XL incubation, giving best results after 5 and 10 min. In addition, the known band of presumably two cross-linked TIR-adaptors (arrow 4) appeared in the control without

A46^{FL} as well as in the experiment with A46^{FL}. Taken together, these conditions were used to prepare samples for MS (red boxes) (Azar et al. 2020). During MS sample preparation, however, the gels shrank and a separation of the two faint bands in box 1 was no longer possible.

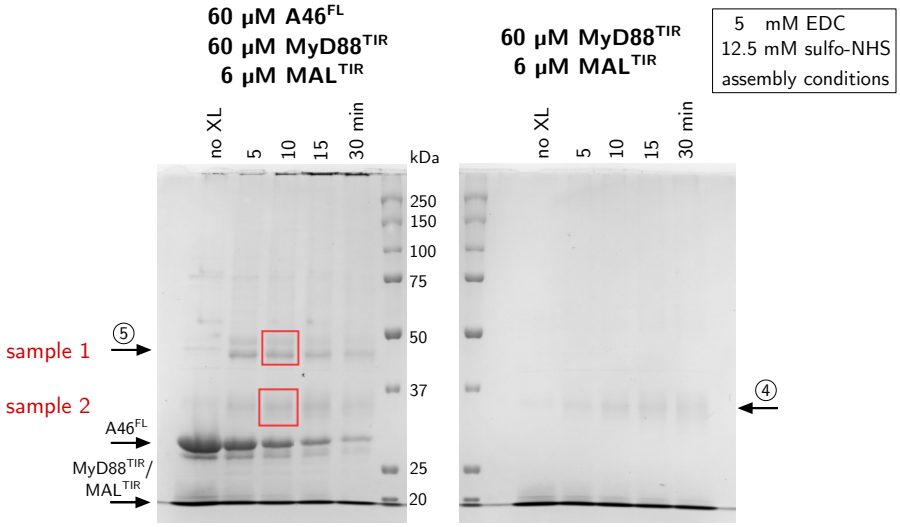

Figure 4.13: Cross-linking A46^{FL} to MyD88^{TIR} under assembly conditions using 5 mM EDC and 12.5 mM sulfo-NHS (Azar et al. 2020). As a control on the right gel no A46^{FL} was added. Arrow 4 indicates a faint band below 37 kDa while arrow 5 points at two bands below 50 kDa. The red boxed conditions were used to prepare samples for MS, the top box corresponds to sample 1 and the lower box to sample 2.
Figure generated using GIMP (2020) and Inkscape (2020).

For MAL^{TIR} filament formation we optimized the protocol of Ve et al. (2017) to a concentration of 120 µM MAL^{TIR}. However, due to limited protein amounts, the experimental setup here had to be adapted: the final working concentration for the assembly conditions was only 65 µM and for the control not MAL^{TIR} alone was used but A46^{FL}, in contrast to the previous setups (Figure 4.14). On the left, arrow 6 points at the desired cross-link product between A46^{FL} and MAL^{TIR} at 48 kDa. Recalling the known impurity of A46^{FL} with the same mass, we see a faint band on the right in the control, however, on the left the band increased remarkably in intensity. Similar to the experiment with MyD88^{TIR}, that band started strongly in the 5 min sample and fainted with longer XL incubation time. During MS sample

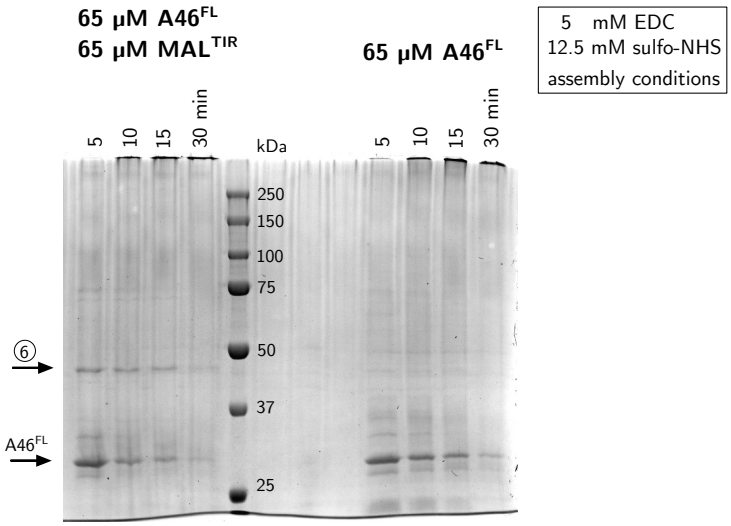

Figure 4.14: Preliminary data of cross-linking 65 µM $A46^{FL}$ to 65 µM MAL^{TIR} under assembly conditions, using 5 mM EDC and 12.5 mM sulfo-NHS. As a control on the right only $A46^{FL}$ was used. Arrow 6 indicates a band just below 50 kDa, where the desired cross-linked product would run.
Figure generated using GIMP (2020) and Inkscape (2020).

preparation these bands could not be reproduced in such an intensity and thus, the experiment needs to be repeated.

4.3.4 MS Analysis of EDC & sulfo-NHS Cross-links

Table 4.2 depicts the MS results using EDC in combination with sulfo-NHS on $MyD88^{TIR}$ assembly conditions disrupted by $A46^{FL}$. Recalling Figure 4.13, sample 1 corresponded to approximately 46 kDa (arrow 5) which would match $A46^{FL}$ cross-linked to one adaptor, whereas sample 2 was the band below 37 kDa, which would match the masses of two cross-linked adaptors; both assumptions were confirmed by MS analysis. In the table, the cross-linked sites of the constructs are again translated into the actual residue numbers of the protein sequence and the results grouped into five main groups: (i) links within the $A46^{FL}$ sequence, (ii) $A46^{FL}$ linked to MAL^{TIR}, (iii) $A46^{FL}$ linked to $MyD88^{TIR}$ with first the N-termini links grouped, (iv) links within the $MyD88^{TIR}$ sequence again first N-termini and loop-links listed, and (v) MAL^{TIR} linked to $MyD88^{TIR}$. Additionally, Figure 4.15 visualizes the cross-links via

two XL-maps (Azar et al. 2020; Combe et al. 2015).

In brief, six cross-links were recorded within $A46^{FL}$, with four loop-links. Of the other two, the MBP-tag of the uncleaved protein was involved in one (as seen in Figure 4.4 the sample of $A46^{FL}$ did still contain some uncleaved construct) while the other record linked D42 to K45. MAL^{TIR} linked to $A46^{FL}$ in three individual links, all covalently binding the N-terminus of $A46^{FL}$ to the myc-tag of the MAL^{TIR}-construct. The links between $A46^{FL}$ and $MyD88^{TIR}$ as well as those within $MyD88^{TIR}$ were of most interest and will therefore be presented in more detail later. Last, MAL^{TIR} linked to $MyD88^{TIR}$ in thirteen individual links, where eleven involve the myc-tag of the MAL^{TIR}-construct and linked the N-terminus of $MyD88^{TIR}$.

Cross-links between $A46^{FL}$ & $MyD88^{TIR}$ and within $MyD88^{TIR}$

These recordings help to understand $MyD88^{TIR}$ filament formation and disruption thereof by $A46^{FL}$ *in vitro*; they are, however, not useful for physiological interpretations. More than half of the links between $A46^{FL}$ and $MyD88^{TIR}$ involved the N-terminus of either of the two constructs, while cross-links within $MyD88^{TIR}$ showed about a third involving its N-terminus. Within the $MyD88^{TIR}$ construct, three loop-links were found, linking residues close in sequence; these are not relevant for $MyD88^{TIR}$ assembly formation.

Regarding cross-links between $A46^{FL}$ and $MyD88^{TIR}$ not invovling N-termini, ten need further consideration: K190, E232, D234, K250, K258, K261, and K262 of MyD88 cross-linked to six residues on A46, namely E133, D152, K206, E213, D235, and E237; all of which reside in the CTD of A46. Previously only K206 had linked to K256 of $MyD88^{TIR}$ with BS^3.

Looking at the cross-links within the $MyD88^{TIR}$ sequence (these could be between two monomers or within one molecule) ten links did not involve the N-terminus. Four residues had previously been reported with BS^3, while four new sites engaged in cross-links, namely E183, E232, D234, and E263.

Table 4.2: MS results of MyD88^{TIR} under assembly conditions cross-linked to A46^{FL} using EDC and sulfo-NHS. The cross-linked sites of the constructs are translated into the residues corresponding to the full-length protein sequence. PSM: peptide spectrum match where the intensity of red correlations to the count.

EDC & sulfo-NHS cross-links

cross-link type	protein 1	cross-link site 1	residue	protein 2	cross-link site 2	residue	best e-value	best score	PSMs Band 1	PSMs Band 2
cross-link	uncleaved A46	52	MBP (K)	uncleaved A46	314	MBP (D)	5.148E-04	5.023E-02	2	0
cross-link	A46^{FL}	46	D42	A46^{FL}	49	K45	4.907E-17	7.348E-02	2	0
loop-link	A46^{FL}	48	D44		49	K45	1.931E-17	9.176E-09	1	0
loop-link	A46^{FL}	140	K136		142	D138	3.998E-27	1.431E-10	1	0
loop-link	A46^{FL}	140	K136		144	D140	3.602E-10	4.287E-10	2	0
loop-link	A46^{FL}	221	D217		222	K218	3.369E-17	3.250E-08	1	0
cross-link	A46^{FL}	1	N-term	MAL^{TIR}	31	myc (E)	4.957E-07	8.123E-05	1	0
cross-link	A46^{FL}	1	N-term	MAL^{TIR}	32	myc (E)	7.265E-10	6.280E-03	1	0
cross-link	A46^{FL}	1	N-term	MAL^{TIR}	33	myc (D)	2.233E-04	4.956E-04	1	0
cross-link	A46^{FL}	1	N-term	MyD88^{TIR}	7	E159	4.301E-27	1.608E-03	3	0
cross-link	A46^{FL}	1	N-term	MyD88^{TIR}	31	E183	3.896E-06	1.915E-03	2	0
cross-link	A46^{FL}	1	N-term	MyD88^{TIR}	82	D234	2.295E-05	1.402E-02	1	0
cross-link	A46^{FL}	1	N-term	MyD88^{TIR}	111	E263	1.224E-14	2.321E-04	5	0
cross-link	A46^{FL}	8	D4	MyD88^{TIR}	2	N-term	1.094E-08	5.376E-02	1	0
cross-link	A46^{FL}	38	D34	MyD88^{TIR}	2	N-term	1.594E-10	3.497E-03	2	0
cross-link	A46^{FL}	44	E40	MyD88^{TIR}	2	N-term	2.426E-05	4.671E-01	1	0
cross-link	A46^{FL}	52	D48	MyD88^{TIR}	2	N-term	1.707E-06	1.716E-03	2	0
cross-link	A46^{FL}	62	D58	MyD88^{TIR}	2	N-term	1.459E-09	1.373E-02	2	0
cross-link	A46^{FL}	72	E68	MyD88^{TIR}	2	N-term	9.564E-08	2.802E-03	4	0
cross-link	A46^{FL}	130	D126	MyD88^{TIR}	2	N-term	2.201E-07	7.177E-05	2	0
cross-link	A46^{FL}	132	D128	MyD88^{TIR}	2	N-term	2.633E-08	2.867E-04	2	0
cross-link	A46^{FL}	137	E133	MyD88^{TIR}	2	N-term	1.806E-16	3.395E-07	7	0
cross-link	A46^{FL}	142	D138	MyD88^{TIR}	2	N-term	2.792E-06	1.120E-02	2	0
cross-link	A46^{FL}	149	D145	MyD88^{TIR}	2	N-term	1.856E-05	2.967E-03	2	0
cross-link	A46^{FL}	156	D152	MyD88^{TIR}	2	N-term	9.879E-14	3.314E-08	7	0
cross-link	A46^{FL}	217	E213	MyD88^{TIR}	2	N-term	3.863E-11	1.967E-04	7	0
cross-link	A46^{FL}	220	E216	MyD88^{TIR}	2	N-term	1.048E-20	4.398E-03	6	0
cross-link	A46^{FL}	221	D217	MyD88^{TIR}	2	N-term	2.821E-07	1.134E-05	5	0
cross-link	A46^{FL}	224	D220	MyD88^{TIR}	2	N-term	1.506E-05	1.350E-03	5	0
cross-link	A46^{FL}	227	E223	MyD88^{TIR}	2	N-term	3.966E-07	2.157E-03	5	0
cross-link	A46^{FL}	228	D224	MyD88^{TIR}	2	N-term	4.566E-07	2.038E-04	7	0
cross-link	A46^{FL}	229	D225	MyD88^{TIR}	2	N-term	7.915E-08	3.299E-04	6	0
cross-link	A46^{FL}	230	D226	MyD88^{TIR}	2	N-term	1.490E-10	8.454E-06	9	0
cross-link	A46^{FL}	239	D235	MyD88^{TIR}	2	N-term	7.834E-10	2.425E-03	5	0
cross-link	A46^{FL}	241	E237	MyD88^{TIR}	2	N-term	4.473E-06	1.698E-08	8	2
cross-link	A46^{FL}	243	D239	MyD88^{TIR}	2	N-term	4.482E-12	6.500E-05	12	0
cross-link	A46^{FL}	137	E133	MyD88^{TIR}	109	K261	4.451E-04	1.057E-02	1	0
cross-link	A46^{FL}	156	D152	MyD88^{TIR}	109	K261	9.019E-07	6.079E-03	1	0
cross-link	A46^{FL}	156	D152	MyD88^{TIR}	110	K262	1.063E-10	1.727E-03	1	0
cross-link	A46^{FL}	210	K206	MyD88^{TIR}	80	E232	6.239E-08	6.576E-03	1	0
cross-link	A46^{FL}	210	K206	MyD88^{TIR}	82	D234	3.214E-07	2.873E-03	1	0
cross-link	A46^{FL}	217	E213	MyD88^{TIR}	98	K250	9.450E-08	1.484E-01	1	0
cross-link	A46^{FL}	239	D235	MyD88^{TIR}	106	K258	6.964E-04	8.338E-03	1	0
cross-link	A46^{FL}	239	D235	MyD88^{TIR}	110	K262	9.754E-16	1.931E-01	1	0
cross-link	A46^{FL}	241	E237	MyD88^{TIR}	38	K190	8.588E-04	3.432E-03	1	0
cross-link	A46^{FL}	241	E237	MyD88^{TIR}	106	K258	2.307E-04	3.107E-03	1	0

cross-link type	protein 1	cross-link site 1	residue	protein 2	cross-link site 2	residue	best e-value	best score	PSMs Band 1	PSMs Band 2
cross-link	MyD88^{TIR}	2	N-term	MyD88^{TIR}	7	E159	3.747E-10	1.743E-07	0	6
cross-link	MyD88^{TIR}	2	N-term	MyD88^{TIR}	31	E183	1.338E-08	4.060E-14	0	4
cross-link	MyD88^{TIR}	2	N-term	MyD88^{TIR}	43	D195	1.356E-10	1.331E-07	0	5
cross-link	MyD88^{TIR}	2	N-term	MyD88^{TIR}	80	E232	4.125E-11	8.063E-22	0	5
cross-link	MyD88^{TIR}	2	N-term	MyD88^{TIR}	82	D234	6.676E-09	2.063E-14	0	6
cross-link	MyD88^{TIR}	2	N-term	MyD88^{TIR}	111	E263	2.466E-12	3.548E-20	0	33
loop-link	MyD88^{TIR}	79	K231		80	E232	4.838E-16	2.940E-05	3	1
loop-link	MyD88^{TIR}	82	D234		86	K238	5.719E-36	1.541E-10	3	2
loop-link	MyD88^{TIR}	110	K262		111	E263	2.853E-06	1.790E-03	2	7
cross-link	MyD88^{TIR}	31	E183	MyD88^{TIR}	98	K250	2.916E-13	1.085E-08	0	2
cross-link	MyD88^{TIR}	31	E183	MyD88^{TIR}	109	K261	2.776E-06	1.323E-09	0	2
cross-link	MyD88^{TIR}	31	E183	MyD88^{TIR}	110	K262	9.643E-08	1.405E-11	0	3
cross-link	MyD88^{TIR}	80	E232	MyD88^{TIR}	98	K250	1.114E-13	3.131E-08	0	2
cross-link	MyD88^{TIR}	80	E232	MyD88^{TIR}	110	K262	1.052E-04	1.023E-07	0	2
cross-link	MyD88^{TIR}	82	D234	MyD88^{TIR}	98	K250	1.422E-09	1.444E-06	0	1
cross-link	MyD88^{TIR}	82	D234	MyD88^{TIR}	110	K262	1.696E-05	2.557E-10	0	1
cross-link	MyD88^{TIR}	98	K250	MyD88^{TIR}	111	E263	4.322E-04	1.417E-04	0	1
cross-link	MyD88^{TIR}	104	K256	MyD88^{TIR}	111	E263	2.054E-04	3.001E-11	0	1
cross-link	MyD88^{TIR}	110	K262	MyD88^{TIR}	111	E263	8.284E-05	1.667E-08	0	1
cross-link	MAL^{TIR}	31	myc (E)	MyD88^{TIR}	2	N-term	3.289E-10	2.759E-17	1	11
cross-link	MAL^{TIR}	31	myc (E)	MyD88^{TIR}	98	K250	5.964E-16	2.086E-12	0	5
cross-link	MAL^{TIR}	31	myc (E)	MyD88^{TIR}	109	K261	1.654E-04	3.110E-01	0	1
cross-link	MAL^{TIR}	31	myc (E)	MyD88^{TIR}	110	K262	3.726E-05	2.457E-12	0	2
cross-link	MAL^{TIR}	32	myc (E)	MyD88^{TIR}	2	N-term	3.498E-15	2.944E-16	0	13
cross-link	MAL^{TIR}	32	myc (E)	MyD88^{TIR}	98	K250	3.746E-07	4.034E-07	0	4
cross-link	MAL^{TIR}	32	myc (E)	MyD88^{TIR}	104	K256	1.076E-05	2.725E-06	0	1
cross-link	MAL^{TIR}	32	myc (E)	MyD88^{TIR}	110	K262	1.464E-06	1.459E-14	0	5
cross-link	MAL^{TIR}	33	myc (D)	MyD88^{TIR}	2	N-term	5.620E-14	2.175E-18	0	6
cross-link	MAL^{TIR}	33	myc (D)	MyD88^{TIR}	98	K250	5.398E-04	1.214E-01	0	1
cross-link	MAL^{TIR}	33	myc (D)	MyD88^{TIR}	110	K262	1.237E-10	4.011E-07	0	1
cross-link	MAL^{TIR}	159	D203	MyD88^{TIR}	2	N-term	6.603E-04	2.973E-02	0	1
cross-link	MAL^{TIR}	167	E211	MyD88^{TIR}	2	N-term	1.327E-06	4.176E-16	0	3

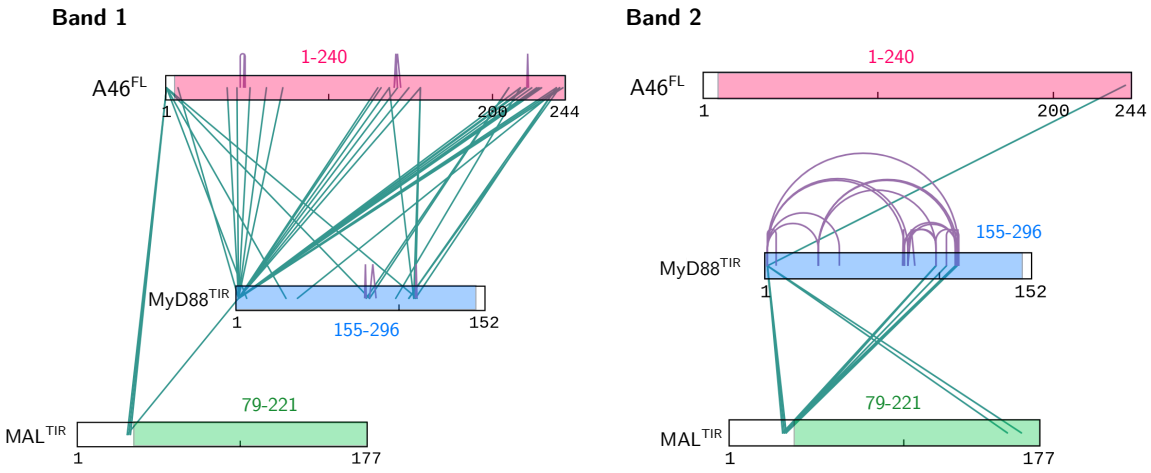

Figure 4.15: The XL maps of band 1 and band 2 using EDC and sulfo-NHS as cross-linkers (Azar et al. 2020). The gene sequence of each protein within its construct is depicted in color. The XL-maps were generated via Combe et al. (2015) and labeled with Inkscape (2020).

5

Discussion

Viral A46 has been shown to inhibit TLR4 signaling by targeting the TIR-domains of all four canonical adaptors (Stack et al. 2005) but the exact mechanism remains elusive. Here, we set out to shed light onto the interaction sites between A46 and the TIR-domain of human MyD88. $MyD88^{TIR}$ forms assemblies *in vitro*, which are destroyed by A46 wild-type (Azar et al. 2020; Ve et al. 2017). We used site-directed mutagenesis to mutate four surface-exposed residues in the last helix $\alpha 7$ of A46 to alanines and generated two double-mutants (Mutant 1: A46 R199A Y202A, Mutant 2: A46 K206A R209A). After successful recombinant bacterial expression and purification, we tested, whether the mutants altered the destruction of the $MyD88^{TIR}$ assemblies and observed a change in Mutant 2. Protein cross-linking coupled to MS confirmed K206 and gave insight into further residues interacting with MyD88.

5.1 Negative-stain EM

After successfully reproducing the published data on the visualization of $MyD88^{TIR}$ assembly formation by negative-stain EM (Figure 4.5 and Ve et al. 2017) on the one hand and on the other hand the concentration-dependent destruction of these assemblies by wild-type $A46^{FL}$ (Azar et al. 2020), two mutants were tested under these conditions to investigate, whether the mutated residues change the destruction of the adaptor assemblies (Figure 4.6). Mutant 1 (A46 R199A Y202A) shows similar effects on $MyD88^{TIR}$ assembly as the wild-type. Thus, judging from this data, neither

R199 nor Y202 of A46 seem to be part of the interface to MyD88^{TIR}.

In contrast, Mutant 2 (A46 K206A R209A) showed a different phenotype than the wild-type A46 protein. At equimolar concentration (60 µM), some assembly formation, albeit unusual, can still be witnessed. The structure of the MyD88^{TIR} assemblies did not resemble the unaffected control (i.e. straight and ordered filaments) but appeared damaged to a comparable extent to lower doses of the wild-type (30 µM or 15 µM). Interestingly, decreasing the concentration of Mutant 2 did not noticeably change this phenotype. In addition, doubling the concentration of Mutant 2 (120 µM) showed no increase in destruction. Thus, one or both of these residues seem to be involved in the interactive interface to MyD88^{TIR}. One caveat might be that the folding of the protein is hampered, given that the residues are towards the C-terminus of the structured part. However, both mutations are to alanines, which is known to have a high propensity for helix formation (Pace and Scholtz 1998). In addition, the mutants showed the same purification behavior as the wild-type protein and their proper folding was confirmed by circular dichroism (CD) analysis (Azar et al. 2020).

In conclusion, this experiment gives a first indication that K206 and/or R209 of A46 are involved in the interaction to the TIR-domain of MyD88 while R199 and Y202 are not.

5.2 Protein XL Coupled to MS

To confirm the involvement of residues K206 and/or R209 in the interaction of A46^{FL} to MyD88^{TIR}, we used two different cross-linking systems: BS^3 on the one hand and EDC in combination with sulfo-NHS on the other. BS^3 covalently links primary amines and introduces a spacer of 11.4 Å (Thermo Fisher Scientific Inc. 2018a), while the EDC/sulfo-NHS system is a so-called zero spacer cross-linker that links carboxylates to primary amines (Thermo Fisher Scientific Inc. 2018b). In the first part of this

section, the experimental setup will be discussed by means of SDS-PAGE analyses while the second part focuses on the interpretation of the MS examination of linked residues leading to a possible mode of interaction between MyD88^{TIR} and A46^{FL}.

5.2.1 SDS-PAGE Results of BS^3

A46^{FL}

In Figure 4.7, when cross-linking wild-type A46^{FL} at 6 µM concentration to itself, we see a strong band at the top of the gel (arrow 3). Here, we most likely observe polymerization of A46 monomers, given that we added cross-linker to a protein that contains 14 lysines.

On the same gel, two well-resolved bands (arrow 2) appear just above the 50 kDa marker. To note, full-length A46 and the NTD tetramerize in solution (Fedosyuk et al. 2016) while the CTD dimerizes (Fedosyuk et al. 2014). A dimer of A46^{FL} theoretically has a mass of 56 kDa, which would explain one of these bands. Nevertheless, this does not explain the presence of the second band. However, the purified A46^{FL} sample does contain some impurities (Figure 4.4), which could not be separated from the viral protein by SEC. Thus, they might have been cross-linked and now appear as that second band.

Surprisingly, there is no strong band appearing where a tetramer of A46^{FL} with theoretical 112 kDa would run. Just above the 100 kDa marker a faint band is visible but not at all comparable to the strength of the other two bands just above the 50 kDa marker. Possibly, a cross-linked tetramer is too rapdily oligomerized and shows up in the top band (arrow 3). Still, it is surprising how rapidly these new bands form upon addition of 35-fold molar excess of BS^3. Already after 0 min (mind the handling of the test tubes), we see the same phenotype as with a 15 min incubation.

Upon decreasing the cross-linker concentration to 5-fold molar excess (Figure 4.9), there was still an accumulation at the top of the gel over time (90 min). However,

the visualization of the presumable dimer band was poorer. Thus, a 35-fold molar excess of cross-linker yielded the better results and was used for further experiments.

MyD88^{TIR}

When cross-linking MyD88^{TIR} at 6 µM concentration to itself, only one faint band (arrow 4 in Figure 4.7) around or just below the 37 kDa marker becomes visible. A cross-link of two MyD88^{TIR} molecules theoretically yields a 36 kDa product, which would match this faint band and is in agreement with previous observations of MyD88^{TIR} dimerization (Loiarro et al. 2013). The low concentration and the fact that MyD88^{TIR} only forms assemblies at high concentrations and in the presence of MAL^{TIR} (Ve et al. 2017), could explain why only a faint band formed.

A46^{FL} and MyD88^{TIR}

Figure 4.8 on the left shows the cross-linking results of A46^{FL} with MyD88^{TIR} resolved by SDS-PAGE. The arrows 1, 2, and 3 point to the known bands from the controls (compare to Figure 4.7). In particular, arrow 1 points at the known impurity of A46^{FL}, which presumably is a leftover of the cleaved MBP-His$_{10}$-tag at about 46 kDa. This is also the mass at which a desired cross-linked product of heterodimer between A46^{FL} and MyD88^{TIR} would run. However, the band does not increase in intensity after adding cross-linker, which suggests that no desired product was formed. Still, some cross-linked heterodimer might have accumulated in the top band with A46^{FL} (arrow 3), Thus, these conditions were used to prepare a sample for MS-analysis.

MAL^{TIR}

MAL^{TIR} at 6 µM concentration does not give any cross-linked band formation when used on itself (Figure 4.7). On the one hand, this is not surprising given that this recombinant protein construct of MAL^{TIR} only has four lysines. Three lysines are part of the human protein sequence (K84, K158, K210) while the fourth is in the myc-tag following the N-terminal His$_6$-tag. On the other hand, MAL^{TIR} is reported

to form filaments by itself; however, *in vitro* higher concentrations are required for this phenomenon (Ve et al. 2017).

By inspecting the published cryo-EM structure of the MAL^{TIR} filament (Ve et al. 2017, PDB ID: 5uzb), we can investigate the three above mentioned lysines, their potential cross-link sites, and their theoretical distances. In each of the Figures 5.1–5.3, one lysine with their closest cross-linking options is depicted, with distances in Å.

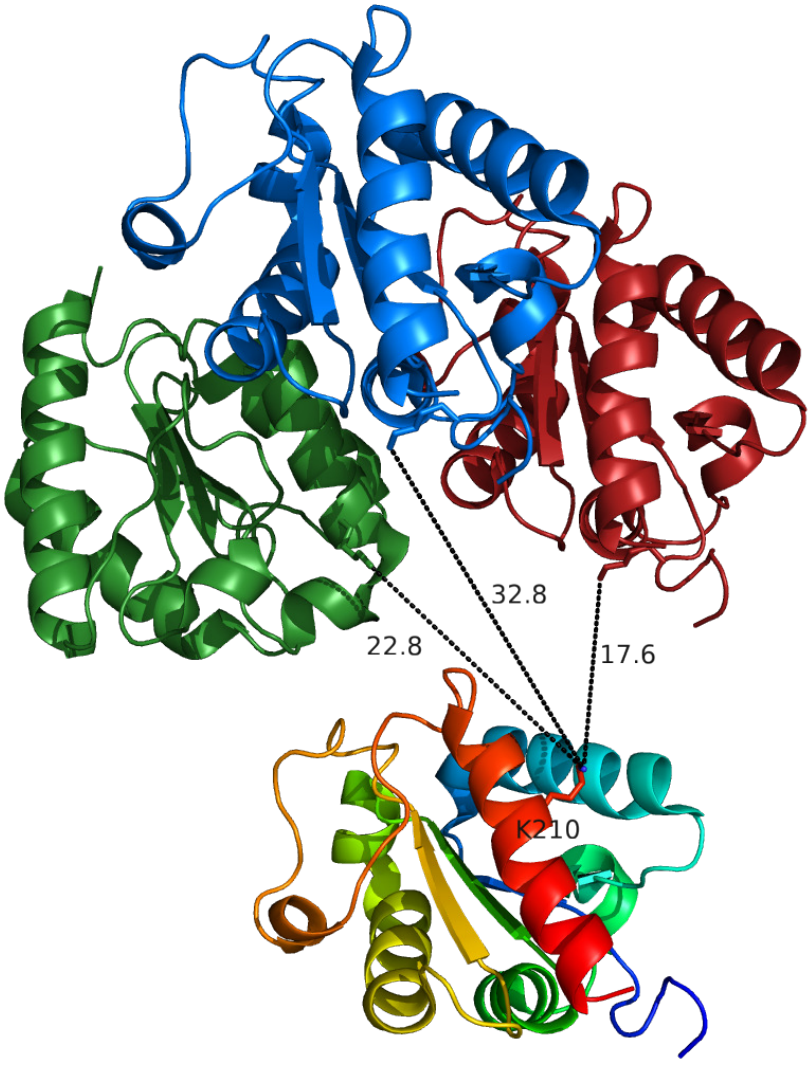

Figure 5.1: **MAL K210.** Using the MAL^{TIR} cryo-EM structure (PDB ID: 5uzb, Ve et al. 2017), K210 is inspected for potential XL-partners. The monomer holding the examined residue is colored in a rainbow spectrum while the monomers holding lysines in close proximity are in single-colors. The closest lysine is located 17.6 Å away. Figure generated with PyMOL (2020).

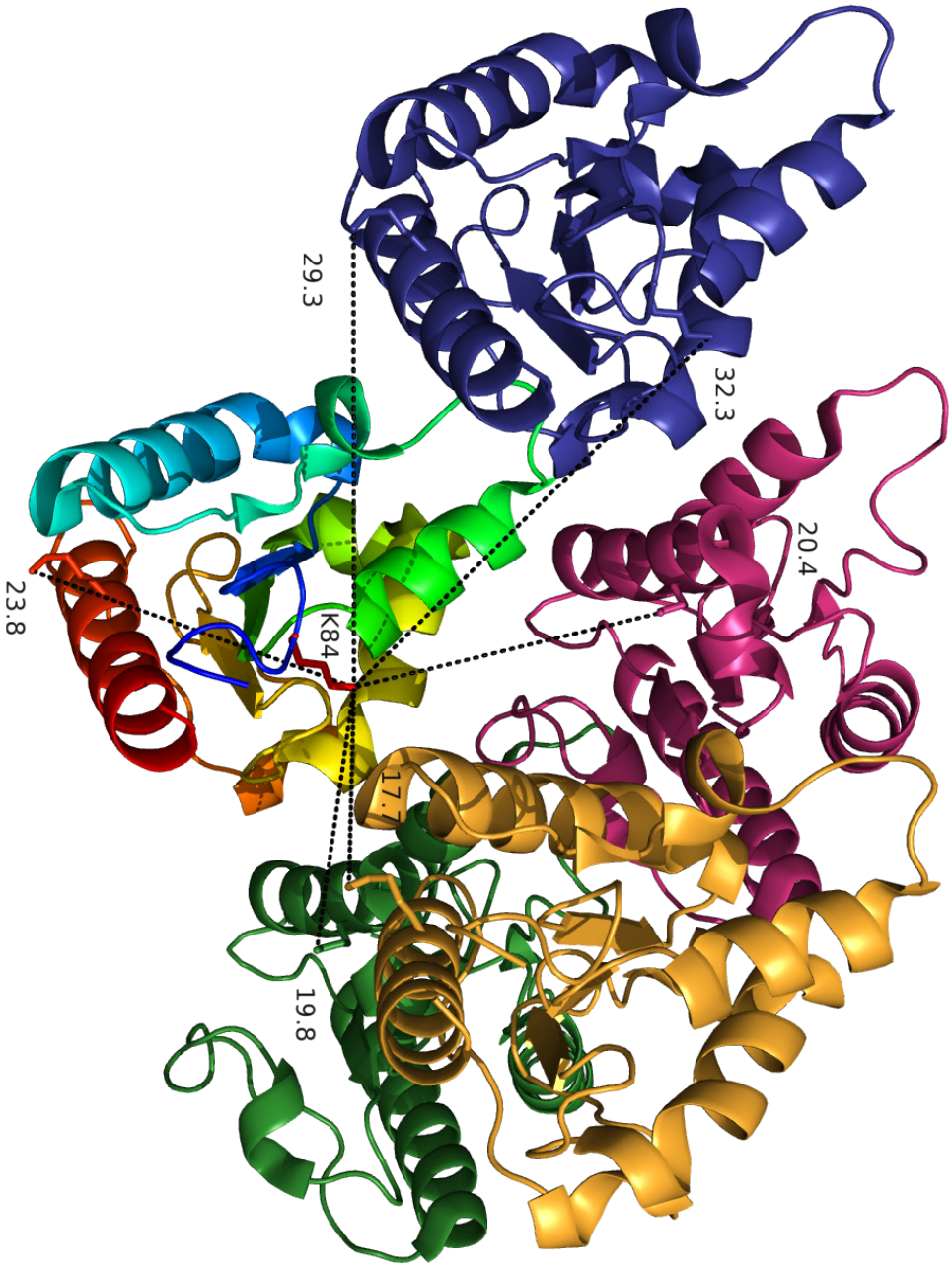

Figure 5.2: **MAL K84.** The closest intermolecular lysine to MAL K84 is located 17.7 Å away. Figure generated with PyMOL (2020) using the PDB entry 5uzb (Ve et al. 2017).

Figure 5.3: **MAL K158.** The closest lysine to MAL K158 on a neighboring subunit is located 19.8 Å away. Figure generated with PyMOL (2020) using the PDB entry 5uzb (Ve et al. 2017).

The monomers holding the examined lysines are colored in a rainbow spectrum while the monomers holding the potential cross-linking partners are single-colored. Only lysines closer than 35 Å are shown. These numbers should only give an overview of the molecular proximity of the lysines, keeping in mind that the folds of the inner- and outerstrand MAL^{TIR} monomers vary slightly.

Still, we see that the smallest distance is 17.6 Å, which is already too far apart for BS^3 to cross-link them as it has a spacer arm of only 11.4 Å. Thus, from this theoretical examination, no cross-linked product would form, which is in agreement with our XL gel data. In conclusion, by examining the cryo-EM structure of the filament forming MAL^{TIR} and its sequence, we can better understand why BS^3 is a poor choice of cross-linker for this particular purpose.

$A46^{FL}$ and MAL^{TIR}

Figure 4.8 on the right shows the results when using BS^3 to cross-link wild-type $A46^{FL}$ to MAL^{TIR}, each at 6 µM concentration. Unfortunately, no new band formation can be seen and the impurity at 46 kDa (arrow 1), which would be close to a desired cross-linked heterodimer of 48 kDa, does not increase in intensity. Still, as with the $MyD88^{TIR}$ sample with $A46^{FL}$, we used the conditions of the red box (top band) to prepare a sample for MS.

5.2.2 SDS-PAGE Results of EDC & sulfo-NHS

On changing to the second XL-systEDC and keeping the protein concentrations at 6 µM, in a first XL titration experiment, we saw a similar picture in the controls as with BS^3: In Figure 4.11, $A46^{FL}$ seems to have oligomerized, while $MyD88^{TIR}$ and MAL^{TIR} did not show any cross-linked products. Surprisingly, however, when cross-linking $A46^{FL}$ to each of the two adaptors under the same conditions, the top bands decreased at least at the lowest XL concentration (Figure 4.12). Indeed, a very faint band at the desired mass in the $MyD88^{TIR}/A46^{FL}$ sample can be hinted just below

50 kDa (arrow 5). Unfortunately, in the $A46^{FL}$ with MAL^{TIR} sample, no new band was observed.

After further optimization, we opted to incubate the samples under assembly conditions (higher protein concentrations incubated for 16 h at 30 °C) prior to cross-linking. With this method, we were able to see an effect of $A46^{FL}$ on the two adaptor protein assemblies *in vitro*, which would render cross-links under these conditions plausible. Finally, we were able to resolve cross-linked products on a gel (Figure 4.13, Azar et al. 2020, and Figure 4.14). For $MyD88^{TIR}$ cross-linked to $A46^{FL}$, two gel bands resolved sufficiently and were sent for MS-analysis. MAL^{TIR}, however, was more problematic. Although a band of the desired mass for a cross-linked product between $A46^{FL}$ and MAL^{TIR} resolved on the gel (arrow 6 in Figure 4.14), in a second attempt (preparing everything under conditions necessary for MS-analysis), the band was not reproducible. Further investigation needs to be put into this experiment, ideally, repeating it at higher protein concentrations (120 µM instead of 65 µM) to better resemble the MAL^{TIR} assembly conditions used in the negative-stain EM experiments.

5.2.3 MS-Analyses Give Insights into $MyD88^{TIR}$ Assembly Formation and Disruption Thereof by $A46^{FL}$

From both XL-MS-analyses, we gained insight into the $MyD88^{TIR}$ assembly formation *in vitro*, as observed by Ve et al. (2017). Moreover, these analyses can help us to understand why $A46^{FL}$ disrupts $MyD88^{TIR}$-assembly formation *in vitro*, as observed in our negative-stain EM experiments (Azar et al. 2020). A summary of the relevant cross-links excluding loop-links and those to tags, but including those to N-termini is given in Table 5.1. Residues involved in adaptor interaction that were also found to cross-link to $A46^{FL}$ are highlighted with a yellow background for BS^3 and with a light orange background for the EDC/sulfo-NHS XL-system, respectively, to emphasize the

significant overlap that could help us to understand MyD88^{TIR} assembly disruption.

In particular, the BS^3 sample revealed two cross-links between A46^{FL} and MyD88^{TIR}, namely K206 of A46 linked to the N-terminus of the MyD88^{TIR} construct as well as to K256. Apart from the fact that both MyD88 sites cross-linked to many other sites on MyD88^{TIR}, this supports our EM data in that A46 K206 is an important residue in the interaction interface to MyD88^{TIR}.

Analyzing the MS-data obtained from the second XL-system, we can identify many cross-link sites involved in putative MyD88^{TIR}-dimers and heterodimers of MAL^{TIR} and MyD88^{TIR}. The cross-link sites between MyD88^{TIR} and MAL^{TIR} are equaly important for *in vitro* assembly to the cross-links between MyD88^{TIR} molecules as MAL^{TIR} induces MyD88^{TIR} assembly formation *in vitro* (Ve et al. 2017). Thus, a disruption between these two adaptors by A46^{FL} would hinder nucleation of MyD88^{TIR} filament formation, while a disruption between MyD88^{TIR} molecules would hinder filament elongation. Comparing the residues on MyD88^{TIR} involved in cross-links to either of the two adaptors to those cross-linked to A46^{FL} (orange background), we

Table 5.1: Summary of the relevant cross-links for *in vitro* MAL^{TIR}-induced MyD88^{TIR} assembly formation and disruption thereof by A46^{FL}, excluding loop-links and links to tags. Residues involved in cross-links between A46^{FL} and MyD88^{TIR} that were also found to cross-link to either of the two adaptors are highlighted with a yellow background for BS^3 and with an orange background for the EDC/sulfo-NHS XL-system.
PSM=peptide spectrum match

BS^3 cross-links								PSMs
protein 1	cross-link site 1	residue	protein 2	cross-link site 2	residue	best e-value	best score	MyD88^{TIR} & A46^{FL}
MyD88^{TIR}	2	N-term	MyD88^{TIR}	2	N-term	4.152E-05	4.557E-02	1
MyD88^{TIR}	2	N-term	MyD88^{TIR}	38	K190	1.613E-12	1.463E-12	31
MyD88^{TIR}	2	N-term	MyD88^{TIR}	98	K250	3.065E-16	8.395E-06	4
MyD88^{TIR}	2	N-term	MyD88^{TIR}	104	K256	1.723E-06	1.288E-06	13
MyD88^{TIR}	2	N-term	MyD88^{TIR}	110	K262	2.193E-07	5.670E-10	4
MyD88^{TIR}	98	K250	MyD88^{TIR}	104	K256	9.021E-04	3.133E-02	1
MyD88^{TIR}	104	K256	MyD88^{TIR}	109	K261	3.110E-17	2.176E-04	9
MyD88^{TIR}	104	K256	MyD88^{TIR}	110	K262	6.908E-07	4.844E-10	2
A46^{FL}	210	K206	MyD88^{TIR}	2	N-term	8.558E-08	7.260E-05	7
A46^{FL}	210	K206	MyD88^{TIR}	104	K256	2.710E-05	5.166E-02	1

EDC & sulfo-NHS cross-links

protein 1	cross-link site 1	residue	protein 2	cross-link site 2	residue	best e-value	best score	PSMs Band 1	PSMs Band 2
MAL^{TIR}	159	D203	MyD88^{TIR}	2	N-term	6.603E-04	2.973E-02	0	1
MAL^{TIR}	167	E211	MyD88^{TIR}	2	N-term	1.327E-06	4.176E-16	0	3
MyD88^{TIR}	2	N-term	MyD88^{TIR}	7	E159	3.747E-10	1.743E-07	0	6
MyD88^{TIR}	2	N-term	MyD88^{TIR}	31	E183	1.338E-08	4.060E-14	0	4
MyD88^{TIR}	2	N-term	MyD88^{TIR}	43	D195	1.356E-10	1.331E-07	0	5
MyD88^{TIR}	2	N-term	MyD88^{TIR}	80	E232	4.125E-11	8.063E-22	0	5
MyD88^{TIR}	2	N-term	MyD88^{TIR}	82	D234	6.676E-09	2.063E-14	0	6
MyD88^{TIR}	2	N-term	MyD88^{TIR}	111	E263	2.466E-12	3.548E-20	0	33
MyD88^{TIR}	31	E183	MyD88^{TIR}	98	K250	2.916E-13	1.085E-08	0	2
MyD88^{TIR}	31	E183	MyD88^{TIR}	109	K261	2.776E-06	1.323E-09	0	2
MyD88^{TIR}	31	E183	MyD88^{TIR}	110	K262	9.643E-08	1.405E-11	0	3
MyD88^{TIR}	80	E232	MyD88^{TIR}	98	K250	1.114E-13	3.131E-08	0	2
MyD88^{TIR}	80	E232	MyD88^{TIR}	110	K262	1.052E-04	1.023E-07	0	2
MyD88^{TIR}	82	D234	MyD88^{TIR}	98	K250	1.422E-09	1.444E-06	0	1
MyD88^{TIR}	82	D234	MyD88^{TIR}	110	K262	1.696E-05	2.557E-10	0	1
MyD88^{TIR}	98	K250	MyD88^{TIR}	111	E263	4.322E-04	1.417E-04	0	1
MyD88^{TIR}	104	K256	MyD88^{TIR}	111	E263	2.054E-04	3.001E-11	0	1
MyD88^{TIR}	110	K262	MyD88^{TIR}	111	E263	8.284E-05	1.667E-08	0	1
A46^{FL}	1	N-term	MyD88^{TIR}	7	E159	4.301E-27	1.608E-03	3	0
A46^{FL}	1	N-term	MyD88^{TIR}	31	E183	3.896E-06	1.915E-03	2	0
A46^{FL}	1	N-term	MyD88^{TIR}	82	D234	2.295E-05	1.402E-02	1	0
A46^{FL}	1	N-term	MyD88^{TIR}	111	E263	1.224E-14	2.321E-04	5	0
A46^{FL}	8	D4	MyD88^{TIR}	2	N-term	1.094E-08	5.376E-02	1	0
A46^{FL}	38	D34	MyD88^{TIR}	2	N-term	1.594E-10	3.497E-03	2	0
A46^{FL}	44	E40	MyD88^{TIR}	2	N-term	2.426E-05	4.671E-01	1	0
A46^{FL}	52	D48	MyD88^{TIR}	2	N-term	1.707E-06	1.716E-03	2	0
A46^{FL}	62	D58	MyD88^{TIR}	2	N-term	1.459E-09	1.373E-02	2	0
A46^{FL}	72	E68	MyD88^{TIR}	2	N-term	9.564E-08	2.802E-03	4	0
A46^{FL}	130	D126	MyD88^{TIR}	2	N-term	2.201E-07	7.177E-05	2	0
A46^{FL}	132	D128	MyD88^{TIR}	2	N-term	2.633E-08	2.867E-04	2	0
A46^{FL}	137	E133	MyD88^{TIR}	2	N-term	1.806E-16	3.395E-07	7	0
A46^{FL}	142	D138	MyD88^{TIR}	2	N-term	2.792E-06	1.120E-02	2	0
A46^{FL}	149	D145	MyD88^{TIR}	2	N-term	1.856E-05	2.967E-03	2	0
A46^{FL}	156	D152	MyD88^{TIR}	2	N-term	9.879E-14	3.314E-08	7	0
A46^{FL}	217	E213	MyD88^{TIR}	2	N-term	3.863E-11	1.967E-04	7	0
A46^{FL}	220	E216	MyD88^{TIR}	2	N-term	1.048E-20	4.398E-03	6	0
A46^{FL}	221	D217	MyD88^{TIR}	2	N-term	2.821E-07	1.134E-05	5	0
A46^{FL}	224	D220	MyD88^{TIR}	2	N-term	1.506E-05	1.350E-03	5	0
A46^{FL}	227	E223	MyD88^{TIR}	2	N-term	3.966E-07	2.157E-03	5	0
A46^{FL}	228	D224	MyD88^{TIR}	2	N-term	4.566E-07	2.038E-04	7	0
A46^{FL}	229	D225	MyD88^{TIR}	2	N-term	7.915E-08	3.299E-04	6	0
A46^{FL}	230	D226	MyD88^{TIR}	2	N-term	1.490E-10	8.454E-06	9	0
A46^{FL}	239	D235	MyD88^{TIR}	2	N-term	7.834E-10	2.425E-03	5	0
A46^{FL}	241	E237	MyD88^{TIR}	2	N-term	4.473E-06	1.698E-08	8	2
A46^{FL}	243	D239	MyD88^{TIR}	2	N-term	4.482E-12	6.500E-05	12	0
A46^{FL}	137	E133	MyD88^{TIR}	109	K261	4.451E-04	1.057E-02	1	0
A46^{FL}	156	D152	MyD88^{TIR}	109	K261	9.019E-07	6.079E-03	1	0
A46^{FL}	156	D152	MyD88^{TIR}	110	K262	1.063E-10	1.727E-03	1	0
A46^{FL}	210	K206	MyD88^{TIR}	80	E232	6.239E-08	6.576E-03	1	0
A46^{FL}	210	K206	MyD88^{TIR}	82	D234	3.214E-07	2.873E-03	1	0
A46^{FL}	217	E213	MyD88^{TIR}	98	K250	9.450E-08	1.484E-01	1	0
A46^{FL}	239	D235	MyD88^{TIR}	106	K258	6.964E-04	8.338E-03	1	0
A46^{FL}	239	D235	MyD88^{TIR}	110	K262	9.754E-16	1.931E-01	1	0
A46^{FL}	241	E237	MyD88^{TIR}	38	K190	8.588E-04	3.432E-03	1	0
A46^{FL}	241	E237	MyD88^{TIR}	106	K258	2.307E-04	3.107E-03	1	0

again find a significant overlap, which helps to explain filament disruption *in vitro*. In addition, K206 of A46 cross-linked in this system as well, emphasizing its importance.

Taken together, these data support our negative-stain EM observations in that wild-type $A46^{FL}$ disrupted MAL^{TIR}-induced $MyD88^{TIR}$ assembly formation *in vitro*. In particular, XL confirms K206 of A46 to be a crucial residue for interaction to $MyD88^{TIR}$ (Azar et al. 2020).

5.2.4 Physiologically Relevant Interaction Sites

For the analysis of physiological relevant sites, we must omit cross-links to N-termini because they may be artificial from the protein constructs. Recall that full-length MyD88 has an N-terminal death domain, which is absent from the recombinant protein construct (Figure 3.2) and the purified, cleaved construct of $A46^{FL}$ holds four extra amino acids N-terminally (Figure 3.1). Table 5.2, therefore, summarizes the cross-links of physiological relevance. In addition, the location of each residue within the secondary structure is stated to better visualize regions of interactions (Azar et al. 2020), which will be discussed in more detail later to find possible modes of interaction between $A46^{FL}$ and $MyD88^{TIR}$.

In short, this table, again, visualizes the overlap of cross-linked residues as denoted with the colored background: $A46^{FL}$ targets residues on $MyD88^{TIR}$ that seem to be important for $MyD88^{TIR}$ oligomerization. In the BS^3 experiment A46 K206 cross-linked to K256 on $MyD88^{TIR}$, which is involved in all three cross-links within the $MyD88^{TIR}$ sequence. A similar picture was obtain in the second XL-experiment using EDC and sulfo-NHS where $A46^{FL}$ cross-linked to five individual residues on $MyD88^{TIR}$ that also engaged in cross-links to $MyD88^{TIR}$. To note, the results of these two XL-system cannot be compared one-by-one as they link different chemical groups and introduce different spacer arm lengths.

Table 5.2: Summary of the physiologically relevant cross-links with the location of the residues in the respective secondary structure stated (Azar et al. 2020). Residues involved in MyD88^{TIR} interaction that were also found to cross-link to A46^{FL} are highlighted, with a green background for the BS^3 sample and a violet background for the EDC/sulfo-NHS links.
PSM: peptide spectrum match, CTFR: C-terminal flexible region

BS^3 cross-links

protein 1	cross-link site 1	residue	location	protein 2	cross-link site 2	residue	location	best e-value	best score	PSMs MyD88^{TIR} & A46^{FL}
MyD88^{TIR}	98	K250	CD loop	MyD88^{TIR}	104	K256	βD	9.021E-04	3.133E-02	1
MyD88^{TIR}	104	K256	βD	MyD88^{TIR}	109	K261	DE loop	3.110E-17	2.176E-04	9
MyD88^{TIR}	104	K256	βD	MyD88^{TIR}	110	K262	DE loop	6.908E-07	4.844E-10	2
A46^{FL}	210	K206	α7	MyD88^{TIR}	104	K256	βD	2.710E-05	5.166E-02	1

EDC & sulfo-NHS cross-links

protein 1	cross-link site 1	residue	location	protein 2	cross-link site 2	residue	location	best e-value	best score	PSMs Band 1	PSMs Band 2
MyD88^{TIR}	31	E183	αA	MyD88^{TIR}	98	K250	CD loop	2.916E-13	1.085E-08	0	2
MyD88^{TIR}	31	E183	αA	MyD88^{TIR}	109	K261	DE loop	2.776E-06	1.323E-09	0	2
MyD88^{TIR}	31	E183	αA	MyD88^{TIR}	110	K262	DE loop	9.643E-08	1.405E-11	0	3
MyD88^{TIR}	80	E232	αC	MyD88^{TIR}	98	K250	CD loop	1.114E-13	3.131E-08	0	2
MyD88^{TIR}	80	E232	αC	MyD88^{TIR}	110	K262	DE loop	1.052E-04	1.023E-07	0	2
MyD88^{TIR}	82	D234	αC	MyD88^{TIR}	98	K250	CD loop	1.422E-09	1.444E-06	0	1
MyD88^{TIR}	82	D234	αC	MyD88^{TIR}	110	K262	DE loop	1.696E-05	2.557E-10	0	1
MyD88^{TIR}	98	K250	CD loop	MyD88^{TIR}	111	E263	DE loop	4.322E-04	1.417E-04	0	1
MyD88^{TIR}	104	K256	βD	MyD88^{TIR}	111	E263	DE loop	2.054E-04	3.001E-11	0	1
MyD88^{TIR}	110	K262	DE loop	MyD88^{TIR}	111	E263	DE loop	8.284E-05	1.667E-08	0	1
A46^{FL}	137	E133	α3	MyD88^{TIR}	109	K261	DE loop	4.451E-04	1.057E-02	1	0
A46^{FL}	156	D152	α4	MyD88^{TIR}	109	K261	DE loop	9.019E-07	6.079E-03	1	0
A46^{FL}	156	D152	α4	MyD88^{TIR}	110	K262	DE loop	1.063E-10	1.727E-03	1	0
A46^{FL}	210	K206	α7	MyD88^{TIR}	80	E232	αC	6.239E-08	6.576E-03	1	0
A46^{FL}	210	K206	α7	MyD88^{TIR}	82	D234	αC	3.214E-07	2.873E-03	1	0
A46^{FL}	217	E213	CTFR	MyD88^{TIR}	98	K250	CD loop	9.450E-08	1.484E-01	1	0
A46^{FL}	239	D235	CTFR (?)	MyD88^{TIR}	106	K258	DE loop	6.964E-04	8.338E-03	1	0
A46^{FL}	239	D235	CTFR (?)	MyD88^{TIR}	110	K262	DE loop	9.754E-16	1.931E-01	1	0
A46^{FL}	241	E237	CTFR (?)	MyD88^{TIR}	38	K190	AB loop	8.588E-04	3.432E-03	1	0
A46^{FL}	241	E237	CTFR (?)	MyD88^{TIR}	106	K258	DE loop	2.307E-04	3.107E-03	1	0

Cross-links on MyD88^{TIR}

Focusing on the interaction interfaces on MyD88^{TIR}, we used the NMR-structure (PDB ID: 2z5v, Ohnishi et al. 2009) to visualize the cross-linked residues. Physiological relevant cross-link sites as stated in Table 5.2 are shown in Figure 5.4 A as sticks with their respective cross-link partners stated, and in the surface representation in B colored in black for better visualization (Azar et al. 2020).

By stating the cross-linked partners in Figure A, we can see that an individual residue on MyD88^{TIR} that engaged in many interactions within a presumable MyD88^{TIR} homodimer was targeted by only one or two A46 residues. Thus, this

visualization helps to explain the destructive effects of A46 on MAL^{TIR}-induced MyD88^{TIR} assembly formation *in vitro*. As seen in Figure B, all residues on MyD88^{TIR} are surface-exposed, which is not surprising given the properties of their side chains and availability for cross-linking.

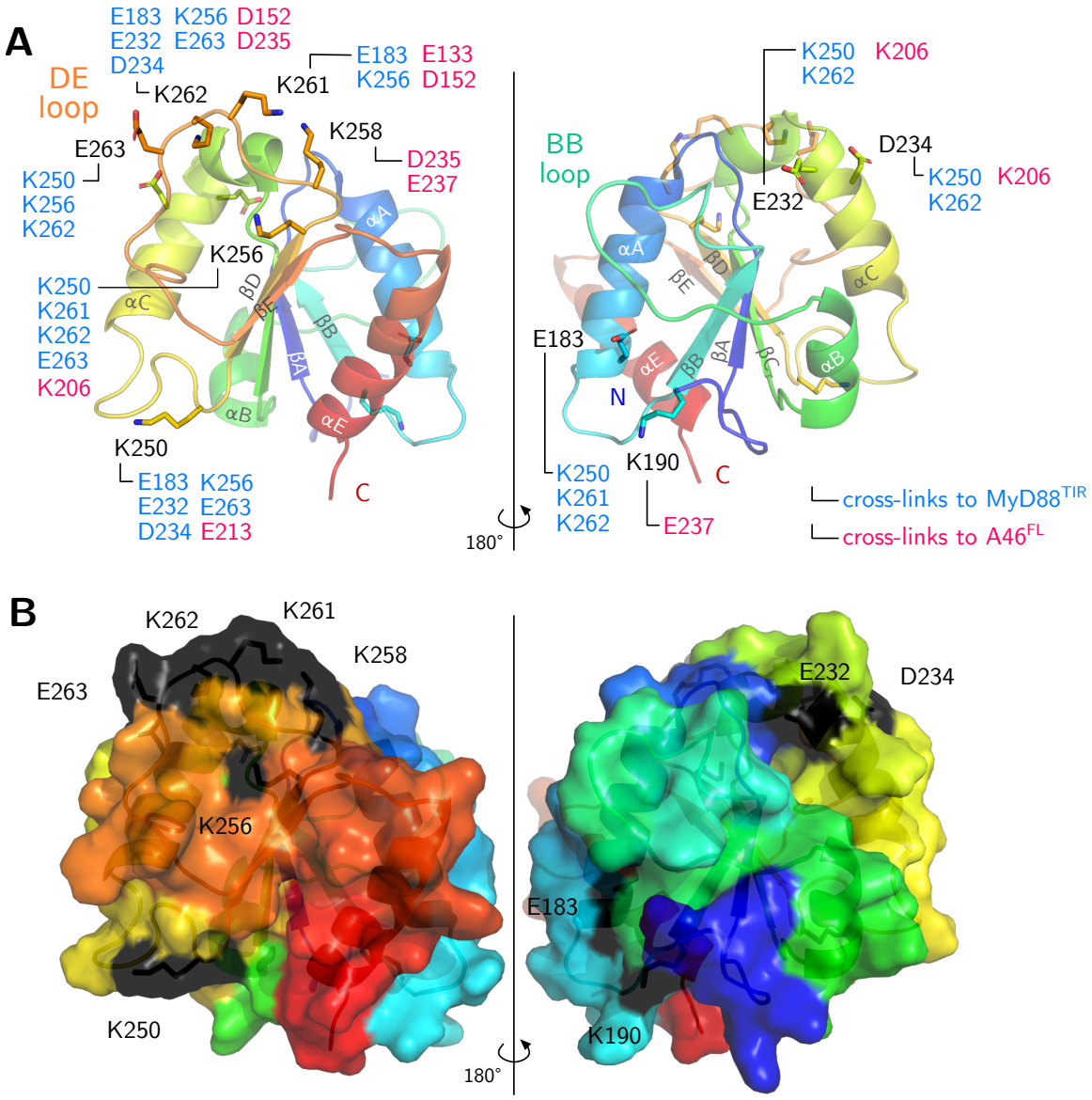

Figure 5.4: **Physiologically relevant cross-link sites visualized on MyD88^{TIR}.**
(A) Cartoon representation colored in a rainbow-spectrum and rotated by 180° with the cross-linked residues represented as sticks. The cross-link site to MyD88^{TIR} and A46^{FL} are stated.
(B) Surface representations with the cross-linked residues in black.
Figures generated with PyMOL (2020) usind the PDB entry 2z5v (Ohnishi et al. 2009) and labeled with Inkscape (2020).

Emphasizing the cross-links to A46^{FL}, we find a cluster in the DE-loop with three well-exposed residues (K258, K261, and K262) and one in close proximity but slightly buried in a notch (K256). Another region involves two residues in the αC-helix, namely E232 and D234. Considering the adjacent BB-loop as another reported interaction site to A46 (Stack and Bowie 2012), these three areas could contribute to the same binding interface. Conformationally distant from the above mentioned area are another two residues (K190 and K250) that cross-linked to A46^{FL}.

To better understand how A46 inhibits NFκB signaling on the MyD88 level, the sequence introduced in the first chapter is expanded with our XL data (Figure 5.5). Blue dots symbol cross-link sites to MyD88^{TIR} while pink squares show those to

Figure 5.5: **MyD88^{TIR} sequence.** The cross-link sites from Table 5.2 are summarized in the sequence introduced in the first chapter with blue spots for links within MyD88^{TIR} and as pink squares those to A46^{FL} as pink squares.
Sequence obtained from the PDB entry 2z5v (Berman 2000; Ohnishi et al. 2009); figure generated with Inkscape (2020).

$A46^{FL}$.

Before investigating links to A46, there is one cross-link to $MyD88^{TIR}$ that did not cross-link to A46 or have neighboring residues that did, namely E183. E183 was reported to be essential for MyD88 dimerization *in vitro* and signaling *in cells* (Loiarro et al. 2013). Our data confirms this as E183 cross-linked within the $MyD88^{TIR}$ sequence.

Focusing on cross-links to A46, most links are between the residues 232 to 263 of MyD88. This sequence does not hold a conserved TIR-sequence (Ve et al. 2015) but two reports proposed binding sites for this stretch. First, Vyncke et al. (2016) noted binding site II (blue squares) to be important for interaction with MAL and for NFκB activation. Our XL-data show that A46 targets two residues within or close to this proposed binding site (E232 and D234, respectively), thereby enhancing our understanding how A46 inhibits MyD88 nucleation at the MAL^{TIR}-$MyD88^{TIR}$ interface. Second, the $MyD88^{TIR}$ protofilament model by Ve et al. (2017) predicted parts of the CD and EE surface to fall into this cross-linked-rich sequence. The majority of the cross-links between $A46^{FL}$ and $MyD88^{TIR}$ are at or in close proximity to these two proposed filament interfaces, which would lead the to conclusion that A46 targets the intra- and interstrand interface of the protofilament. Recently, the $MyD88^{TIR}$ assembly structure was resolved and the interfaces within and between the $MyD88^{TIR}$ protofilaments clarified (by personal communication with Bostjan Kobe). Our XL data illustrate that A46 targets the interface between two protofilaments in addition to the interfaces within the protofilament, thereby more efficiently inhibiting $MyD88^{TIR}$ oligomerization.

The BB loop was shown to be essential for homotypic $MyD88^{TIR}$ interaction (Gay et al. 2014; Ve et al. 2015) and targeted by A46 (Stack and Bowie 2012). Nevertheless, our XL-data did not record any links in this region, either to $MyD88^{TIR}$ or to $A46^{FL}$. Judging from the given sequence of $MyD88^{TIR}$, there are not many sites amenable for

cross-linking with the employed XL-systems; it is, thus, not surprising that no links were recorded. More importantly, no evidence against the importance of the BB loop was obtained.

Interaction Sites on A46^{CTD}

The first XL-experiment with BS^3 already gave a strong indication that A46 K206 is indeed a vital interaction partner, while the second XL-system confirmed K206 and revealed five more sites, namely E133, D152, E213, D235, and E237. All six residues are located in the CTD of A46, depicted in the dimeric structure in Figure 5.6 with the last two residues not resolved but drawn schematically (PDB ID: 4lqk, Fedosyuk et al. 2014).

In particular, E133 is located in helix α3, which has not yet been reported to have a particular function, while residue D152 is located in helix α4, parts of which are involved in the dimer interface together with helix α6 (gray residues, Fedosyuk et al. 2014) but D152 does not participate in dimer formation. These two residues (E133 and D152) cross-linked to the same region on MyD88^{TIR}, namely K261 and K262. By orientating E133 and D152 on the A46 monomer, they face they same plane and could thus, contribute to the same site of interaction. Moreover, D152 of the adjacent molecule in the A46^{CTD} dimer falls into the same plane as E133 and D152 of the one molecule and could thus be part of the same interaction site.

Next, there are four residues towards the C-terminus: K206 in α7-helix, E213, D235, and E237 in the C-terminal flexible region (CTFR). Here, we find K206 and E237 each linking to two conformationally distant areas on MyD88^{TIR}. Therefore, there must be more than one specific way of interaction between A46 and MyD88. Assuming the CTFR can freely wrap around the molecule, there are two feasible options for the reported cross-links. In the first scenario, K206 of A46 interacted with K256 of MyD88, which could be followed by E213 linked to K250, and the flexible tail with E237 wrapping around to link to K190 explaining the distant interaction

site on MyD88^{TIR} as stated before. However, in this scenario the cross-link between the CTFR (D235 and E237) and K258 on MyD88 seems unlikely and must therefore be accounted for in the second scenario, which would explain K206 cross-linked to the area E232/D234 on MyD88 on the opposite side of the reported link to K256, now allowing the CTFR to now engage with K258 on MyD88, or alternatively again with K190. Moreover, in the dimeric form the two C-terminal ends are located on the far opposite sides allowing for interaction with two different molecules and giving the CTFR unconfined possibilities. This supports the idea of at least two different modes of interaction between A46 and MyD88, and the flexible tail freely wrapping around.

Keeping in mind the theory of SCAF (Vajjhala et al. 2017) and the observation of MyD88 oligomerization (Ve et al. 2017), an A46 dimer could capture two MyD88 monomers or inhibit a MyD88 dimer from assembling. Thus, A46 efficiently inhibits filament elongation necessary for signal transduction. Moreover, the VIPER-peptide (corresponding to parts of the sequence in helix α1 of A46) did not interact with

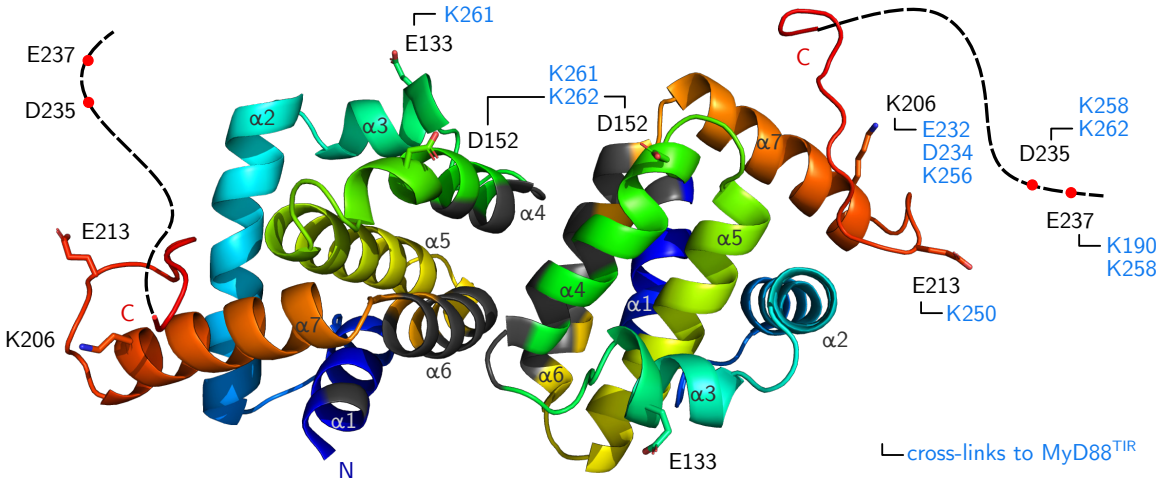

Figure 5.6: **A46 dimer.** Residues involved in the dimer interface are colored in gray while cross-linked residues to MyD88^{TIR} are visualized as sticks and labeled. D235 and E237 are not resolved in the structure and only schematically added. Figure generated with PyMOL (2020) using the PDB entry 4lqk (Berman 2000; Fedosyuk et al. 2014) and labeled with Inkscape (2020).

MyD88^{TIR} but MAL^{TIR} (Lysakova-Devine et al. 2010), which is in agreement to our XL-data. With this information, the CTD of A46 could on the one side interact with MAL^{TIR} via its α1 helix while at the same time bind MyD88^{TIR} on the adjacent site via the E133/D152 plane and/or K206 together with the CTFR. Or, considering the tetrameric structure of A46, where the two CTD dimers are orientated away from each other (Fedosyuk et al. 2016), one CTD dimer could interact with MAL while the other interacts with MyD88. Either way, A46 would prevent nucleation of MyD88 assembly in the signaling cascade.

In Figure 5.7 the cross-links to MyD88^{TIR} are added to the CTD sequence introduced in the first chapter. Here, we see that the recorded links to MyD88^{TIR} do not overlap with the residues reported to be involved in A46 dimerization (Fedosyuk et al. 2014; Y. Kim et al. 2014). Additionally, the VIPER peptide was reported to inhibit MAL but not MyD88 (Lysakova-Devine et al. 2010), which is supported by our data with no recorded links to MyD88^{TIR} in the VIPER region. Previously, the ClusPro algorithm predicted a model of A46 docked to MyD88^{TIR} (light green dots, Fedosyuk 2014), which unfortunately cannot be supported with our XL data.

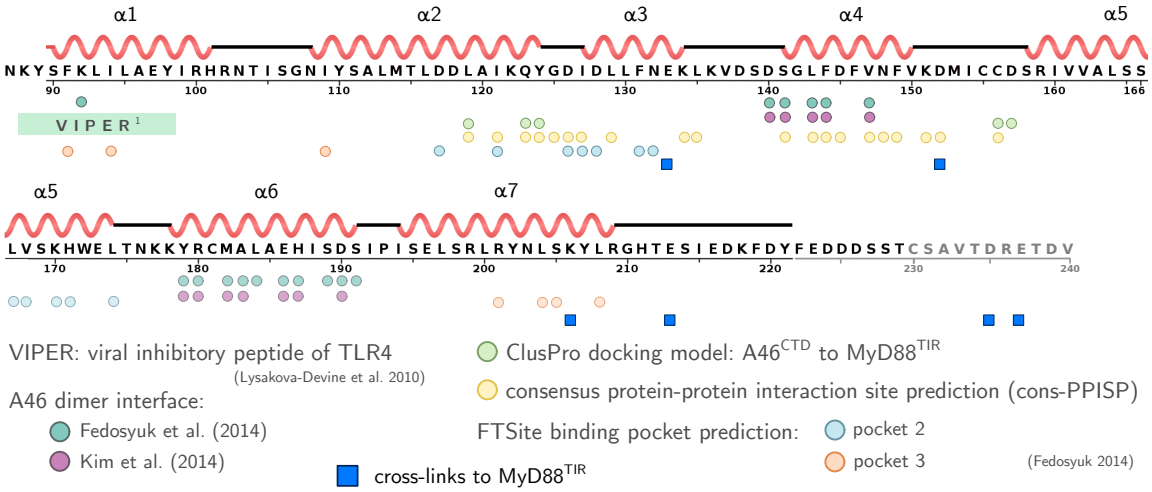

Figure 5.7: **A46^{CTD} sequence.** Cross-links to MyD88^{TIR} are added to the sequence introduced in the first chapter. Sequence obtained from the PDB entry 4lqk (Berman 2000; Fedosyuk et al. 2014); figure and the missing C-terminal sequence generated with Inkscape (2020).

In addition, the FTSite binding pocket prediction algorithm previously revealed two areas worth investigating (Fedosyuk 2014): pocket 2 (blue dots) is supported with one cross-link (E133) adjacent to the predicted site and pocket 3 (orange dots) with another link (K206) in close proximity.

5.3 Conclusion

To investigate the interaction of the CTD of A46 with the TIR-domain of MyD88, we chose four surface-exposed amino acids within the last helix α7 of A46 and abolished their interaction by substituting them for alanines (Mutant 1: A46 R199A Y202A; Mutant 2: A46 K206A R209A). Site-directed mutagenesis successfully introduced the desired mutations and purification of the two mutants was successful. Negative-stain EM gave us a first indication that K206 and/or R209 might be involved in the interaction interface to $MyD88^{TIR}$.

Cross-linking wild-type A46 to $MyD88^{TIR}$ confirmed K206 to be a vital residue for inhibiting $MyD88^{TIR}$ assembly formation and revealed further residues on both molecules. After investigation of the published structures, the dimeric $A46^{CTD}$ seems to interact with $MyD88^{TIR}$ in more than one specific way, allowing the interaction of more than one adaptor molecule simultaneously. Moreover, the cross-linking analysis indicated that A46 targets the inter- and intrastrand interface within the $MyD88^{TIR}$ protofilament as well as the interface between protofilaments.

In conclusion, these studies give first insights into the interaction sites between A46 and MyD88 and help to understand how A46 efficiently hinders MyD88 assembly formation and thereby inhibits NFκB activation.

6
References

Abbas, A. K., Lichtman, A. H., & Pillai, S. (2010). *Cellular and Molecular Immunology: Updated Edition* (6th ed.). ISBN: 978-1-4160-3123-9. Saunders Elsevier.

Albarnaz, J., Torres, A., & Smith, G. (2018). Modulating vaccinia virus immunomodulators to improve immunological memory. *Viruses*, *10*(3), 101. PMID: 29495547. doi:10.3390/v10030101

Arthur, J. S. C., & Ley, S. C. (2013). Mitogen-activated protein kinases in innate immunity. *Nature Reviews Immunology*, *13*(9), 679–692. PMID: 23954936. doi:10.1038/nri3495

Azar, D. F., Haas, M., Fedosyuk, S., Rahaman, M. H., Hedger, A., Kobe, B., & Skern, T. (2020). Vaccinia Virus Immunomodulator A46: Destructive Interactions with MAL and MyD88 Shown by Negative-Stain EM. *SSRN Electronic Journal*. preprint - under review. doi:10.2139/ssrn.3600564

Balka, K. R., & Nardo, D. (2018). Understanding early TLR signaling through the Myddosome. *Journal of Leukocyte Biology*, *105*(2), 339–351. PMID: 30256449. doi:10.1002/jlb.mr0318-096r

Berman, H. M. (2000). The Protein Data Bank. *Nucleic Acids Research*, *28*(1), 235–242. doi:10.1093/nar/28.1.235

Bonham, K. S., Orzalli, M. H., Hayashi, K., Wolf, A. I., Glanemann, C., Weninger, W., Iwasaki, A., Knipe, D. M., & Kagan, J. C. (2014). A Promiscuous Lipid-Binding Protein Diversifies the Subcellular Sites of Toll-like Receptor Signal Transduction. *Cell*, *156*(4), 705–716. PMID: 24529375. doi:10.1016/j.cell.2014.01.019

Bowie, A. G., Kiss-Toth, E., Symons, J. A., Smith, G. L., Dower, S. K., & O'Neill, L. A. J. (2000). A46R and A52R from vaccinia virus are antagonists of host IL-1 and toll-like receptor signaling. *Proceedings of the National Academy of Sciences*, *97*(18), 10162–10167. PMID: 10920188. doi:10.1073/pnas.160027697

Bowie, A. G., & Unterholzner, L. (2008). Viral evasion and subversion of pattern-recognition receptor signalling. *Nature Reviews Immunology*, *8*(12), 911–922. PMID: 18989317. doi:10.1038/nri2436

Broyles, S. S. (2003). Vaccinia virus transcription. *Journal of General Virology*, *84*(9), 2293–2303. PMID: 12917449. doi:10.1099/vir.0.18942-0

Carter, G. C., Rodger, G., Murphy, B. J., Law, M., Krauss, O., Hollinshead, M., & Smith, G. L. (2003). Vaccinia virus cores are transported on microtubules. *The Journal of general virology*, *84*, 2443–2458. PMID: 12917466. doi:10.1099/vir.0.19271-0

Chen, Z. J. (2005). Ubiquitin signalling in the NF-κB pathway. *Nature Cell Biology*, *7*(8), 758–765. PMID: 16056267. doi:10.1038/ncb0805-758

Chiuppesi, F., d'Alincourt Salazar, M., Contreras, H., Nguyen, V., Martinez, J., Park, S., Nguyen, J., Kha, M., Iniguez, A., Zhou, Q., Kaltcheva, T., Levytskyy, R., Ebelt, N., Kang, T., Wu, X., Rogers, T., Manuel, E., Shostak, Y., Diamond, D., & Wussow, F. (2020). Development of a Multi-Antigenic SARS-CoV-2 Vaccine Using a Synthetic Poxvirus Platform. *Research Square*. preprint - under review. doi:10.21203/rs.3.rs-40198/v1

Combe, C. W., Fischer, L., & Rappsilber, J. (2015). xiNET: Cross-link network maps with residue resolution. *Molecular & Cellular Proteomics*, *14*(4), 1137–1147. PMID: 25648531. doi:10.1074/mcp.o114.042259

Condit, R. C., Moussatche, N., & Traktman, P. (2006). In a nutshell: Structure and assembly of the vaccinia virion. In *Advances in virus research* (pp. 31–124). PMID: 16877059. doi:10.1016/s0065-3527(06)66002-8

Cyrklaff, M., Risco, C., Fernandez, J. J., Jimenez, M. V., Esteban, M., Baumeister, W., & Carrascosa, J. L. (2005). Cryo-electron tomography of vaccinia virus. *Proceedings of the National Academy of Sciences*, *102*(8), 2772–2777. PMID: 15699328. doi:10.1073/pnas.0409825102

Dunne, A., Ejdebäck, M., Ludidi, P. L., O'Neill, L. A. J., & Gay, N. J. (2003). Structural Complementarity of Toll/Interleukin-1 Receptor Domains in Toll-like Receptors and the Adaptors Mal and MyD88. *Journal of Biological Chemistry*, *278*(42), 41443–41451. PMID: 12888566. doi:10.1074/jbc.m301742200

Esparza, J., Schrick, L., Damaso, C. R., & Nitsche, A. (2017). Equination (inoculation of horsepox): An early alternative to vaccination (inoculation of cowpox) and the potential role of horsepox virus in the origin of the smallpox vaccine. *Vaccine*, *35*(52), 7222–7230. PMID: 29137821. doi:10.1016/j.vaccine.2017.11.003

Fedosyuk, S. (2014). Structural studies of VACV A46 and TBEV NS2B/3 proteins as an approach to elucidate virus-host interactions. Doctoral dissertation, Medizinische Universität Wien.

Fedosyuk, S., Bezerra, G. A., Radakovics, K., Smith, T. K., Sammito, M., Bobik, N., Round, A., Eyck, L. F. T., Djinović-Carugo, K., Usón, I., & Skern, T. (2016). Vaccinia Virus Immunomodulator A46: A Lipid and Protein-Binding Scaffold

for Sequestering Host TIR-Domain Proteins. *PLOS Pathogens*, *12*(12). PMID: 27973613. doi:10.1371/journal.ppat.1006079

Fedosyuk, S., Grishkovskaya, I., de Almeida Ribeiro, E., & Skern, T. (2014). Characterization and Structure of the Vaccinia Virus NF-κB Antagonist A46. *Journal of Biological Chemistry*, *289*(6), 3749–3762. PMID: 24356965. doi:10.1074/jbc.m113.512756

Gay, N. J., Symmons, M. F., Gangloff, M., & Bryant, C. E. (2014). Assembly and localization of Toll-like receptor signalling complexes. *Nature Reviews Immunology*, *14*(8), 546–558. PMID: 25060580. doi:10.1038/nri3713

George, J., Motshwene, P. G., Wang, H., Kubarenko, A. V., Rautanen, A., Mills, T. C., Hill, A. V. S., Gay, N. J., & Weber, A. N. R. (2011). Two human myd88 variants, s34y and r98c, interfere with myd88-irak4-myddosome assembly. *The Journal of biological chemistry*, *286*, 1341–1353. PMID: 20966070. doi:10.1074/jbc.M110.159996

Ghosh, S., & Dass, J. F. P. (2016). Study of pathway cross-talk interactions with NF-κB leading to its activation via ubiquitination or phosphorylation: A brief review. *Gene*, *584*(1), 97–109. PMID: 26968890. doi:10.1016/j.gene.2016.03.008

GIMP. (2020). GNU Image Manipulation Program (Version 2.10.18).

Henderson, D. A. (2011). The eradication of smallpox – an overview of the past, present, and future. *Vaccine*, *29 Suppl 4*, D7–D9. PMID: 22188929. doi:10.1016/j.vaccine.2011.06.080

Inkscape. (2020). Inkscape Project (Version 1.0).

Jacobs, B. L., Langland, J. O., Kibler, K. V., Denzler, K. L., White, S. D., Holechek, S. A., Wong, S., Huynh, T., & Baskin, C. R. (2009). Vaccinia virus vaccines: Past, present and future. *Antiviral Research*, *84*(1), 1–13. PMID: 19563829. doi:10.1016/j.antiviral.2009.06.006

Jiang, Z., Georgel, P., Li, C., Choe, J., Crozat, K., Rutschmann, S., Du, X., Bigby, T., Mudd, S., Sovath, S., Wilson, I. A., Olson, A., & Beutler, B. (2006). Details of toll-like receptor:adapter interaction revealed by germ-line mutagenesis. *Proceedings of the National Academy of Sciences*, *103*(29), 10961–10966. PMID: 16832055. doi:10.1073/pnas.0603804103

Kawai, T., & Akira, S. (2010). The role of pattern-recognition receptors in innate immunity: update on Toll-like receptors. *Nature Immunology*, *11*(5), 373–384. PMID: 20404851. doi:10.1038/ni.1863

Kim, Y., Lee, H., Heo, L., Seok, C., & Choe, J. (2014). Structure of vaccinia virus A46, an inhibitor of TLR4 signaling pathway, shows the conformation of VIPER motif. *Protein Science*, *23*(7), 906–914. PMID: 24723367. doi:10.1002/pro.2472

Kim, Y.-C., Lee, S. E., Kim, S. K., Jang, H.-D., Hwang, I., Jin, S., Hong, E.-B., Jang, K.-S., & Kim, H.-S. (2019). Toll-like receptor mediated inflammation requires FASN-dependent MYD88 palmitoylation. *Nature Chemical Biology*, *15*(9), 907–916. PMID: 31427815. doi:10.1038/s41589-019-0344-0

Lane, J. M., & Poland, G. A. (2011). Why not destroy the remaining smallpox virus stocks? *Vaccine*, *29*(16), 2823–2824. PMID: 21376120. doi:10.1016/j.vaccine.2011.02.081

Law, M., Carter, G. C., Roberts, K. L., Hollinshead, M., & Smith, G. L. (2006). Ligand-induced and nonfusogenic dissolution of a viral membrane. *Proceedings of the National Academy of Sciences of the United States of America*, *103*, 5989–5994. PMID: 16585508. doi:10.1073/pnas.0601025103

LibreOffice. (2020). The Documentation Foundation (Version 6.4.4).

Liu, L., Cooper, T., Howley, P., & Hayball, J. (2014). From crescent to mature virion: Vaccinia virus assembly and maturation. *Viruses*, *6*(10), 3787–3808. PMID: 25296112. doi:10.3390/v6103787

Loiarro, M., Volpe, E., Ruggiero, V., Gallo, G., Furlan, R., Maiorino, C., Battistini, L., & Sette, C. (2013). Mutational Analysis Identifies Residues Crucial for Homodimerization of Myeloid Differentiation Factor 88 (MyD88) and for Its Function in Immune Cells. *Journal of Biological Chemistry*, *288*(42), 30210–30222. PMID: 24019529. doi:10.1074/jbc.m113.490946

Luo, L., Lucas, R. M., Liu, L., & Stow, J. L. (2019). Signalling, sorting and scaffolding adaptors for Toll-like receptors. *Journal of Cell Science*, *133*. PMID: 31889021. doi:10.1242/jcs.239194

Lysakova-Devine, T., Keogh, B., Harrington, B., Nagpal, K., Halle, A., Golenbock, D. T., Monie, T., & Bowie, A. G. (2010). Viral Inhibitory Peptide of TLR4, a Peptide Derived from Vaccinia Protein A46, Specifically Inhibits TLR4 by Directly Targeting MyD88 Adaptor-Like and TRIF-Related Adaptor Molecule. *The Journal of Immunology*, *185*(7), 4261–4271. PMID: 20802145. doi:10.4049/jimmunol.1002013

Mahy, B. W. J. (2003). An overview on the use of a viral pathogen as a bioterrorism agent: Why smallpox? *Antiviral Research*, *57*(1-2), 1–5. PMID: 12615297. doi:10.1016/s0166-3542(02)00194-8

Max Perutz Labs Mass Spectrometry Service Facility. (2018). *Sample preparation guidelines for MS-base cross-linking (XL-MS)*. Version Dec 2018.

Mohamed, M. R., & McFadden, G. (2009). NFκB inhibitors: Strategies from poxviruses. *Cell Cycle*, *8*(19), 3125–3132. PMID: 19738427. doi:10.4161/cc.8.19.9683

Moss, B. (1990). Regulation of vaccinia virus transcription. *Annual Review of Biochemistry*, *59*(1), 661–688. PMID: 2197987. doi:10.1146/annurev.bi.59.070190.003305

Moss, B. (2013). Poxvirus DNA replication. *Cold Spring Harbor Perspectives in Biology*, *5*(9), a010199–a010199. PMID: 23838441. doi:10.1101/cshperspect.a010199

Moss, B. (2016). Membrane fusion during poxvirus entry. *Seminars in Cell & Developmental Biology*, *60*, 89–96. PMID: 27423915. doi:10.1016/j.semcdb.2016.07.015

Nanson, J. D., Rahaman, M. H., Ve, T., & Kobe, B. (2020). Regulation of signaling by cooperative assembly formation in mammalian innate immunity signalosomes by molecular mimics. *Seminars in Cell & Developmental Biology*, *99*, 96–114. PMID: 29738879. doi:10.1016/j.semcdb.2018.05.002

Narayanan, K. B., & Park, H. H. (2015). Toll/interleukin-1 receptor (TIR) domain-mediated cellular signaling pathways. *Apoptosis*, *20*(2), 196–209. PMID: 25563856. doi:10.1007/s10495-014-1073-1

New England BioLabs® Inc. (2019). *Q5® Site-Directed Mutagenesis Kit (Without Competent Cells*. Version 1.0. Retrieved from https://international.neb.com/products/

Ngo, V. N., Young, R. M., Schmitz, R., Jhavar, S., Xiao, W., Lim, K.-H., Kohlhammer, H., Xu, W., Yang, Y., Zhao, H., Shaffer, A. L., Romesser, P., Wright, G., Powell, J., Rosenwald, A., Muller-Hermelink, H. K., Ott, G., Gascoyne, R. D., Connors, J. M., Rimsza, L. M., Campo, E., Jaffe, E. S., Delabie, J., Smeland, E. B., Fisher, R. I., Braziel, R. M., Tubbs, R. R., Cook, J. R., Weisenburger, D. D., Chan, W. C., & Staudt, L. M. (2011). Oncogenically active myd88 mutations in human lymphoma. *Nature*, *470*, 115–119. PMID: 21179087. doi:10.1038/nature09671

Nimma, S., Ve, T., Williams, S. J., & Kobe, B. (2017). Towards the structure of the TIR-domain signalosome. *Current Opinion in Structural Biology*, *43*, 122–130. PMID: 28092811. doi:10.1016/j.sbi.2016.12.014

O'Neill, L. A. J., & Bowie, A. G. (2007). The family of five: TIR-domain-containing adaptors in Toll-like receptor signalling. *Nature Reviews Immunology*, *7*(5), 353–364. PMID: 17457343. doi:10.1038/nri2079

Oda, S.-i., Franklin, E., & Khan, A. R. (2011). Poxvirus A46 protein binds to TIR domain-containing Mal/TIRAP via an α-helical sub-domain. *Molecular Immunology*, *48*(15-16), 2144–2150. PMID: 21831443. doi:10.1016/j.molimm.2011.07.014

Ohnishi, H., Tochio, H., Kato, Z., Orii, K. E., Li, A., Kimura, T., Hiroaki, H., Kondo, N., & Shirakawa, M. (2009). Structural basis for the multiple interactions of the MyD88 TIR domain in TLR4 signaling. *Proceedings of the Na-*

tional Academy of Sciences, *106*(25), 10260–10265. PMID: 19506249. doi:10.1073/pnas.0812956106

Pace, C. N., & Scholtz, J. M. (1998). A Helix Propensity Scale Based on Experimental Studies of Peptides and Proteins. *Biophysical Journal*, *75*(1), 422–427. PMID: 9649402. doi:10.1016/s0006-3495(98)77529-0

Pandey, S., Kawai, T., & Akira, S. (2014). Microbial sensing by toll-like receptors and intracellular nucleic acid sensors. *Cold Spring Harbor perspectives in biology*, *7*, a016246. PMID: 25301932. doi:10.1101/cshperspect.a016246

Picard, C., von Bernuth, H., Ghandil, P., Chrabieh, M., Levy, O., Arkwright, P. D., McDonald, D., Geha, R. S., Takada, H., Krause, J. C., Creech, C. B., Ku, C.-L., Ehl, S., Maródi, L., Al-Muhsen, S., Al-Hajjar, S., Al-Ghonaium, A., Day-Good, N. K., Holland, S. M., Gallin, J. I., Chapel, H., Speert, D. P., Rodriguez-Gallego, C., Colino, E., Garty, B.-Z., Roifman, C., Hara, T., Yoshikawa, H., Nonoyama, S., Domachowske, J., Issekutz, A. C., Tang, M., Smart, J., Zitnik, S. E., Hoarau, C., Kumararatne, D. S., Thrasher, A. J., Davies, E. G., Bethune, C., Sirvent, N., de Ricaud, D., Camcioglu, Y., Vasconcelos, J., Guedes, M., Vitor, A. B., Rodrigo, C., Almazán, F., Méndez, M., Aróstegui, J. I., Alsina, L., Fortuny, C., Reichenbach, J., Verbsky, J. W., Bossuyt, X., Doffinger, R., Abel, L., Puel, A., & Casanova, J.-L. (2010). Clinical features and outcome of patients with irak-4 and myd88 deficiency. *Medicine*, *89*, 403–425. PMID: 21057262. doi:10.1097/MD.0b013e3181fd8ec3

Promega. (2010). *Wizard® Plus SV Minipreps DNA Purification System*. Version 12/10. Retrieved from https://www.promega.com/protocols/

Pütz, M. M., Midgley, C. M., Law, M., & Smith, G. L. (2006). Quantification of antibody responses against multiple antigens of the two infectious forms of vaccinia virus provides a benchmark for smallpox vaccination. *Nature Medicine*, *12*(11), 1310–1315. PMID: 17086190. doi:10.1038/nm1457

PyMOL. (2020). The PyMOL Molecular Graphics System, Schrödinger, LLC. (Version 2.4.1).

Roberts, K. L., & Smith, G. L. (2008). Vaccinia virus morphogenesis and dissemination. *Trends in Microbiology*, *16*(10), 472–479. PMID: 18789694. doi:10.1016/j.tim.2008.07.009

Saitoh, S.-i., Akashi, S., Yamada, T., Tanimura, N., Matsumoto, F., Fukase, K., Kusumoto, S., Kosugi, A., & Miyake, K. (2004). Ligand-dependent toll-like receptor 4 (TLR4)-oligomerization is directly linked with TLR4-signaling. *Journal of Endotoxin Research*, *10*(4), 257–260. PMID: 15373971. doi:10.1179/096805104225005904

Schmidt, F. I., Bleck, C. K. E., Helenius, A., & Mercer, J. (2011). Vaccinia extracellular virions enter cells by macropinocytosis and acid-activated membrane rupture. *The EMBO journal*, *30*, 3647–3661. doi:10.1038/emboj.2011.245

Schmidt, F. I., Bleck, C. K. E., & Mercer, J. (2012). Poxvirus host cell entry. *Current Opinion in Virology*, *2*(1), 20–27. PMID: 22440962. doi:10.1016/j.coviro.2011.11.007

Schmidt, F. I., Bleck, C. K. E., Reh, L., Novy, K., Wollscheid, B., Helenius, A., Stahlberg, H., & Mercer, J. (2013). Vaccinia Virus Entry Is Followed by Core Activation and Proteasome-Mediated Release of the Immunomodulatory Effector VH1 from Lateral Bodies. *Cell Reports*, *4*(3), 464–476. PMID: 23891003. doi:10.1016/j.celrep.2013.06.028

Schneider, C. A., Rasband, W. S., & Eliceiri, K. W. (2012). NIH image to ImageJ: 25 years of image analysis. *Nature Methods*, *9*(7), 671–675. PMID: 22930834. doi:10.1038/nmeth.2089

Sinz, A. (2018). Cross-linking/mass spectrometry for studying protein structures and protein-protein interactions: Where are we now and where should we go from here? *Angewandte Chemie International Edition*, *57*(22), 6390–6396. PMID: 29334167. doi:10.1002/anie.201709559

Smith, G. L., Benfield, C. T. O., de Motes, C. M., Mazzon, M., Ember, S. W. J., Ferguson, B. J., & Sumner, R. P. (2013). Vaccinia virus immune evasion: Mechanisms, virulence and immunogenicity. *Journal of General Virology*, *94*(Pt_11), 2367–2392. PMID: 23999164. doi:10.1099/vir.0.055921-0

Smith, G. L., & Law, M. (2004). The exit of vaccinia virus from infected cells. *Virus Research*, *106*(2), 189–197. PMID: 15567497. doi:10.1016/j.virusres.2004.08.015

Smith, G. L., & McFadden, G. (2002). Smallpox: Anything to declare? *Nature Reviews Immunology*, *2*(7), 521–527. PMID: 12094226. doi:10.1038/nri845

Smith, G. L., Vanderplasschen, A., & Law, M. (2002). The formation and function of extracellular enveloped vaccinia virus. *Journal of General Virology*, *83*(12), 2915–2931. PMID: 12466468. doi:10.1099/0022-1317-83-12-2915

Stack, J., & Bowie, A. G. (2012). Poxviral Protein A46 Antagonizes Toll-like Receptor 4 Signaling by Targeting BB Loop Motifs in Toll-IL-1 Receptor Adaptor Proteins to Disrupt Receptor:Adaptor Interactions. *Journal of Biological Chemistry*, *287*(27), 22672–22682. PMID: 22593572. doi:10.1074/jbc.m112.349225

Stack, J., Haga, I. R., Schröder, M., Bartlett, N. W., Maloney, G., Reading, P. C., Fitzgerald, K. A., Smith, G. L., & Bowie, A. G. (2005). Vaccinia virus protein A46R targets multiple Toll-like–interleukin-1 receptor adaptors and contributes to virulence. *The Journal of Experimental Medicine*, *201*(6), 1007–1018. PMID: 15767367. doi:10.1084/jem.20041442

Stern-Ginossar, N., Thompson, S. R., Mathews, M. B., & Mohr, I. (2019). Translational Control in Virus-Infected Cells. *Cold Spring Harbor perspectives in biology*, *11*. PMID: 29891561. doi:10.1101/cshperspect.a033001

Swiss Institute of Bioinformatics. (2019). ExPASy: ProtParam. Retrieved January 28, 2019, from https://web.expasy.org/protparam/

Swiss Institute of Bioinformatics. (2020). ExPASy: ViralZone. Retrieved January 24, 2020, from https://viralzone.expasy.org/4399

The UniProt Consortium. (2019). UniProt: A worldwide hub of protein knowledge. *Nucleic Acids Research*, *47*, D506–D515. PMID: 30395287. doi:10.1093/nar/gky1049

Thermo Fisher Scientific Inc. (2017). *Instructions: EDC*. Version Rev A.0. MAN0017125. Retrieved from https://www.thermofisher.com

Thermo Fisher Scientific Inc. (2018a). *Instructions: DSS and BS^3 Crosslinkers*. Version Rev B.0. MAN0011309. Retrieved from https://www.thermofisher.com

Thermo Fisher Scientific Inc. (2018b). *Instructions: NHS and Sulfo-NHS*. Version Rev B.0. MAN0011240. Retrieved from https://www.thermofisher.com

Treon, S. P., Xu, L., Yang, G., Zhou, Y., Liu, X., Cao, Y., Sheehy, P., Manning, R. J., Patterson, C. J., Tripsas, C., Arcaini, L., Pinkus, G. S., Rodig, S. J., Sohani, A. R., Harris, N. L., Laramie, J. M., Skifter, D. A., Lincoln, S. E., & Hunter, Z. R. (2012). Myd88 l265p somatic mutation in waldenström's macroglobulinemia. *The New England journal of medicine*, *367*, 826–833. PMID: 22931316. doi:10.1056/NEJMoa1200710

Vajjhala, P. R., Ve, T., Bentham, A., Stacey, K. J., & Kobe, B. (2017). The molecular mechanisms of signaling by cooperative assembly formation in innate immunity pathways. *Molecular Immunology*, *86*, 23–37. PMID: 28249680. doi:10.1016/j.molimm.2017.02.012

Ve, T., Gay, N. J., Mansell, A., Kobe, B., & Kellie, S. (2012). Adaptors in toll-like receptor signaling and their potential as therapeutic targets. *Current Drug Targets*, *13*(11), 1360–1374. PMID: 22664090. doi:10.2174/138945012803530260

Ve, T., Vajjhala, P. R., Hedger, A., Croll, T., DiMaio, F., Horsefield, S., Yu, X., Lavrencic, P., Hassan, Z., Morgan, G. P., Mansell, A., Mobli, M., O'Carroll, A., Chauvin, B., Gambin, Y., Sierecki, E., Landsberg, M. J., Stacey, K. J., Egelman, E. H., & Kobe, B. (2017). Structural basis of TIR-domain-assembly formation in MAL- and MyD88-dependent TLR4 signaling. *Nature Structural & Molecular Biology*, *24*(9), 743–751. PMID: 28759049. doi:10.1038/nsmb.3444

Ve, T., Williams, S. J., & Kobe, B. (2015). Structure and function of Toll/interleukin-1 receptor/resistance protein (TIR) domains. *Apoptosis*, *20*(2), 250–261. PMID: 25451009. doi:10.1007/s10495-014-1064-2

Volz, A., & Sutter, G. (2017). Modified Vaccinia Virus Ankara. In *Advances in Virus Research* (pp. 187–243). PMID: 28057259. doi:10.1016/bs.aivir.2016.07.001

Vyncke, L., Bovijn, C., Pauwels, E., Van Acker, T., Ruyssinck, E., Burg, E., Tavernier, J., & Peelman, F. (2016). Reconstructing the TIR Side of the Myddosome: a Paradigm for TIR-TIR Interactions. *Structure*, *24*(3), 437–447. PMID: 26876098. doi:10.1016/j.str.2015.12.018

Wingfield, P. T. (2017). N-Terminal Methionine Processing. *Current Protocols in Protein Science*, *88*(1). PMID: 28369664. doi:10.1002/cpps.29

World Health Organization. (2016). Smallpox vaccines. Retrieved January 19, 2020, from https://www.who.int/csr/disease/smallpox/vaccines/en/

Xie, L., Liu, C., Wang, L., Gunawardena, H. P., Yu, Y., Du, R., Taxman, D. J., Dai, P., Yan, Z., Yu, J., Holly, S. P., Parise, L. V., Wan, Y. Y., Ting, J. P., & Chen, X. (2013). Protein Phosphatase 2A Catalytic Subunit α Plays a MyD88-Dependent, Central Role in the Gene-Specific Regulation of Endotoxin Tolerance. *Cell Reports*, *3*(3), 678–688. doi:10.1016/j.celrep.2013.01.029

7 Abbreviations

Amp	ampicillin
AP-1	activator protein-1
ATP	adenosine triphosphate
BCAP	B-cell adaptor for phosphoinositide 3-kinase
BME	β-mercaptoethanol
BS	binding site
BS^3	bis(sulfosuccinimidyl) suberate
cAMP	cyclic adenosine monophosphate
CD	circular dichroism
COVID-19	coronavirus disease 2019
CREB	cAMP response element-binding protein
CSK	tyrosine-protein kinase, also known as C-terminal Src kinase
CTD	C-terminal domain
CTFR	C-terminal flexible region
DD	death domain
DNA	deoxyribonucleic acid
ds	double-stranded
DTT	dithiothreitol
E.R.	endoplasmic reticulum
EDC	1-ethyl-3-(3-dimethylaminopropyl)carbodiimide hydrochloride
EFC	entry fusion complex
EM	electron microscopy
ETF	early transcription factor
EV	enveloped virion
FDR	false discovery rate
FPLC	fast protein liquid chromatography/chromatogram
GAG	glycosaminoglycan
HEPES	4-(2-hydroxyethyl)-1-piperazineethanesulfonic acid
HIV	human immunodeficiency virus

IκBα	NFκB inhibitor α
IFN	interferon
IKK	IκB kinase
IPTG	isopropyl-β-D-thiogalactopyranosid
IRAK	Interleukin-1 receptor-associated kinase
IRF	interferon regulatory factor
IV	immature virion
JAK	Janus kinase
Kan	kanamycin
kb	kilo bases
KLD	kinase, ligase, *Dpn*I enzyme mix
LB	Luria Bertani broth
LPS	lipopolysaccharide
MAL	MyD88-adaptor like, also known as TIRAP
MAPK	mitogen-activated protein kinase
MBP	maltose binding protein
MD2	myeloid differentiation factor 2
MES	2-(N-morpholino)ethanesulfonic acid
MS	mass spectrometry
MV	mature virion
MVA	modified vaccinia Ankara
MyD88	myeloid differentiation primary response protein 88
NEMO	NFκB essential modulator, also called the subunit γ of IKK
NFκB	nuclear factor κB
Ni-NTA	nickel-charged nitrilotriacetic acid agarose beads
NMR	nuclear magnetic resonance spectroscopy
NTD	N-terminal domain
PAMP	pathogen-associated molecular pattern
PCR	polymerase chain reaction
PDB	Protein Data Bank
PI3K	Phosphoinositide 3-kinase
Poc	Pococurante
PRR	pattern recognition receptor
PSM	peptide spectrum match
PTA	sodium phosphotungstate, pH=7.0 with KOH
PTM	post-translational modification
RNA	ribonucleic acid

SARM1	sterile α- and armidillo-motifs-containing protein 1
SARS-CoV-2	severe acute respiratory syndrome coronavirus 2
SCAF	signaling by co-operative assembly formation
SCIMP	SLP adapter and CSK-interacting membrane protein
SDS	sodium-dodecylsulfate
SDS-PAGE	sodium-dodecylsulfate polyacrylamide gel electrophorese
SEC	size-exclusion chromatography/chromatogram
SH2	Src Homology 2
SLP	SH2-domain-containing leukocyte protein
ss	single-stranded
STAT	signal transducer and activator of transcription
sulfo-NHS	N-hydroxysulfosuccinimide
TAB	TAK1 binding protein
TAK1	TGF-β-activated kinase 1
TANK	TRAF family member-associated NFκB activator
TBK1	TANK-binding kinase 1, also known as serine/threonine-protein kinase
TEV	tobacco etch virus protease
TGF	transforming growth factor
TIR	Toll/Interleukin-1 receptor
TLR	Toll-like receptor
TRAF	tumor necrosis factor receptor-associated factor
TRAM	TRIF-related adaptor molecule, also known as TICAM-2
TRIF	TIR-domain-containing adaptor protein inducing IFNβ, also known as TICAM-1
Tris	tris(hydroxymethyl)-aminomethan
VACV	vaccinia virus
VARV	variola virus
VGF	vaccinia growth factor
VIPER	viral inhibitory peptide of TLR4
WHO	World Health Organization
XL	cross-linker or cross-linking
XL-MS	protein cross-linking coupled with mass spectrometry